

UC San Diego

UC San Diego Electronic Theses and Dissertations

Title

Dynamic Modeling of Earthquake Sources on Rough Faults

Permalink

<https://escholarship.org/uc/item/3h37c2x5>

Author

Yao, Qian

Publication Date

2017

Peer reviewed|Thesis/dissertation

UNIVERSITY OF CALIFORNIA, SAN DIEGO

SAN DIEGO STATE UNIVERSITY

Dynamic Modeling of Earthquake Sources on Rough Faults

A dissertation submitted in partial satisfaction of the
requirements for the degree
Doctor of Philosophy

in

Geophysics

by

Qian Yao

Committee in charge:

University of California, San Diego

Professor Joel Conte
Professor Yuri Fialko

San Diego State University

Professor Steven Day, Chair
Professor Shuo Ma
Professor Samuel Shen

2017

Copyright
Qian Yao, 2017
All rights reserved.

The dissertation of Qian Yao is approved, and it is acceptable in quality and form for publication on microfilm and electronically:

Chair

University of California, San Diego
San Diego State University

2017

DEDICATION

To my family

EPIGRAPH

*Long as the way is
I will keep on searching above and below*
—Qu Yuan

TABLE OF CONTENTS

Signature Page		iii
Dedication		iv
Epigraph		v
Table of Contents		vi
List of Figures		viii
List of Tables		xiii
Acknowledgements		xiv
Vita		xvii
Abstract of the Dissertation		xviii
Chapter 1	Introduction	1
	1.1 Motivation to Study Rough Fault	1
	1.2 Statistics of Kinematic Earthquake Source Parameters	2
	1.3 Supershear Earthquake	3
	1.4 Earthquake Field Observations	4
	1.5 Thesis Overview	5
	References	5
Chapter 2	Earthquake Source Parameter Relationships from 3D Rough Fault Simulations	16
	2.1 Introduction	17
	2.2 Dynamic Rupture Models	21
	2.3 Methods of Analysis	23
	2.4 Result	27
	2.5 Discussion	33
	2.6 Conclusion	34
	2.7 Acknowledgements	35
	References	36
Chapter 3	Supershear Transition Analysis in 3D Rough Fault Dynamic Simulations	52
	3.1 Introduction	53
	3.2 Dynamic Rupture Models	56

	3.3	Supershear Rupture Styles	59
	3.4	Analysis of Supershear Rupture	62
	3.5	Discussion	68
	3.6	Conclusions	71
	3.7	Acknowledgements	72
		References	72
Chapter 4		Surface Lateral Slip and Shallow Slip Deficit from 3D Rough Fault Simulations	93
	4.1	Introduction	94
	4.2	Model Setup	96
	4.3	Result	98
		4.3.1 Surface Lateral Slip	98
		4.3.2 Shallow Slip Deficit	99
		4.3.3 Off-Fault Displacement and Plastic Strain	101
	4.4	Discussion	102
	4.5	Conclusion	104
	4.6	Acknowledgements	106
		References	106

LIST OF FIGURES

Figure 1.1:	Figure 9 from <i>Candela et al. (2009)</i> . 3-D scanner data of the Magnola fault slip surface at different scales.	12
Figure 1.2:	Illustration of Linear slip-weakening friction law, modified from <i>Andrews (1976)</i> , τ_p , yield stress; τ_0 , initial stress, τ_0 , residual frictional stress, d_c , critical slip-weakening distance	13
Figure 1.3:	Supershear happens in Mode II rupture. Figure is from https://pangea.stanford.edu/edunham/research/supershear.html . . .	14
Figure 1.4:	The accumulated slip in the damage zone in the 1992 Landers Earthquake. Figure 3 from <i>Milliner et al. (2015)</i>	15
Figure 2.1:	Model geometry and dimensions for 3D earthquake dynamic rupture. Ruptures are nucleated at 4 possible nucleation centers on the fault plane. (right) Examples of 20 random rough fault surfaces. We apply different amplitude to the surface elevation to adjust for the fault roughness level.	43
Figure 2.2:	Example of 1d fault profiles selected from surface in (right) with α equals 0.001, 0.005 and 0.01 and their power spectral densities. (right) One 2D rough fault surface with minimum wavelength 200m.	44
Figure 2.3:	Illustration that shows how to fit the slip rate function. (left) top shows the fault plane with the red circle as hypocenter. (left) bottom, (right) top and (right) bottom show computer slip rate (black) and fitted slip rate (red) from three selected points on the fault plane (three blue points in (left) top). The slip rate function fit procedure is similar to <i>Schemedes et al. 2010</i>	45
Figure 2.4:	Probability density function for various source parameters computed on points for each dynamic rupture simulation, which is dependent on fault roughness amplitude. We only consider points on the fault plane that have slipped and with sub-shear rupture velocity. (left) Top shows total slip, and bottom shows peak slip rate. (right) shows normalized rupture velocity, V_R is Rayleigh wave velocity. Bottom shows rise time.	46
Figure 2.5:	Probability density function for various source parameters with different fault roughness levels computed on points. The probability density function is dependent on the distance to the nucleation center. We only consider sub-shear and slipped regions in each simulation. (left column) shows peak slip rate, (middle column) shows normalized rupture, and (right column) shows rise time.	47

Figure 2.6:	(left) Example of 1D sin kink, the initial homogeneous background normal and shear stress are applied in the right lateral direction. Normal tractions increase at releasing bends and reduce at restraining bends. (right) Probability density function of ratio of initial shear traction to initial normal traction at different fault roughness levels. Green dashed line is the ratio of initial background shear stress to initial background normal stress.	48
Figure 2.7:	Variation of correlation-coefficient distribution of source parameter and initial traction ratio at different fault roughness levels. Total slip, rupture velocity and peak slip rate show positive correlation with initial traction ratio at all levels of rough faults. Rise time shows no correlation with initial traction ratio. . .	48
Figure 2.8:	Variation of correlation-coefficient distribution of source parameter pairs with different fault roughness level. The main parameters are total slip, peak slip rate, rupture velocity and rise time. Total slip shows positive correlation with peak slip rate, rupture velocity when α is non-zero. The correlation of rise time and total slip is negative when α is small, and become positive when α is large. Peak slip rate shows high correlation with rupture velocity, and rise time is negatively correlated with rupture velocity and peak slip rate at all fault roughness level.	49
Figure 2.9:	Example of slip, normalized rupture velocity, initial traction ratio and peak slip rate distributions on fault plane in one realization. From top to bottom, the fault roughness level changes from 0.001, 0.003, 0.005, 0.007 to 0.009.	50
Figure 2.10:	Spatial coherence of different source parameters. (a), (b) and (c) are correlogram distributions of rupture velocity, total slip and peak slip rate with initial traction ratio. (d) shows correlogram distributions of rupture velocity with peak slip rate. From top to bottom, the fault roughness level changes from 0.001, 0.003, 0.005, 0.007 to 0.009.	51
Figure 3.1:	Snapshots of slip pulse evolution on rough fault with presence of favorable geometry, generating daughter crack like supershear. The yellow dot at (10km, 10km) at each figure is the hypocenter. (Left) Slip rate distribution superimposed on rupture velocity distribution. All red parts are supershear areas. The blue pulses are slip rate pulses. (Right) Slip rate distribution superimposed on fault geometry.	82
Figure 3.2:	Snapshots of slip pulse evolution on rough fault with pulse-focusing effect like supershear. The yellow dot at (10km, 10km) at each figure is the hypocenter. Same as above.	83

Figure 3.3:	Snapshots of slip pulse evolution on rough fault with free surface triggered supershear. The yellow dot at (30km, 15km) at each figure is the hypocenter. Same as above.	84
Figure 3.4:	Fault roughness reduces supershear at the free surface in SET2. (Left) Comparison of rupture velocity distribution on the fault at different levels of fault roughness in one realization. From top to bottom, α is from 0.001 to 0.009. (Right) Bottom is probability density of rupture velocity at all points free surface to 2km depth at different levels of fault roughness. Top is the zoom in session of bottom at supershear regions	85
Figure 3.5:	(Left) Rupture velocity distribution on the fault at all levels of fault roughness level in one realization in SET3, and α is from 0.001 to 0.009. The friction coefficients near free surface are tapering. (Right) Probability densities of rupture velocity in all simulations in SET3.	86
Figure 3.6:	Fault roughness enhances supershear on the fault plane in SET1. (Left) Comparison of rupture velocity distribution on the fault on different levels of fault roughness in one realization. From top to bottom, α is from 0.001 to 0.009. (Right) Bottom is probability density of rupture velocity at all points on fault plane at different levels of fault roughness. Top is the zoomed out session of bottom at supershear regions.	87
Figure 3.7:	Probability density of local traction ratio for supershear points vs. subshear points for α from 0.001 to 0.009. The solid lines are for points in sub-shear regions, and the dashed lines are for points in supershear regions. R is the background stress ratio which is the ratio of background shear stress and background normal stress, which is 0.5833.	88
Figure 3.8:	Pseudo-stress Model. (Top) left shows the fault geometry in one simulation in SET1. Right is distribution of normal traction projected on the fault plane from background stress. (Bottom) left is distribution of shear traction along dip direction as before, right is the distribution of shear traction along strike direction as before.	89
Figure 3.9:	Comparison between the same case in pseudo-stress model and rough model at all level of fault roughness. (Left) Distribution of rupture velocity at each simulation in rough model in SET1, and α is increasing from top to bottom. (Middle) same as before in pseudo-stress model in SET5. (Right) Probability densities of rupture velocity in all simulation in SET1 and SET5.	90

Figure 3.10: (Left) Rupture velocity distribution on the fault at different levels of fault roughness in one realization when background shear stress is 70MPa. From top to bottom, α is increasing from 0.001 to 0.009. (Middle) Rupture velocity distribution on the fault at different levels of fault roughness in one realization when background shear stress is 71MPa. From top to bottom, α is increasing from 0.001 to 0.009. (Right) Middle figure is probability densities of rupture velocity in all simulation in SET1 and SET4. The solid lines are for probability densities in SET1, and dashed lines are for probability densities in SET4. Increasing background shear stress increases supershear phenomena. Top figure is the zoomed out of supershear region in the middle figure.	91
Figure 3.11: Connecting supershear patches depend on the distance to the nucleation center, nucleation strategy, fault length and fault width. (left) shows comparisons of all connecting supershear patches areas whose area are no smaller than $0.5km^2$ vs distance to nucleation center in SET7, SET1 $\alpha = 0.005$ and SET6 in the nucleation regions. (middle) shows the same as before, except outside of the nucleation regions. (right) shows comparisons of ratio of all connecting supershear patches areas and ruptured areas vs distance to nucleation center in SET7, SET1 $\alpha = 0.005$ and SET6. The circle size for each point is proportional to the ruptured area in that simulation event.	92
Figure 4.1: Model Geometry and dimensions for 3D earthquake dynamic rupture. (Top) Example of rough fault surface. The color scale denotes deviation of the rough-fault surface. For better view, the fault deviation has been greatly exaggerated in the 3D plot.	114
Figure 4.2: Initial normal and shear stresses resolved onto the mean fault plane, RSD friction parameters (b and v_w).	115
Figure 4.3: Final slip distribution on fault plane from dynamic rupture at 5 different α level (increasing from top to bottom) in plastic cases. Black lines are contours of rupture fronts at 1s intervals mapped onto the mean fault plane.	116
Figure 4.4: (a) Surface lateral slip distributions and power spectral density of surface lateral slip in (a) elastic cases and (b) plastic cases at 5 different fault roughness levels. Solid lines are calculated psd, and dashed lines are fitted psd. (d) Hurst exponents of surface lateral slip distributions.	117

Figure 4.5:	(left) shows mean surface slips (averaged along strike) obtained at 5 fault roughness levels. (right) shows the ratio of slip near Earth surface and at depth, are dependent on the fault roughness level.	118
Figure 4.6:	(left) Mean fault parallel displacement (averaged along strike) obtained for both elastic and plastic cases at 5 fault roughness levels. (right) Ratio of fault parallel displacement to on fault displacement for both elastic and plastic cases at 5 fault roughness levels.	119
Figure 4.7:	Power spectral density of surface lateral slips on-fault and on-plus off-fault within different damage zone $-0.25\text{km}\sim 0.25\text{km}$, $-0.5\text{km}\sim 0.5\text{km}$, $-0.75\text{km}\sim 0.75\text{km}$ at 5 different fault roughness levels in plastic cases. Solid lines are calculated psd, and dashed lines are fitted psd. (right) Hurst exponent of different surface lateral slips.	120
Figure 4.8:	Distributions of accumulated plastic strain along cross-sections perpendicular to fault at $x = 10\text{km}$ for plastic cases.	121
Figure 4.9:	Distributions of accumulated plastic strain at 25m for plastic cases for different fault roughness levels. α ranges from 0.001 to 0.009 from top to bottom.	122

LIST OF TABLES

Table 2.1: Model Parameters	42
Table 3.1: Model Parameters	80
Table 3.2: Different Sets of Simulation Ensembles	81
Table 4.1: Model Parameters	113

ACKNOWLEDGEMENTS

First and foremost, I would like to thank my advisor, Professor Steven Day. With his outstanding guidance, suggestion, and encouragement, I have had great opportunities to explore geophysics and earthquake dynamic rupture on rough fault. Steve was the chair when I first joined the doctorate program at 2011. He taught us classes about rupture dynamics from 2012 to 2013. When we had any question in his classes, he was always quick to give us detailed and clear explanations. I was very impressed with his depth and breath of knowledge and professionalism. I transferred to Steve's group at the beginning of 2014 fall semester. He introduced me to the world of numerical simulations of earthquake dynamics and provide me the rupture dynamic code, and I started to study source-parameter correlations in 3D strike slip rough fault dynamic simulations. Later, we observed very interesting supershear phenomena in our rough fault simulations. Then we found that lots of geological observations like, not limited to, fractal surface slip can be potentially explained by rough fault simulations. Besides earthquake dynamics, I learned how to prepare presentations and write technical papers from Steve. He is very patient when helping me modify presentation poster and slides, and edit papers. I can clearly feel my improvement on these two areas during the past three years. What I learn from him is not only how to become an independent researcher, but also how to become a better person. He is a very extraordinary advisor, who gives me lots of inspiration about my research and strong support, both emotional and financial during my hard time in my graduate life, making my completion of degree possible. It is my honor to work with him for the last three years.

I would like to thanks my dissertation committee members, Dr. Yuri Fialko, Dr. Samuel Shen, Dr. Shuo Ma, and Dr. Joel Conte for their support and help on my PhD research. The committees feedback and comments were very helpful in improving this dissertation.

I also thank Dr. Zheqiang Shi for his guidance, support and friendship. He provided me SORD code and gave me lots of technical support to use the code. Several of the ideas in this work were sparked by our discussions during weekly

meeting and daily talk. He gave me lots of help and encouragement during my transition time to current group.

I also thanks Dr. Shuo Ma for guidance and support during the early part of my PhD studies and for inspiring my interests in GPS inversion and tsunami wave propagation, especially subduction zone earthquake. When I applied for the doctorate program, Dr. Ma is very nice to help me pay the application fee in time, and conducted interview on me who makes my life in San Diego in the past six years possible. He is a good advisor who cares the career growth of his students, and gives a good example of a young scientist.

During my graduate studies, I took many useful classes from excellent teachers. I want to express my deep appreciation to them: Dr. Duncan Agnew, Dr. Peter Shearer, Dr. Guy Masters, Dr. Catherine Constable, Dr. David Sandwell, Dr. Hubert Staudigel, Dr. Kevin Brown, Dr. John Orcutt, Dr. Dave Stegman and Dr. Dan Rudnick in Scripps Institution of Oceanography at UCSD, Dr. Steve Day, Dr. Shuo Ma, Dr. Kim Olsen in Department of geological sciences at SDSU. I would like to thank former administrative support Sem Tran, Tony Carrasco and current administrative support Irene Occhiello, Heather Webb and Pia Parrish in Department of geological sciences at SDSU, Gilbert at UCSD to help me a lot on various forms, class registration, financial support, IT support and graduation procedures. I also would to thank the IGPP computing and networking helpdesk at UCSD to take care of my computer issues.

I owe a great debt of gratitude to many people when I was studying in our joint doctorate program. I am grateful to have friends in talented geophysics cohort of which I was part of: Wenyuan, Kang, Kyle, Shi, Maggie, Peter, Nick, Lauren. I appreciate the support and friendship from fellow people in SDSU-UCSD joint doctorate program: Evan, Kyle, Bill, Yuval, Yongfei, Nan and Zhifeng. They provided me with countless discussions about science and life which makes my daily life more enjoyable. I'd like to acknowledge my other geophysicist friends: Xiaowei, who helped me settle down when I first arrived San Diego, like a big sister, Wei, Zhitu, Huajian, Lijun, Xiaopeng, Linghan, Xiaohua, Yuxiang, Zhao and Shiyong (big chinese community here). Diego and Brendon who are very nice

to give me tutorial about GPS inversion, Erica who provides lots of rides for me, including first SCEC and GP field trips, and lots of students who organize field trips and camping for GP students.

I am also grateful for the friendship outside of my academic circle, particularly friends from my undergraduate university USTC, make my life in San Diego more pleasant and fulfilling. Houdong and Duo provided me countless help during my graduate study. Xiaoshan, who is one of the best friends in San Diego, shared lots of happiness with me, taught me lots of soft skills. Hua and Sharon, both of them are very good friends, always showed positive attitude to life, and encourage me when I am miserable.

Finally, my endless love goes to my family. To my parents, you give me good care, education, endless love and guidance to science. You are very supportive about every decision I made. To my husband, Ning, thank you for your support, encouragement, confidence and love you have in me, making my life much happier and easier. You always push me to make the right decision to my career and life. I can not imagine how my life will be without you. To my son, Mason, you are always the source of my happiness, and thank you for letting me experience the joy and bitterness being a new mom.

Chapter 2, in full, is a reformatted version of a paper currently being prepared for submission for publication to Journal of Geophysical Research: Yao, Q. and S. M. Day, Earthquake Source Parameter Relationships from 3D Rough Fault Simulations. (2017). I was the primary investigator and author of this paper.

Chapter 3, in full, is a reformatted version of a paper currently being prepared for submission for publication to Journal of Geophysical Research: Yao, Q. and S. M. Day, Supershear Transition Analysis in 3D Rough Fault Dynamic Simulations. (2017). I was the primary investigator and author of this paper.

Chapter 4, in full, is a reformatted version of a paper currently being prepared for submission for publication to Geophysical Research Letters: Yao, Q. and S. M. Day, Free Surface Lateral Slip and Shallow Slip Deficit from 3D Rough Fault Simulations. (2017). I was the primary investigator and author of this paper.

VITA

- 2011 B. S. in Geophysics, University of Science and Technology of
China
- 2017 Ph. D. in Geophysics, University of California, San Diego and
San Diego State University

PUBLICATIONS

Yao, Q. and S. M. Day, Earthquake Source Parameter Relationships from 3D Rough Fault Simulations. (2017) (currently being prepared for submission for publication to Journal of Geophysical Research)

Yao, Q. and S. M. Day, Supershear Transition Analysis in 3D Rough Fault Dynamic Simulations. (2017) (currently being prepared for submission for publication to Journal of Geophysical Research)

Yao, Q. and S. M. Day, Surface Lateral Slip and Shallow Slip Deficit from 3D Rough Fault Simulations. (2017) (currently being prepared for submission for publication to Geophysical Research Letter)

ABSTRACT OF THE DISSERTATION

Dynamic Modeling of Earthquake Sources on Rough Faults

by

Qian Yao

Doctor of Philosophy in Geophysics

University of California and San Diego, 2017
San Diego State University, 2017

Professor Steven Day, Chair

Surface roughness is a universal characteristic of natural faults. Roughness can be represented statistically as a random field that is approximately self-similar over many orders of magnitude in scale-length with a ratio of amplitude to length scale that typically falls into the range 10^{-3} to 10^{-2} . Incorporating realistic rough fault surface into 3D numerical simulations of earthquake dynamic rupture provides guidance to build kinematic rupture generator.

We have built a database of more than 1000 simulations of 3D strike slip dynamic rupture for different realizations of rough fault surfaces at different fault roughness levels. We first have explored the role of the fault roughness in influencing the 1-point and 2-point statistics of earthquake source parameters such as rupture velocity, peak slip rate, total slip, and slip rise time. Fault roughness

reduces the amplitudes of rupture velocity, peak slip rate, rise time and total slip.

Then, we have extended our study to assess supershear transition mechanisms that operate in 3D on rough faults and what factors contribute to the frequency of occurrence and spatial extent of supershear rupture episodes. We have reconciled the conflict that the supershear is favored by fault roughness from 2D numerical simulation (Bruhat et al., 2016) and unfavored by fault roughness from field observations (Bouchon et al., 2010) by dividing supershear into two types supershear transitions: free surface supershear transition and buried supershear transition.

Finally, we have investigated how well simulated earthquake behaviors on rough fault relate to direct geological observations, such as free surface lateral slip, plastic strain, and shallow slip deficits. We have found that fault roughness in the form of a power law leads to self-affine surface lateral slip, which is in agreement with recent optical imaging observations in the 1992 Landers earthquake (Milliner et al., 2015). Also fault roughness tends to produce individual events with large shallow slip deficits, which may help explain the suggestion that has been made, based on a small number of earthquakes, that the SSD tends to be larger on immature faults.

Chapter 1

Introduction

1.1 Motivation to Study Rough Fault

Faults are complex structures, consisting of many scales of geometrically complex features and a variety of different forms of heterogeneity. Geometrical complexities are obvious from surface trace mapping. A fault system may include multiple branching, discontinuous strands or secondary faulting (e.g., *Ben-Zion and Sammis, 2003; Bryant et al., 2005; Power and Tullis, 1991; Renard et al., 2006; Sagy et al., 2007; Sage and Brosky, 2009; Candela et al., 2009, 2012; Bistacchi et al., 2011*). Fault surfaces are not geometrically flat. The surface roughness can affect the stresses around the fault, and the dynamic stress perturbations induced during earthquake slip, leading to a significant changes in earthquake nucleation and propagation (e.g., *Chester and Chester, 2000; Campillo et al., 2001; Dieterich and Smith, 2009; Griffith et al., 2010*).

Dynamic rupture modeling has been a fruitful way to investigate the effects of geometrical complexity on rupture propagation. Several studies have already been conducted to numerically simulate dynamic rupture on nonplanar faults (e.g., *Dunham et al., 2011a; Shi and Day, 2013*). The fluctuations of slip rate and rupture velocity induced by fault roughness lead to heterogeneous slip distribution and the excitation of high-frequency accelerations. The latter result is consistent with previous theoretical work predicting strong high-frequency radiation when rupture fronts accelerate or decelerate, as would be expected from interactions with fault

geometrical irregularity (e.g., *Madariaga, 1977; Boore and Joyner, 1978; Kame and Uchida, 2008*).

There are many geophysically interesting, and practically important, topics related to the dynamics of rough faults that can be profitably addressed in numerical simulations, such as dependency of high frequency ground motions on fault roughness, stress drop variations on rough faults, the conditions governing super-shear transitions and other exciting topics. In many cases, the statistical analysis of large ensembles of simulations may be required to meaningfully relate the simulations to geophysical observations. With the advanced computational ability of supercomputers, and evolving analytical methods, researchers can address them one by one in the future.

1.2 Statistics of Kinematic Earthquake Source Parameters

Both kinematic and dynamic simulations have been used to simulate strong ground motions. Kinematic simulations take as their input the slip function, parameterized by source parameters such as slip, slip rate, rupture velocity and rise time. Methodologies for assigning those parameters are sometimes called kinematic rupture generators. At low frequencies, the source parameters may be assigned on the basis of simplified theoretical models or slip inversions of past earthquakes (e.g., *Mai et al., 2010; Roten et al., 2014; Graves and Pitarka, 2010*). Dynamic rupture models provide another approach to simulate strong ground motion. The fault surface geometry, initial stress state, and the frictional parameters are the inputs to dynamic models, generating consistent physics-based rupture kinematics and ground motions (e.g., *Olsen et al., 2009; Shi and Day, 2013; Ma and Andrews, 2010; Roten et al., 2014*). However, the dynamic approach has the disadvantage that is difficult to adjust input parameters (some of which are poorly constrained by direct observations) to fit ground motion records in past earthquakes, and dynamic models also are much more computationally complex. Therefore, a viable approach is to use a combination of kinematic and dynamic approaches in which

ensembles of dynamic simulations are used to estimate the source-parameter statistical distributions for a kinematic formulation. This promising approach to ground motion simulation is called pseudo-dynamic modeling.

On planar faults, several studies have been carried out to contribute to this pseudo-dynamic approach (e.g., *Oglesby and Day, 2002; Guatteri et al., 2003; Ripperger et al., 2007; Song and Somerville, 2010; Schmedes et al., 2010, 2012*). Based on source parameter relationships on planar faults, a kinematic rupture generator has been built for the 1994 Northridge and 1989 Loma Prieta earthquake (*Schmedes et al., 2012*). The study of kinematic source parameters on rough faults can add more realistic features when building a kinematic rupture generator. In particular, the degree to which the various parameters are correlated with each other affects the variance obtained in an ensemble of ground motion simulations, and that variance is of great importance in probabilistic seismic hazard analysis. To describe the source-parameter distributions appropriate to rough-fault kinematics, both 1-point and 2-point statistics are relevant (*Song and Somerville, 2010; Song et al., 2009*). 1-point statistics are used to calculate correlation coefficient of two source parameters, regarded as random fields with zero offset. 2-point statistics are used to calculate the correlation coefficient of two source parameters with non-zero offset.

1.3 Supershear Earthquake

A supershear earthquake is an earthquake in which the rupture propagation along part of the fault surface propagates at speeds in excess of the shear wave velocity. Previous theoretical work has investigated supershear rupture (e.g., *Burridge, 1973; Andrews, 1976; Freund, 1979*). Supershear rupture propagation has been documented from seismic observations (e.g., *Archuleta, 1984; Bouchon et al., 2000, 2001; Dunham et al., 2004; Bouchon and Vallée, 2003; Robinson et al., 2006; Vallée et al., 2008; Yue et al., 2013*) and observed in laboratory experiments (e.g., *Xia et al., 2004*). However, most numerical studies of supershear rupture (e.g., *Andrews, 1976; Day, 1982; Schmedes et al., 2010; Bizzarri and Das, 2012;*

Dunham et al., 2003; Dunham, 2007) are limited to a planar fault surface.

It is important to better understand the supershear transitions on rough faults. Rough fault dynamic simulations in 2D have shown that the supershear transition is very sensitive to the background stress level and local geometry (*Bruhat et al., 2016*). Therefore, we can anticipate that 3D rough-fault dynamic rupture simulations will yield some new insights not available from the 2D simulations.

1.4 Earthquake Field Observations

In addition to the fractal-like fault geometry of faults that is revealed by surface trace mapping, similarly complex fluctuations of fault surface slip in individual earthquakes have also been observed through high resolution imaging (e.g., *Rockwell et al., 2002; Rockwell and Klinger, 2013*). For example, the final slip is self-affine fractal in the 1992 Landers earthquake, showing fluctuations at all observable length scales (*Milliner et al., 2015*). Furthermore, surface deformation is not, in general, fully confined to the fault trace. For example, off-fault deformation has been documented in many strike-slip earthquakes, such as the 1992 M7.3 Landers earthquake (*Milliner et al., 2015*), the 1999 Hector Mine earthquake (*Milliner et al., 2016*), the 1999 M7.5 Izmit earthquake (*Rockwell et al., 2002*) and the 2013 Balochistan earthquake (*Gold et al., 2015*).

Another set of relevant observations come from coseismic slip inversions, which are informed by GPS, inSAR, and seismic data. In large strike slip earthquakes, slip at depth around 4-5km is systematically larger than slip near Earth surface (e.g., *Reilinger et al., 2000; Simons et al., 2002; Fialko, 2004; Fialko et al., 2005; Bilham, 2010*), a phenomenon which is called shallow slip deficit (SSD). Geological observation suggest that structurally mature, large-cumulative-displacement faults are associated with smaller SSD than faults that are structurally immature and small-cumulative-slip (*Dolan and Haravitch, 2014*).

3D dynamic rupture simulations that incorporate rough fault surfaces can contribute to our understanding of the above field observations. Simulations can

help us understand the origin of the self-affine character of surface slip and aid us in quantifying the relationships between fault roughness level and measurable effects such as SSD, off-fault deformation, and along-trace variability of the surface slip.

1.5 Thesis Overview

This primary focus of this work is to characterize the dynamic behavior of rough faults, as revealed by 3D simulations. It is natural that much of that characterization takes the form of statistical distributions obtained from large ensembles of simulations. Because the thesis focuses on 3D effects and large simulations, the efficient use of advanced supercomputers was an essential aspect of the work. This work is organized as follows. Chapter 2 discusses 1-point and 2-point source parameter relationships based on 3D earthquake dynamic ruptures on rough faults. Chapter 3 discusses supershear transition mechanisms on 3D rough faults, and factors that contribute to the frequency of occurrences and rupture extent of supershear. Chapter 4 contains a study that uses 3D numerical simulations to relate fault roughness effects to empirically observed near-fault deformational behaviors of earthquakes, including fractal-like free-surface lateral slip, plastic strain distributions and shallow slip deficits.

References

- Andrews, D. J. (1976), Rupture velocity of plane strain shear cracks, *J. Geophys. Res.*, *81*(32), 5679-5687, doi:10.1029/JB081i032p05679.
- Archuleta, R. J. (1984), A faulting model for the 1979 Imperial Valley earthquake, *J. Geophys. Res.*, *89*(B6), 4559-4585, doi:10.1029/JB089iB06p04559.
- Ben-Zion, Y., and C. G. Sammis (2003), Characterization of fault zones, *Pure Appl. Geophys.*, *160*, 677-715, doi:10.1007/PL00012554.
- Bilham, R. (2010). Lessons from the Haiti earthquake, *Nature*, *463*(7283), 878-879.
- Bistacchi, A., W. A. Griffith, S. A. F. Smith, G. Di Toro, R. Jones, and S. Nielsen

- (2011), Fault roughness at seismogenic depths from LIDAR and photogrammetric analysis, *Pure Appl. Geophys.*, doi:10.1007/s00024-011-0301-7.
- Bizzarri, A., and S. Das (2012), Mechanics of 3-D shear cracks between Rayleigh and shear wave rupture speeds, *Earth Planet. Sci. Lett.*, 357358, 397404, doi:10.1016/j.epsl.2012.09.053.
- Boore, D. M., and W. B. Joyner (1978), The influence of rupture incoherence on seismic directivity, *Bull. Seismol. Soc. Am.*, 68, 283300.
- Bouchon, M., and M. Vallée (2003), Observation of long supershear rupture during the magnitude 8.1 Kunlunshan earthquake, *Science*, 301(5634), 824826, doi:10.1126/science.1086832.
- Bouchon, M., N. Toksz, H. Karabulut, M. P. Bouin, M. Dietrich, M. Aktar, and M. Edie (2000), Seismic imaging of the 1999 Izmit (Turkey) rupture inferred from the near-fault recordings, *Geophys. Res. Lett.*, 27(18), 30133016, doi:10.1029/2000GL011761.
- Bouchon, M., M. P. Bouin, H. Karabulut, M. Nafi Toksz, M. Dietrich, and A. J. Rosakis (2001), How fast is rupture during an earthquake? New insights from the 1999 Turkey earthquakes, *Geophys. Res. Lett.*, 28(14), 27232726, doi:10.1029/2001GL013112.
- Bruhat, L., Z. Fang, and E. M. Dunham(2016), Rupture complexity and the supershear transition on rough faults, *J. Geophys. Res. Solid Earth*, 121, doi:10.1002/2015JB012512.
- Bryant, W. A. (1992), Surface fault rupture along the Johnson Valley, Homestead Valley, and related faults associated with the Ms 7.5 28 June 1992 Landers earthquake, Fault Eval. Rep. FER-234, 21 p., scale 1:24,000, Calif. Dep. of Conserv., Div. of Mines and Geol., Sacramento, Calif.
- Bryant, W. A. (1994), Surface fault rupture along the Homestead Valley, Emerson, and related faults associated with the Mw 7.3 28 June 1992 Landers earthquake, Fault Eval. Rep. FER-239, 18 p., scale 1:24,000, Calif. Dep. of Conserv., Div. of Mines and Geol., Sacramento, Calif.
- Bryant, W. A. (Comp.) (2005), Digital database of Quaternary and younger faults from the fault activity map of California, version 2.0, California Geological Survey.
- Burridge, R. (1973), Admissible speeds for plane-strain self-similar shear cracks with friction but lacking cohesion, *Geophys. J. R. Astron. Soc.*, 35(4), 439455, doi:10.1111/j.1365-246X.1973.tb00608.x.

- Campillo, M., P. Favreau, I. R. Ionescu, and C. Voisin (2001), On the effective friction law of a heterogeneous fault, *J. Geophys. Res.*, *106*(B8), 16,30716,322.
- Candela, T., F. Renard, M. Bouchon, A. Brouste, D. Marsan, J. Schmittbuhl, and C. Voisin (2009), Characterization of fault roughness at various scales: Implications of three-dimensional high resolution topography measurements, *Pure Appl. Geophys.*, *166*(1011), 18171851, doi:10.1007/s00024-009-0521-2.
- Candela, T., F. Renard, Y. Klinger, K. Mair, J. Schmittbuhl, and E. E. Brodsky (2012), Roughness of fault surfaces over nine decades of length scales, *J. Geophys. Res.*, *117*, B08409, doi:10.1029/2011JB009041.
- Chester, F. M., and J. S. Chester (2000), Stress and deformation along wavy frictional faults, *J. Geophys. Res.*, *105*(B10), 23,42123,430, doi:10.1029/2000JB900241.
- Day, S. M. (1982). Three-dimensional simulation of spontaneous rupture: the effect of nonuniform prestress. *Bull. Seismol. Soc. Am.*, *72*, 18811902.
- Dieterich, J. H., and D. E. Smith (2009), Nonplanar faults: Mechanics of slip and off-fault damage, *Pure Appl. Geophys.*, *166*(1011), 17991815, doi:10.1007/s00024-009-0517-y
- Dolan, J. F., and B. D. Haravitch (2014), How well do surface slip measurements track slip at depth in large strike-slip earthquakes? The importance of fault structural maturity in controlling on-fault slip versus off-fault surface deformation, *Earth and Planetary Science Letters*, *388*, 3847.
- Dunham, E. M. and R. J. Archuleta (2004), Near-source ground motion from steady state dynamic rupture pulses, *Geophysical Research Letters*, *32*, L03302, doi:10.1029/2004GL021793.
- Dunham, E. M. (2007), Conditions governing the occurrence of supershear ruptures under slip-weakening friction, *J. Geophys. Res.*, *112*, B07302, doi:10.1029/2006JB004717.
- Dunham, E. M., P. Favreau, and J. M. Carlson (2003), A supershear transition mechanism for cracks, *Science*, *299*(5612), 15571559.
- Dunham, E. M., and R. J. Archuleta (2004), Evidence for a supershear transient during the 2002 Denali fault earthquake, *Bull. Seismol. Soc. Am.*, *94*(6B), S256S268, doi:10.1785/0120040616.
- Dunham, E. M., D. Belanger, L. Cong, and J. E. Kozdon (2011a), Earthquake ruptures with strongly rate-weakening friction and off-fault plasticity, Part 1: Planar faults, *Bull. Seismol. Soc. Am.*, *101*(5), 22962307, doi:10.1785/0120100075.

- Dunham, E. M., D. Belanger, L. Cong, and J. E. Kozdon (2011b), Earthquake ruptures with strongly rate-weakening friction and off-fault plasticity, Part 2: Nonplanar faults, *Bull. Seismol. Soc. Am.*, *101*(5), 23082322, doi:10.1785/0120100076.
- Fialko, Y. (2004), Evidence of fluid-filled upper crust from observations of post-seismic deformation due to the 1992 Mw 7.3 Landers earthquake, *Journal of Geophysical Research: Solid Earth*, *109*(B8).
- Fialko, Y., D. Sandwell, M. Simons, and P. Rosen (2005), Three-dimensional deformation caused by the Bam, Iran, earthquake and the origin of shallow slip deficit, *Nature*, *435*(7040), 295299.
- Freund L. B. (1979). The mechanics of dynamic shear crack propagation, *J. geophys. Res.*, *84*, 21992209.
- Gold, R. D., N. G. Reitman, R. W. Briggs, W. D. Barnhart, G. P. Hayes, and E. Wilson (2015), On- and off-fault deformation associated with the September 2013 Mw7.7 Balochistan earthquake: Implications for geologic slip rate measurements, *Tectonophysics*, *660*,6578.
- Graves, R. W., Pitarka, A. (2010). Broadband ground-motion simulation using a hybrid approach. *Bull. Seismol. Soc. Am.*, *100*(5A), 20952123.
- Griffith, W. A., S. Nielsen, G. Di Toro, and S. A. F. Smith (2010), Rough faults, distributed weakening, and off-fault deformation, *J. Geophys. Res.*, *115*, B08409, doi:10.1029/2009JB006925.
- Guatteri, M., P. M. Mai, G. C. Beroza, and J. Boatwright (2003). Strong ground-motion prediction from stochastic-dynamic source models, *Bull. Seismol. Soc. Am.*, *93*, no. 1, 301313, doi: 10.1785/0120020006.
- Kame, N., and K. Uchida (2008), Seismic radiation from dynamic coalescence, and reconstruction of dynamic source parameters on a planar fault, *Geophys. J. Int.*, *174*(2), 696706, doi:10.1111/j.1365-246X.2009.03849.x.
- Liu, J., K. Sieh, and E. Hauksson (2003), A structural interpretation of the after-shock Cloud of the 1992 M-w 7.3 Landers earthquake, *Bull. Seismol. Soc. Am.*, *93*(3), 13331344, doi:10.1785/0120020060.
- Ma, S., and D. J. Andrews (2010), Inelastic off-fault response and three dimensional dynamics of earthquake rupture on a strike-slip fault, *J. Geophys. Res.*, *115*(B4), 116. doi:10.1029/2009JB006382.
- Madariaga, R. (1977). High-frequency radiation from crack (stress drop) models of earthquake faulting, *Geophys. J. Roy. Astron. Soc.*, *51*, no. 3, 625651, doi: 10.1111/j.1365-246X.1977.tb04211.x.

- Mai, P.M., Imperatori, W., Olsen, K. B. (2010). Hybrid broadband ground-motion simulations: combining long-period deterministic synthetics with high-frequency multiple S-to-S backscattering. *Bull. Seismol. Soc. Am.*, *100*, 21242142. doi:10.1785/0120080194
- Milliner, C., J. Dolan, J. Hollingsworth, S. Leprince, F. Ayoub, and C. Sammis (2015), Quantifying near-field and off-fault deformation patterns of the 1992 Mw 7.3 Landers earthquake, *Geochemistry, Geophysics, Geosystems*, *16*(5), 15771598.
- Milliner, C., J. Dolan, J. Hollingsworth, S. Leprince, and F. Ayoub (2016), Comparison of coseismic near-field and off-fault surface deformation patterns of the 1992 mw 7.3 anders and 1999 mw 7.1 hector mine earthquakes: Implications for controls on the distribution of surface strain, *Geophysical Research Letters*, *43*(19).
- Oglesby, D. D., and S. M. Day (2002). Stochastic fault stress: Implications for fault dynamics and ground motion, *Bull. Seismol. Soc. Am.*, *92*, no. 8, 30063021, doi: 10.1785/0120010249.
- Olsen, K. B., S. M. Day, L. Dalguer, J. Mayhew, Y. Cui, J. Zhu, V.M. Cruz-Atienza, D. Roten, P. Maechling, T.H. Jordan, and A. Chourasia (2009). ShakeOut-D: Ground Motion Estimates Using an Ensemble of Large Earthquakes on the Southern San Andreas Fault With Spontaneous Rupture Propagation, *Geophysical Research Letters* *36*L04303, doi:10.1029/2008GL036832.
- Power, W. L., and T. E. Tullis (1991), Euclidean and fractal models for the description of rock surface roughness, *J. Geophys. Res.*, *96*(B1), 415424, doi:10.1029/90JB02107.
- Reilinger, R., S. Ergintav, R. Brgmann, S. McClusky, O. Lenk, A. Barka, O. Gurkan, L. Hearn, K. Feigl, R. Cakmak, et al. (2000), Coseismic and postseismic fault slip for the 17 August 1999, M= 7.5, Izmit, Turkey earthquake, *Science*, *289*(5484), 15191524.
- Renard, F., C. Voisin, D. Marsan, and J. Schmittbuhl (2006), High resolution 3-D laser scanner measurements of a strike-slip fault quantify its morphological anisotropy at all scales, *Geophys. Res. Lett.*, *33*, L04305, doi:10.1029/2005GL025038.
- Ripperger, J., J. P. Ampuero, P. M. Mai, and D. Giardini (2007). Earthquake source characteristics from dynamic rupture with constrained stochastic fault stress, *J. Geophys. Res.*, *112*, no. B04311, doi: 10.1029/ 2006JB004515.
- Robinson, D. P., C. Brough, and S. Das (2006), The Mw 7.8, 2001 Kunlunshan earthquake: Extreme rupture speed variability and effect of fault geometry, *J. Geophys. Res.*, *111*, B08303, doi:10.1029/2005JB004137.

- Rockwell, T. K., S. Lindvall, T. Dawson, R. Langridge, W. R. Lettis, and Y. Klinger (2002), Lateral offsets on surveyed cultural features resulting from the 1999 Izmit and Duzce Earthquakes, Turkey, *Bull. Seismol. Soc. Am.*, *92*, 7994, doi:10.1785/0120000809.
- Rockwell, T. K., and Y. Klinger (2013), Surface rupture and slip distribution of the 1940 Imperial Valley earthquake, Imperial Fault, Southern California: Implications for rupture segmentation and dynamics, *Bull. Seismol. Soc. Am.*, *103*(2A), 629640.
- Roten, D., K.B. Olsen, S.M. Day, Y. Cui, and D. Fah (2014). Expected seismic shaking in Los Angeles reduced by San Andreas fault zone plasticity, *Geophys. Res. Lett.*, 2769-2777, DOI: 10.1002/2014GL059411.
- Sagy, A., and E. E. Brodsky (2009), Geometric and rheological asperities in an exposed fault zone. *J. Geophysics. Res.*, *114*. B02301, doi:10.1029/2008JB005701.
- Sagy, A., E. E. Brodsky, and G. J. Axen (2007), Evolution of fault-surface roughness with slip, *Geology*, *35*(3), 283286, doi:10.1130/G23235A.1.
- Schmedes, J., R. J. Archuleta, and D. Lavalley (2010). Dependency of supershear transition and ground motion on the autocorrelation of initial stress, *Tectonophysics*, *493*, 222-235, doi:10.1016/j.tecto.2010.05.013
- Schmedes, J., R. J. Archuleta, and D. Lavalley (2012). A kinematic rupture model generator incorporating spatial interdependency of earthquake source parameters, *Geophys. J. Int.* *192*, 11161131, doi: 10.1093/gji/ggs021
- Shi, Z., and S. M. Day (2013), Rupture dynamics and ground motion from 3-D rough-fault simulations, *J. Geophys. Res. Solid Earth*, *118*, 11221141, doi:10.1002/jgrb.50094.
- Simons, M., Y. Fialko, and L. Rivera (2002), Coseismic deformation from the 1999 Mw 7.1 Hector Mine, California earthquake as inferred from InSAR and GPS observations, *Bull. Seismol. Soc. Am.*, *92*, 13901402.
- Song, S. G., and P. Somerville (2010). Physics-based earthquake source characterization and modeling with geostatistics, *Bull. Seismol. Soc. Am.*, *100*, no. 2, 482496, doi: 10.1785/0120090134.
- Song, S. G., A. Pitarka, and P. Somerville (2009). Exploring spatial coherence between earthquake source parameters, *Bull. Seismol. Soc. Am.*, *99*, no. 4, 25642571, doi: 10.1785/0120080197.
- Spotila, J. A., and K. Sieh (1995), Geologic investigations of a slip gap in the surficial ruptures of the 1992 Landers earthquake, southern California, *J. Geophys. Res.*, *100*, 543559.

- Vallée, M., M. Lands, N. M. Shapiro, and Y. Klinger (2008), The 14 November 2001 Kokoxili (Tibet) earthquake: High-frequency seismic radiation originating from the transitions between sub-Rayleigh and supershear rupture velocity regimes, *J. Geophys. Res.*, *113*, B07305, doi:10.1029/2007JB005520
- Xia, K., A. J. Rosakis, and H. Kanamori (2004), Laboratory Earthquakes: The Sub-Rayleigh-to-Supershear Rupture Transition, *Science*, *303*, Issue 5665, 1859-1861,
- Yue, H., T. Lay, J. T. Freymueller, K. Ding, L. Rivera, N. A. Ruppert, and K. D. Koper (2013), Supershear rupture of the 5 January 2013 Craig, Alaska (Mw7.5) earthquake, *J. Geophys. Res. Solid Earth*, *118*, 59035919, doi:10.1002/2013JB010594.

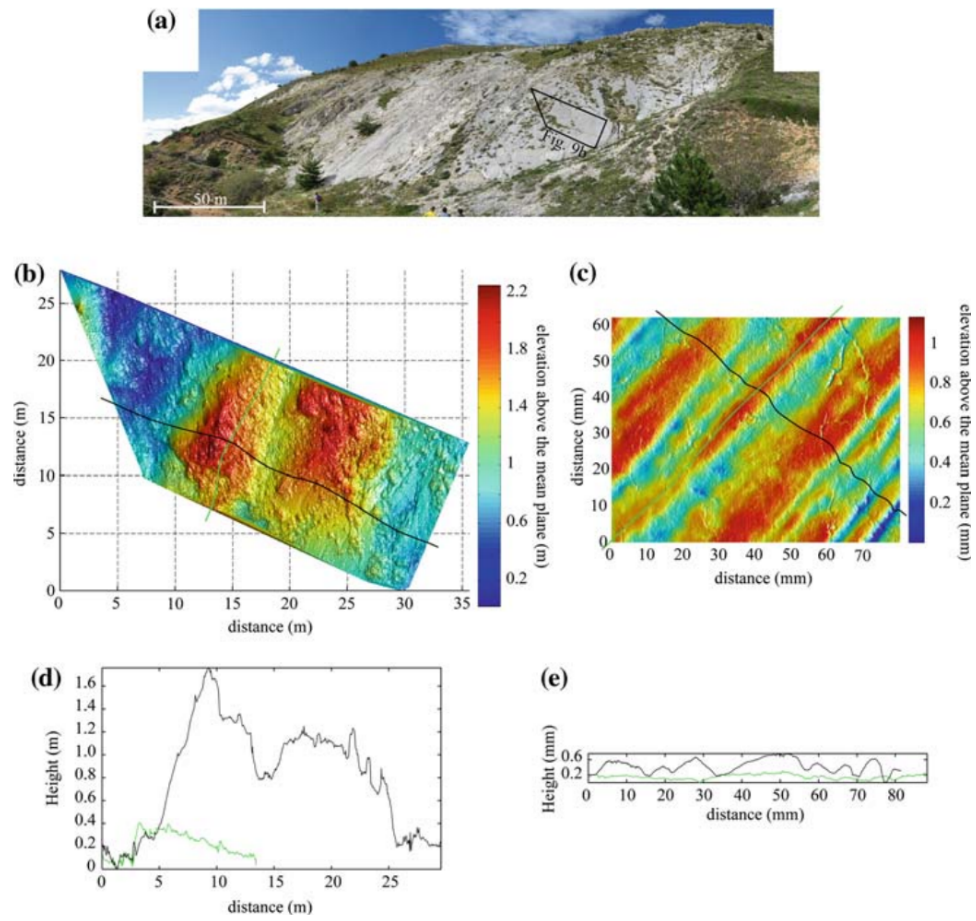


Figure 1.1: Figure 9 from *Candela et al.* (2009). 3-D scanner data of the Magnola fault slip surface at different scales.

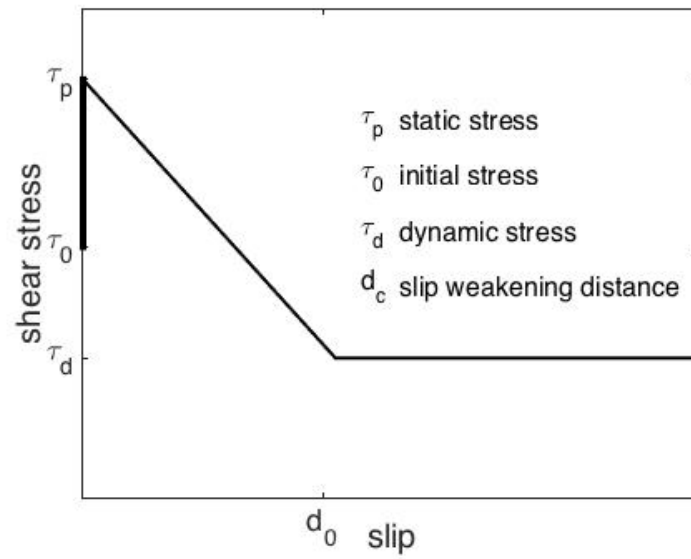


Figure 1.2: Illustration of Linear slip-weakening friction law, modified from *Andrews* (1976), τ_p , yield stress; τ_0 , initial stress, τ_0 , residual frictional stress, d_c , critical slip-weakening distance

Rupture Velocity and Directivity: Most important finite-source effect

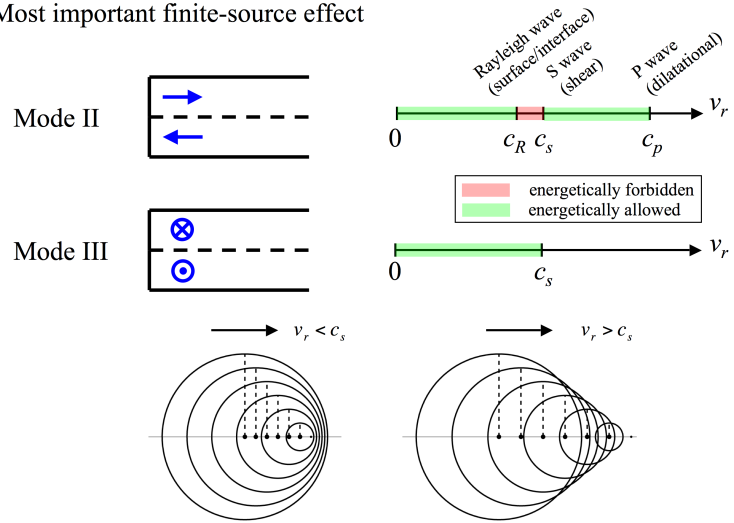


Figure 1.3: Supershear happens in Mode II rupture. Figure is from <https://pangea.stanford.edu/~edunham/research/supershear.html>

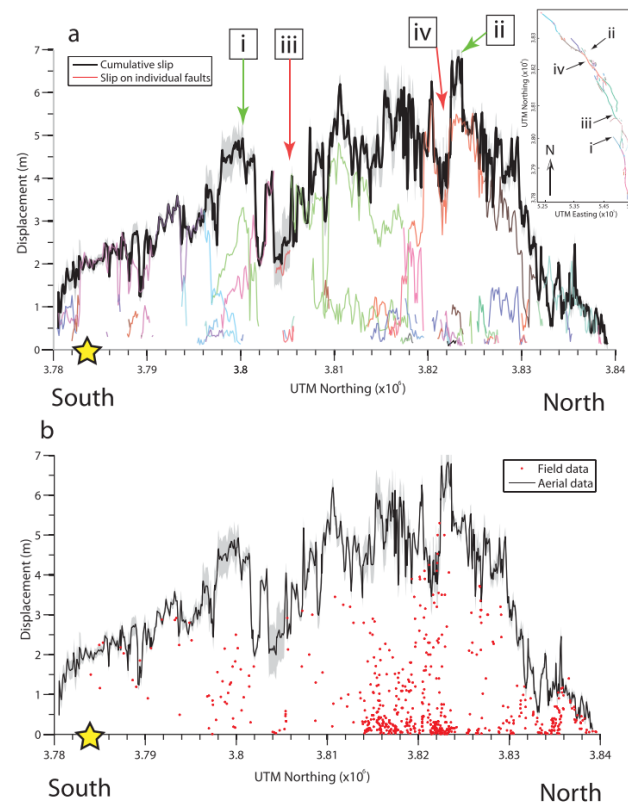


Figure 1.4: The accumulated slip in the damage zone in the 1992 Landers Earthquake. Figure 3 from *Milliner et al.* (2015).

Chapter 2

Earthquake Source Parameter Relationships from 3D Rough Fault Simulations

Earthquake ground motion simulations usually rely upon a kinematic description of the source in which the slip is parameterized by a few quantities (e.g., static slip, peak slip velocity, rupture velocity, rise time) that vary with position on the fault. The kinematic parameters are frequently represented as random fields, and dynamic rupture simulations have been used for estimating their distributional parameters. This approach has been carried out for planar fault models, but fault surface roughness modifies the rupture process and can affect the statistical distributions. We examine kinematic parameters derived from an ensemble of 3D dynamic simulations for faults with self-similar roughness, with RMS surface deflection, α , in the range 0.001 to 0.01 times the fault dimensions. Fault roughness reduces the amplitudes of rupture velocity, peak slip rate, rise time and total slip, and also changes the correlation of source parameter pairs. For a very smooth fault surface, with α equals to 0.001, the distribution of rupture velocity is concentrated near the Rayleigh wave velocity (the terminal velocity for mode II rupture); the distribution gradually broadens with fault roughness, and for a very rough case, α equals 0.009, the rupture velocity distribution is broadly dispersed over the range between 0.5 and 1.0 times the S wave velocity. Peak slip velocity and rise time

are broadly distributed for models at all roughness levels, but increased roughness shifts the distribution medians to lower values by about a factor of 1/3 (11 m/s to 4 m/s) for peak slip velocity, and about a factor of 2/3 (6 s to 4 s) for rise time, as roughness α varies over the 0.001-0.009 range. The distribution of static slip is broadened by increased roughness, and the median decreases by about a factor of 0.6 (5m to 3m). Total slip shows negative correlation with rise time on smooth faults, while the correlation becomes positive when the fault gets rougher. Stopping phases from the edge of the rupture surface become less important on rougher faults, because slip is more likely stopped by local geometry, leading to different dependency of source parameters on the distance to the nucleation center. Source parameters like total slip, peak slip rate and rupture velocity correlate with initial traction ratio, defined as the ratio of initial shear to normal traction on the fault surface. Two-point statistics show non-zero offset of the strong correlation peak between different source parameters. These results may provide guidance for the development of kinematic rupture generators for use in strong motion simulation.

2.1 Introduction

Earthquake ground motion simulations usually rely upon a kinematic description of the source in which the slip is parameterized by a few quantities (e.g., static slip, peak slip velocity, rupture velocity, rise time) that vary with position on the fault. The kinematic parameters are frequently represented as random fields, and dynamic rupture simulations have been used for estimating their distributional parameters. This approach has been carried out for planar fault models, but fault surface roughness modifies the rupture process and can affect the statistical distributions. We examine kinematic parameters derived from an ensemble of 3D dynamic simulations for faults with self-similar roughness, with RMS surface deflection, α , in the range 0.001 to 0.01 times the fault dimensions. Fault roughness reduces the amplitudes of rupture velocity, peak slip rate, rise time and total slip, and also changes the correlation of source parameter pairs. For a very smooth fault surface, with α equals to 0.001, the distribution of rupture velocity is concentrated

near the Rayleigh wave velocity (the terminal velocity for mode II rupture); the distribution gradually broadens with fault roughness, and for a very rough case, α equals 0.009, the rupture velocity distribution is broadly dispersed over the range between 0.5 and 1.0 times the S wave velocity. Peak slip velocity and rise time are broadly distributed for models at all roughness levels, but increased roughness shifts the distribution medians to lower values by about a factor of 1/3 (11 m/s to 4 m/s) for peak slip velocity, and about a factor of 2/3 (6 s to 4 s) for rise time, as roughness α varies over the 0.001-0.009 range. The distribution of static slip is broadened by increased roughness, and the median decreases by about a factor of 0.6 (5m to 3m). Total slip shows negative correlation with rise time on smooth faults, while the correlation becomes positive when the fault gets rougher. Stopping phases from the edge of the rupture surface become less important on rougher faults, because slip is more likely stopped by local geometry, leading to different dependency of source parameters on the distance to the nucleation center. Source parameters like total slip, peak slip rate and rupture velocity correlate with initial traction ratio, defined as the ratio of initial shear to normal traction on the fault surface. Two-point statistics show non-zero offset of the strong correlation peak between different source parameters. These results may provide guidance for the development of kinematic rupture generators for use in strong motion simulation.

Both kinematic and dynamic simulations have been used to compute earthquake ground motions. Kinematic simulations employ a phenomenological description of the source in which the slip function is often parameterized by a few quantities (e.g., slip, slip velocity, rupture velocity, rise time) that vary with positions. For simulations limited to relatively low frequencies, the slip parameters may be approximated on the basis of simplified theoretical models, or derived from slip inversions of past earthquakes (e.g., *Mai et al.*, 2010; *Roten et al.*, 2014; *Graves and Pitarka*, 2010). Other studies have examined the statistical structure of slip in past events; for example, *Song et al.* (2009) have studied the 2D spatial coherences between source parameters for both the 1999 Izmit, Turkey and 1992 Lander earthquakes. They found that total slip correlates to other parameters such as peak slip rate, rupture velocity and rise time. However, in order to sim-

ulate high frequency ground motion and achieve a quantitative and qualitative character comparable to observed ground motions, it is necessary to use a source model that represents short length-scale complexity of rupture that is not readily resolved observationally in inversions of individual earthquakes (e.g., *Mai et al.*, 2010; *Roten et al.*, 2014; *Graves and Pitarka*, 2010). Dynamic rupture models provide an alternative approach to ground motion simulation. In dynamic models, the fault surface geometry, initial stress state and the distributions of frictional parameters are required input. While these inputs are also poorly constrained by observation, the dynamic approach has the advantage that it can ensure that the resulting rupture kinematics and ground motions are consistent with fundamental physical constraints (e.g. physical limits on transient stress levels (e.g., *Roten et al.*, 2014), local energy conservation at the rupture front (e.g., *Olsen et al.*, 2009; *Day et al.*, 2012)). On the other hand, the dynamic approach has the disadvantage that it is difficult to adjust the input parameters to assimilate the information from ground motion records of past earthquakes, a process that is relatively straightforward for kinematic models (e.g., *Dreger et al.*, 2015). Dynamic simulations also entail nonlinear boundary conditions and are much more computationally complex than kinematic simulations. For these reasons, the kinematic approach to ground motion simulation predominates, especially in practical engineering applications.

Given the absence of direct observational constraints for short-wavelength structure of the source, the kinematic parameters are frequently represented as random fields. A promising means of combining the advantages of kinematic and dynamic approaches is to retain the kinematic formulation, but use ensembles of dynamic simulations to estimate the distributional parameters of those random field models. Versions of this procedure have been called pseudo-dynamic models. For planar models of faults, several such studies have been carried out (e.g., *Oglesby and Day*, 2002; *Guatteri et al.*, 2003; *Ripperger et al.*, 2007; *Song and Somerville*, 2010; *Schmedes et al.*, 2010, 2012). From 315 simulations, *Schmedes et al.* (2010) found that final slip amplitude is not related to local rupture velocity, but the latter is correlated with rise time. They also found rupture velocity is positively correlated with peak slip rate and source parameters are hypocenter-distance de-

pendent. Based on these source parameter relationships, *Schmedes et al.* (2012) have built kinematic rupture generators for the 1994 Northridge and 1989 Loma Prieta earthquake.

Surface roughness is a universal characteristic of natural faults. Roughness can be represented statistically as a random field that is approximately self-similar over many orders of magnitude in scale-length (e.g., *Candela et al.*, 2012; *Shi and Day*, 2013; *Dunham et al.*, 2011b) with a ratio of amplitude to length scale that typically falls into the range 10^{-3} to 10^{-2} (e.g., *Power and Tullis*, 1991). Geometrical complexities such as surface roughness can influence the spontaneous propagation of rupture in ways that may affect the slip parameters and enhance the generation of high frequency motions, as has been demonstrated by numerical simulations in 2D (*Dunham et al.*, 2011b; *Trugman and Dunham*, 2014) and 3D (*Shi and Day*, 2013). Enhanced generation of high-frequency radiation is a consequence of roughness-induced spatial fluctuations of both slip and rupture velocity (and direction), as expected on the basis of analytical studies (e.g., *Madariaga*, 1977; *Spudich and Frazer*, 1984). *Trugman and Dunham* (2014) have shown that, in 2D rough fault simulations, there is an anti-correlation between local slope of the fault profile and slip parameters like rupture velocity, peak slip rate and total slip, respectively. Similar relationships in 3D may provide a basis for the generation of kinematic models for use in ground motion simulations.

Here we examine kinematic parameters derived from an ensemble of 400 dynamic simulations for geometrically rough faults. Our goal is to get a better understanding of how the source parameters and their correlations are influenced by fault roughness in 3D. This study is in part an extension to 3D of the 2D study of *Trugman and Dunham* (2014), as required for practical application in engineering seismology. To isolate the effects of fault roughness, we only consider homogenous background stress, neglecting the effects of prestress heterogeneity that have been examined in previous studies for flat faults (e.g., *Ripperger et al.*, 2007; *Schmedes et al.*, 2010, 2012; *Song and Somerville*, 2010; *Andrew and Ma*, 2016; *Baumann and Dalguer*, 2014). We have computed the correlation coefficient and spatial interdependency between different pairs of source parameters. To support our

conclusions, we examine subsets of our datasets to confirm that the results are stable.

After checking the correlation coefficient of different source parameter pairs, we investigate how the initial traction distribution on rough fault varied with roughness, and how that initial traction condition alone (i.e., in the absence of geometrical roughness) would control source parameters, to provide some insight into the origin of the aforementioned source parameter correlations. In addition to examining parameter-pair correlations, we also consider the 2D spatial correlation of rupture velocity and peak slip rate, total slip and initial traction ratio, which are relevant for defining the spatial distribution of source parameters in kinematic rupture generators (e.g., *Song et al.*, 2009; *Schmedes et al.*, 2010).

2.2 Dynamic Rupture Models

In this study, we simulate in 3D, 400 strike slip dynamic ruptures whose fault dimensions are 60km(along strike) \times 30km (along dip). We tapered friction parameters on the fault near the boundary to stop the rupture before the rupture front hits the boundaries. The faults in this study are represented by 2D surfaces that are self-similar (with a short-wavelength cutoff), having a Hurst exponent equal to 1. On these surfaces, the short-wavelength cutoff and scale-length ratio define the roughness. The scale-length ratio is the ratio of the standard deviation of the fault surface from its mean plane to the scale length over which that measurement is taken (and the ratio is independent of the latter scale length). In this ensemble of simulations, the short-wavelength cutoff is 100m and the scale-length ratio varies from 0.001 to 0.01. The 2D self-similar fault profiles are constructed based on a Fourier transform method (e.g., *Andrew and Barall*, 2011; *Shi and Day*, 2013). We randomly choose 20 seeds to generate 20 fault surface realizations, and for each realization, the amplitude is scaled to five α values ranging from 0.001 to 0.01, so that, in total, we have 100 realizations of fault surfaces.

To investigate the importance of fault roughness, we isolate the roughness effect by adopting homogenous background stress. The initial normal stress is given

by $\sigma_{11} = \sigma_{22} = \sigma_{33} = 120MPa$ and the shear stress is assumed: $\sigma_{12} = 70MPa$ and $\sigma_{23} = \sigma_{31} = 0$ on the mean plane of the fault. The initial shear and normal tractions vary at different points on the fault, due to the fluctuations of fault orientation. To enable comparison with previous studies of flat faults, we only consider a slip weakening friction law, which implies there is no restrengthening when slip slows. The slip weakening distance is 0.4m. For simplicity, we use spatially uniform friction coefficient on the fault except for a tapering near the boundary and a minimum friction condition that prevents premature rupture at sharp releasing bends. On the fault, the dynamic friction coefficient is 0.525. To avoid any rupture prior to the arrival of waves from nucleation zone, we prescribe the minimum static friction coefficient for the whole fault plane determined as the value which is larger than the maximum ratio of the initial local shear traction to the normal traction at all points on the whole fault plane. On a flat fault, the ratio of shear and normal stress is 7/12. When we resolve the background stress onto 20 fault realizations at each fault roughness, the ratio of initial shear and normal traction can be up to 0.72, therefore we use 0.75 as our static friction coefficient, which is uniform on the fault. If we did not consider this, the fault would self-nucleate, rather than nucleated by our nucleation strategy.

Many studies of flat faults have shown that the dimensionless ratio S (Andrew, 1976a) is an important determinant of rupture behaviors. For the rough-fault simulations, we can define a hypothetical S_h value on the mean fault, S_h ($S_h = (\tau_s - \tau_0)/(\tau_0 - \tau_d)$, where τ_0 is the background shear stress and τ_s and τ_d are the peak and residual strengths), that is equal to 2.857. However the actual traction-based value, S_t , of that ratio ($S_t = (T_n \times \mu_s - T_s)/(T_s - T_n \times \mu_d)$, where T_s is local shear traction, T_n is local normal traction, and μ_s and μ_d are static and dynamic friction coefficient, respectively) varies spatially due to the fluctuations of fault orientations; S_t takes minimum value 0.146, and in a few places the initial shear traction approaches τ_d , so that S_t has no meaningful upper bound.

We initiate rupture by imposing a minimum rupture velocity (within the specified nucleation zone) to generate a rupture front that eventually reaches a point of instability and grows spontaneously. In this study, the nucleation zone

radius is 2.3km and a minimum rupture velocity is 1800km/s. For each realization of the fault geometry, we do simulations with the nucleation zone at each of four different locations on the fault. We use generalized finite difference method SORD (e.g., *Ely et al.*, 2008, 2009, 2010), based on a trial-stress formulation (*Shi and Day*, 2013), with a grid spacing 50m and time step 0.004s in our computations.

To ensure numerical accuracy, the cohesive zone where the rupture front evolves with time has to be resolved by enough grid points. As a first approximation, we can estimate the cohesive zone size Λ using the expression by *Palmer and Rice* (1973) which applies to a planar fault and is an upper bound in the sense that it represents the zero rupture-velocity limit λ_0 , whose length is around 210m. We can compare this preliminary estimate with the actual cohesive-zone dimension calculated for the dynamic rupture process in a representative case (with an intermediate value, 0.005, for α). For each time step, we calculate two contours on the fault surface, one given by the locations of rupture front on the fault, and the other one given by the locations whose accumulated slip equals the slip weakening distance. At a given time, the cohesive zone dimension is the minimum distance between these two contours (rupture time and weakening slip time). We have verified that the cohesive zone is always well resolved with at least 3 grid points (equal to 150m, which, as expected, and consistent with results in *Day et al.* (2005)) is somewhat less than the zero rupture-velocity estimate of 210m). Based on analysis in *Day et al.* (2005), this resolution is sufficient for our purposes (simulation errors in rupture velocity and slip less than about 2%, and in peak slip velocity less than about 10%).

2.3 Methods of Analysis

To provide reasonable statistical sampling, we have simulated 400 cases, as outlined in the previous section(20 fault shapes, 5 roughness amplitude, 4 nucleation sites), and for each simulation, we choose more than 2000 points on the fault to generate our database of slip parameters. The five roughness levels are given by α 0.001, 0.003, 0.005, 0.007 and 0.009, respectively. In our analysis, we focus on

the points in sub-shear rupture velocity regions, deferring analysis of supershear regions, anticipating that these regions may have a different pattern of behavior. We exclude the points in regions that are close to the hypocenter (at least 10km from the nucleation center) or domain boundary because the rupture behavior in these regions is heavily affected by assumptions known to be highly artificial.

The source parameters we investigate in this study are total slip, peak slip rate, rupture velocity and rise time at each point on the fault. The simulation directly provides rupture time and slip rate history at each point on the fault. To compute the rupture velocity, first we calculate the 2D gradient of rupture time (e.g., *Oglesby and Day, 2002*). The derivative is smoothed by filtering with a 2D $250\text{m} \times 250\text{m}$ box function. The inverse Euclidean norm of the gradient gives the local rupture velocity V_{rup} . The normalized rupture velocity V_{norm} is rupture velocity divided by the shear wave velocity.

To obtain a simplified representation of the slip, we fit the simulated slip rate at each point to a representative function form, and obtained the slip parameter from that function. *Tinti et al. (2005)* have discussed different types of slip rate functions, for example, boxcar, delta, Gaussian, truncated Kostrov and Yoffe functions. They proposed an analytical function that is good for dynamic rupture based on Yoffe function as used by *Nielsen and Madariaga (2003)*. This function is originally proposed by *Yoffe (1951)* for a steady-state solution of a mode I crack and extended to Mode II crack propagation by *Broberg (1978, 1999)* and *Freund (1979)*. This regularized Yoffe function proposed by *Tinti et al.* is parameterized by source parameters like rise time, peak time, and peak slip rate. By fitting Yoffe function, we can get total slip, peak slip rate and rise time. The main motivation for fitting the slip to the function before estimating the source parameters is to ensure a stable estimation of the rise time. That parameter can sometimes be difficult to define in a consistent and meaningful way from the original slip function, which may sometimes have a secondary slip episode, or exhibit a long decay time that includes very low-amplitude slip with little seismological significance.

In our analysis, we parameterize the slip rate history with Yoffe function at each point on the fault. In the simulations, we find that some points can rupture

again after the passage of an initial rupture pulse in rough fault simulations, and we only focus on the first peak of the slip rate if there are multiple peaks. The slip rate function is generated by convolving a Yoffe function with a half sine of width (*Schmedes et al.*, 2010),

$$\dot{s}(t) = ARe\left(\sqrt{\frac{T_0 + T_r - T_p - t}{t - T_0}}\right) * H(T_p - t)\sin\left(\pi\frac{t}{T_0}\right), \quad (2.1)$$

where T_0 is rupture time, T_r is rise time and T_p is peak time. First, we need to find the initial approximation of the parameters. The minimum time when the slip rate is non-zero is defined as the rupture time T_0 , and the interval time from the rupture time to the first time when the slip rate is not monotonically increasing is the peak time. The interval between the rupture time and the first time after the first peak when the slip rate equals zeros defines the rise time T_r . The peak slip rate is defined as the amplitude of the first peak. Total slip parameter is defined as the integral of the slip rate function from the rupture time to the rupture time plus rise time. We fit the slip rate function between T_0 to $T_0 + T_r$ to equation (1) by minimizing the integral of squared misfit by using downhill simplex method (e.g *Nelder and Mead*, 1965), and get the local minimum as a function of (T_0, T_r, T_p) . Figure 2.3 gives an illustration of slip rate function parameterization.

We focus on 1-point statistics in our data analysis. 1-points statistics are used to calculate correlation coefficient of two source parameters, regarded as random fields with zero offset. When calculating source parameter correlation coefficients in 1-point statistics, we choose to use Spearmans rank correlation coefficient. Usually Pearson correlation coefficient is used to calculate correlation coefficient based on two variable values. However, the Pearson correlation coefficient is sensitive to outliers in variables, which occasionally happens due to poor fitting in our data analysis; this is rare, but but can be significant. The correlation coefficient of two spatially distributed quantities, X and Y, can be computed by the equations.

$$\rho = E[(rg_X(\vec{u}) - m_{rg_X})(rg_Y(\vec{u}) - m_{rg_Y})]/(\sigma_{rg_X}\sigma_{rg_Y}). \quad (2.2)$$

The two random variable X and Y, can be any source parameters. rg_Y and rg_X are ranks converted from X and Y, and σ_{rg_X} and σ_{rg_Y} are the standard

deviations, respectively. \vec{u} is the position vector. We get the expectations in equation (2) estimated by averaging over a single simulation, and then forming a distribution of corresponding source parameter from the simulation ensembles. In this part of analysis, we investigate how source parameter distributions vary by the fault roughness level. This information provides guidance for development of kinematic rupture models, supplementing the similar relationships previously derived from smooth-fault models (*Schmedes et al.*, 2010, 2012). We also examine how source parameter distributions vary with the distance to the nucleation center, information also relevant for building practical kinematic models. How the source parameters and rough fault surface shape are related is also studied, and this leads to distributions of the ratio between shear and normal tractions and correlations of each source parameter and initial traction ratio at different fault roughness levels.

We also consider 2-point statistics of the source-parameter fields. Two-point statistics are used to calculate the correlation coefficient of two source parameters with non-zero spatial offset, which can be expressed by the equation.

$$\rho(\vec{h}) = E[(X(\vec{u}) - m_X)(Y(\vec{u} + \vec{h}) - m_Y)]/(\sigma_X\sigma_Y). \quad (2.3)$$

\vec{h} is separation vector between X and Y. The normalized covariance $\rho(\vec{h})$ is called a correlogram (*Goovaerts*, 1997). If fault roughness causes a delay of one source parameter relative to another as the rupture propagates, the 2-point statistics might capture that effect. To study 2-point statistics, we have selected a fixed size 2D region within each realization that is not affected by the nucleation regions or domain boundaries.

We have tested the robustness of all the statistics by applying the analysis to three different subsets of the simulations. The first test is to choose all realizations from two rather than four nucleation centers, and the second test is getting all realizations from fault surfaces derived from 10 seeds rather than 20 seeds, and the third one is randomly selecting 1000 points from the rupture plane rather than 2700. All three subset test cases give consistent results; the differences of results from subset test cases, and from all simulations taken together, are less than 1%.

2.4 Result

We first focus on how the parameters amplitudes distribute. The parameters we have studied are rupture velocity, total slip, rise time and peak slip rate. From Figure 2.4, the total slip on faults in the sub-shear areas from our simulations decreases with increased fault roughness (holding the initial stresses and friction coefficients fixed). When α equals 0.009, which corresponds to the roughest simulations in our datasets, the median of total slip is around 3m, however the median of total slip in the smoothest fault is around 5m. The rougher fault triggers larger fault drag force, making the total slip smaller. *Dieterich and Smith (2009)* also found reduced slip due to fault roughness. *Fang and Dunham (2013)* introduce the term roughness drag to describe the additional shear resistance to slip induced by fault roughness.

Rupture velocity, shown in Figure 2.4, has been normalized by shear wave velocity. As Figure 2.4 shows, rupture velocity at points on the fault is more widely distributed and smaller in amplitude with higher-amplitude fault roughness. When *Fang and Dunham (2013)* equals 0.001, the normalized rupture velocity is concentrated near 0.92, which corresponds to the Rayleigh wave velocity, the terminal velocity for mode II rupture. However the normalized rupture velocity spreads overall the interval from 0.5 to 1 when α equals 0.009. With higher amplitude fault roughness, the rupture velocity has larger variation because of the complications introduced by dynamic rupture interaction with local fault geometry. In addition to the increased variability, the averaged normalized rupture velocity also becomes smaller with increased roughness. We can interpret that result in terms of the roughness drag concept of *Fang and Dunham (2013)*. A rougher fault repartitions part of the energy otherwise available from the strain field into short wave-length strain fluctuations around the fault, leaving less energy available to extend the rupture. We also find an increased tendency for supershear rupture patches to arise under higher amplitude fault roughness. However, factors controlling occurrence of supershear are complicated, including, in particular, the degree to which the rupture interacts with the free surface. Supershear rupture in rough-fault simulations also involves supershear patches that may occur at a wide range of scales,

some of which may be of observational and engineering relevance and some not. In addition, supershear rupture is associated with systematic changes in the form of slip function (e.g., *Schmedes et al.*, 2010). For these reasons, we defer analysis of supershear rupture to a separate study.

Peak slip rate is another parameter we have analyzed. Peak slip rate amplitude decreases with increased fault roughness. When α equals 0.009, the median of peak slip rate is around 4m/s, which is much smaller than 11m/s, the median of peak slip rate when α equals 0.001. The rupture acceleration at local points has been affected by the dynamic rupture interacting with local fault geometry, which can be demonstrated by the variation of peak slip rate on the fault. From theory (Ida, 1973; Freund and Hutchinson 1985) and (flat-fault) simulation (*Day*, 1982; *Gabriel et al.*, 2013; *Bizzarri*, 2012), peak slip rate is expected to be approximately positively proportional to rupture velocity. Reduced rupture velocity leads to reduced peak slip rate. We did not consider off fault plasticity in our study, and this is a subject that still needs to be explored. Based on previous work (e.g., *Andrews*, 2005; *Duan and Day*, 2008; *Gabriel et al.*, 2013), our expectation is that introducing off-fault yielding would generally reduce rupture velocities and peak slip velocities, with little effect on their correlation structure.

Rise time on faults gets shortened with increased fault roughness. When α equals 0.009, the rise time centers around 6s. When α equals 0.001, the rise time focuses around 4s. With higher fault roughness, the stopping phase of fault dynamic rupture is more likely to be controlled by the local geometry rather than the stopping phase from the simulation domain boundary. For example, a bend may result in early termination of the slip pulse, either because sliding increases the normal stresses at the bend itself, or because rupture velocity change at the bend induces a stopping phase affecting nearby points.

In summary, the additional shear drag from fault roughness generally reduces rupture front acceleration, which slows the rupture process, generating smaller rupture velocity and smaller peak slip rate. The fault geometry influences the length of rise time because the rupture process is more likely be stopped by local fault geometry on a rough fault rather than stopping phase from domain boundary

on a flat fault. Larger fault roughness introduces some areas on which slip produces large normal-stress increases, which can easily stop the slip pulse, generating smaller rise time. Total slip is dependent on rise time and peak slip rate, therefore total slip is decreased with increased fault roughness. These three conditions are correlated, and those correlations should be taken into account in the development of kinematic rupture generators (i.e., for use in ground motion simulation). Our simulations provide information on both mean source parameter values and their correlation matrix, with potential applications in kinematic modeling of ground motion.

We next consider how the source parameters depend on the distance of the point from the nucleation centers, which is another important factor for the design of a kinematic rupture generator. We consider hypocentral distance intervals of 10km -20km, 20km-30km, and 30km-40km. In Figure 2.5, when α equals 0.001, peak slip rate increases with increased distance from the point to the hypocenter, normalized rupture velocity increases and concentrates more closely on 0.92, and rise time decreases. At low-amplitude roughness, the trend of source parameters can be explained well by a crack-like model governed by a slip weakening law, with the rupture stopped by the boundary. The rupture front accelerates from the hypocenter until it hits the boundary; therefore we have larger peak slip rate, larger rupture velocity and smaller rise time with larger distance from the point to the hypocenter. The analytical solution from *Kostrov* (1964) gives the slip history on a self similar circular shear crack which grows at a fixed rupture velocity in a prestressed homogeneous space. In that solution, the peak slip rate is expected to increase as the square root of distance from the point of rupture, as seen in the lower-roughness distribution in Figure 2.5. With high-amplitude roughness, this trend is less apparent, and disappears entirely for the roughest case. In the rougher cases, the source parameters are more controlled by dynamic interaction of slip pulse and local fault geometry, and a slip pulse stops more easily when it hits a local barrier. The diminished distance dependency for rough faults may need to be taken into account in the development of kinematic rupture generators.

The third part of the analysis examines the correlation of the source param-

eters with a property of the fault geometry that we refer to as the initial traction ratio. While our model uses a uniform initial stress tensor, the local shear traction and normal traction in this model are non uniform when the fault is rough, but are strongly dependent on the local geometry. In Figure 2.6, an example of a sine-shaped kink shows how normal traction and shear traction change through the releasing and restraining bends. We define the initial traction ratio as the ratio of shear traction (i.e., the amplitude of the shear traction vector) to normal traction at a point on the fault. For higher amplitude fault roughness, the initial traction ratio has slightly smaller mean and is more widely distributed relative to smooth faults. The initial traction ratio in 3D plays a role similar to that of the local slope in 2D rough fault simulations considered by *Trugman and Dunham (2014)*.

Starting with the calculated source parameters (rupture velocity, peak slip rate, rise time and total slip) at each fault point from each simulation, and the corresponding initial traction ratio at the same set of points, we calculate the correlation coefficient of each source parameter with the initial traction ratio in each simulation realization. The result is a distribution of 100 correlation coefficients at five different roughness levels. As shown in Figure 2.7, when α equals 0.009, total slip, rupture velocity and peak slip rate are high positively correlated with initial traction ratio. Positive correlation is weaker for smoother faults. When α equal 0.001, which is at the low end of observed roughness values, there is no correlation between total slip, rupture velocity, peak slip rate and initial traction ratio respectively. For all levels of fault roughness, there is no obvious correlation between rise time and initial traction ratio. When the fault is very rough, however, the other local source parameters are heavily influenced by initial traction ratio and interaction between rupture front and local geometry during rupture propagation. At a releasing bend, the initial traction ratio is high, which favors rupture nucleation. As rupture propagates, the rupture front accelerates faster along the releasing bends, and then rupture velocity, peak slip rate and total slip are larger compared to a flat fault. At a restraining bend, the initial traction ratio is low, and the three source parameters show a negative trend, so source parameters rupture velocity, peak slip rate and total slip are more positively correlated with initial

traction ratio in the high roughness cases. In contrast, rise time is controlled by positions of large local barriers. Since our fault geometry is randomly generated, after averaging of 100 realizations, there is no obvious correlation between rise time and initial traction ratio. To the extent that we can characterize the statistics of fault geometry, the correlation structure of the source parameter spatial distributions may be approximated from this type of correlation with initial traction ratio.

Next we examine how the correlation coefficients of different source parameter pairs distribute. Similar to foregoing analysis, source parameters at each point on the faults have been retrieved, then the correlation coefficients of different source parameter pairs have been calculated based on 80 simulation realizations at each of 5 different levels of fault roughness. In Figure 2.8, rupture velocity is positively correlated with peak slip rate at all levels of fault roughness, and both rupture velocity and peak slip rate are positively correlated with total slip at all levels of fault roughness. The positive correlation of rupture velocity and peak slip rate is supported by theoretical work for faults (*Ida, 1973; Freund and Hutchinson, 1985*). Because we already found that rupture velocity, peak slip rate and total slip are positively correlated with local traction ratio, the positive correlation coefficients in Figure 2.8 between rupture velocity and total slip, and between peak slip rate and total slip, were to be expected.

Rupture velocity and peak slip rate are each negatively correlated with rise time at low amplitude of fault roughness. The correlation becomes positive when fault roughness increases. On smooth faults, because the slip weakening law governs the rupture behavior, this negative relationship is related to the distance to the nucleation center. As the slip pulse propagates away from the hypocenter, peak slip rate and rupture velocity both becomes larger, and rise time becomes shorter, therefore the correlation coefficient is negative when the fault is smooth. When fault roughness increases, the slip pulse can be stopped before it hits the domain boundary. Rupture velocity and peak slip rate become more dependent on the local traction ratio. However, rise time does not show obvious correlation with initial traction ratio when fault is rough, but is more dependent on the nearby

geometry that may generate stopping phases (as noted earlier), and therefore the negative correlation becomes weakened.

Two-point statistics from dynamic simulations provide further information describing the rough-fault kinematics. As discussed in *Song et al.* (2009), spatial coherence estimates for slip in the 1999 Izmit earthquake and the 1992 Landers earthquakes show that a significant level of correlation between parameters not only exists at zero offset but also at nonzero offset distance. We examine the spatial coherence of initial traction ratio and source parameters total slip, peak slip rate, and rupture velocity in the datasets. For 2-point statistics study, we select fault areas on the right or left side of the fault surface which are away from the nucleation center, i.e., the analysis area in each case is entirely on one side of the nucleation zone, and the size is $30\text{km} \times 30\text{km}$. When analyzing spatial coherence, we include only the areas where have slipped more than 0.01m . In Figure 2.9, total slip, rupture velocity, peak slip rate and initial traction ratio distributions in the selected study area in one simulation as an example are illustrated in columns (a), (b), (c), (d). Fault roughness changes the rupture behaviors and leads to different source parameter distributions.

The correlogram is used to represent 2-point statistics, based on separation vector \vec{h} in equation (3), which is used to describe the offset distance on the fault. Figure 2.10 illustrates correlograms of different parameter pairs. The columns in Figure 2.10 represent correlograms of rupture velocity, total slip and peak slip rate with initial traction ratio, and rupture velocity with peak slip rate; each row represents a different fault roughness level. On smooth faults, all of rupture velocity, total slip and peak slip rate do not show strong correlations with initial traction ratio, no matter at zero offset or non-zero offsets, and there is no obvious maximum value. The initial traction ratios do not show many variations for smoother fault, and therefore the heterogenous source parameters mainly dominated by crack like model, should not correlate much with initial traction ratio distributions. On rougher faults, these three source parameters show larger correlations with initial traction ratio. When α equals 0.009, the correlogram maximum values are positive for aforementioned three pairs, but the maximum points are shifted by (0m,

0m), (0m, 0m), (0, -150m), respectively, which means rupture velocity does not change instantaneously with traction perturbations on fault surface, causing small non-zero offsets. Rupture velocity shows positive correlation with peak slip rate, and the maximum correlogram values increase with increasing α . At all α values, correlogram maximum values are always at zero offset for this parameter pair.

Better understanding of the 2-point statistics between source parameter pairs may be of importance to the design of kinematic rupture generators for the simulation of earthquake ground motion. While we have not yet explored this topic in a comprehensive way, the current results demonstrate that fault roughness is a significant element that may need to be considered in such studies.

2.5 Discussion

In this study, we use slip weakening friction law describing evolution, which does not allow self-healing slip pulse to propagate with low background shear stress. To make sure the rupture occurs at different rough faults, especially very rough fault, we need to choose a comparatively high background shear stress to break the additional dragness. It may be important to study source parameters relationships in comparable low background shear stress to further complete the study. Another assumption in this study for the material is elastic without plastic yielding. Off fault plasticity interacts with the rupture dynamics, which can limit the slip rate and rupture velocity (e.g. *Dunham et al.*, 2011a; *Ma and Andrews*, 2010; *Duan and Day*, 2008). If plasticity is included, changes of rupture properties like the peak slip rate, rupture velocity can lead to different distributions. It remains uncertain whether the inclusion of plasticity will also significantly modify the effects of surface roughness that we have found here, e.g., the roughness-induced shifts in distribution maxima and parameter pair correlations. [30] Another important factor to be considered is free surface. The existence of free surface changes the rupture dynamics, relative to models without a free surface as in this study. Free surface interactions often trigger supershear rupture in simulations of rupture propagation on simple geometrical fault (e.g., *Olsen et al.*, 1997; *Aagaard*, 2001; *Day*

et al., 2008; *Kaneko et al.*, 2008; *Olsen et al.*, 2008; *Kaneko and Lapusta*, 2010). In rough-fault simulations with a free surface, the rupture pulse reflected from the free surface interacts with the slip pulse on the fault, leading to different source parameter distributions compared with simulations without a free surface. Even though we have found that fault roughness can suppress this kind of supershear transition to some extent, the complexity of fault geometry in rough fault simulations sometimes triggers complicated slip pulses, which merge with the supershear slip pulse from the free surface, generating a very complicated rupture process (*Yao et al.*, 2016). The coupling of rupture process on the fault and free surface could lead to different strong motions. To have a more comprehensive study of source parameters correlations, free surface needs to be considered, especially for guidance of kinematic generator for ground motion prediction.

2.6 Conclusion

In this study, we examined hundreds of 3D dynamic rupture simulations on different realizations of self-similar rough faults. We first showed how the source parameter distribution varied with fault roughness level. Then we demonstrated how the source parameters distributions at different fault roughness level varied by the distance from the nucleation center. Later, we examined the correlation coefficients of source parameters with initial traction ratio distribution, and related them to the correlation coefficients of source parameter pairs. Finally, we investigated spatial coherence of source parameters.

The amplitude of source parameters like peak slip rate, rupture velocity, total slip and rise time in the sub-shear region decrease with increasing roughness on fault. Since the additional drag imposed by a rough fault increases with increasing roughness, the additional drag on fault prevents the acceleration of rupture pulse, leading to smaller rupture velocity, peak slip rate, rise time, therefore smaller total slip. At comparatively flat case, peak slip rate, rise time and rupture velocity distributions are dependent to the distance to the nucleation center. After the earthquake initiating, as the rupture front accelerates to faster velocity, the

rupture velocity gets faster, rise time becomes shorter, and the amplitude of peak slip rate is larger when the rupture propagate away from the nucleation center, which are behaviors of crack like rupture. When we increase the fault roughness level, the distance dependency is much weaker.

The rough fault model predicts that total slip is positively correlated with peak slip rate, and also positively correlated with rupture velocity at all levels of fault roughness. Total slip is negatively correlated with rise time when fault is smooth, and the correlation get weakened when the fault get rougher, and at very rough case, the correlation becomes positive. Rupture velocity is always positive correlated with peak slip rate at all levels of fault roughness. Rise time is negatively correlated with rupture velocity, peak slip rate at all fault roughness level, but at higher fault roughness levels, the absolute amplitude of negative correlation is smaller.

Total slip, rupture velocity and peak slip rate show positive correlation with initial traction ratio (ratio of initial shear to normal traction) on rough faults, and rise time does not show obvious correlation with initial traction ratio, in agreement with an analogous 2D result of *Trugman and Dunham (2014)*.

The maximum correlogram of rupture velocity and peak slip rate is positive and at zero horizontal offset for all roughness levels. When the offset is zero, rupture velocity and total slip show slightly positive correlation with initial traction ratio on smooth fault, and peak slip rate does not show correlation with initial traction ratio on smooth fault, which are consistent with what we have observed in Figure 2.8. The maximum correlogram of rupture velocity with initial traction ratio shows non-zero offset for rough faults.

2.7 Acknowledgements

This work was supported by NSF award EAR-1135455. Simulations were done using the generalized finite difference code SORD at Blue Waters super-computer at the National Center for Supercomputing Applications. Input files to reproduce the simulation results are available upon request.

Chapter 2, in full, is a reformatted version of a paper currently being prepared for submission for publication to Journal of Geophysical Research: Yao, Q. and S. M. Day, Earthquake Source Parameter Relationships from 3D Rough Fault Simulations. (2017). I was the primary investigator and author of this paper.

References

- Aagaard, B.T., Heaton, T.H., Hall, J.F. (2001). Dynamic earthquake ruptures in the presence of lithostatic normal stresses: implications for friction models and heat production. *Bull. Seismol. Soc. Am.* 91(6) 11,765-11,796.
- Aki, K., and P. Richards (2002). Quantitative Seismology, University Science Books, Sausalito, California, 700 pp
- Andrews, D. J. (1976). Rupture velocity of plane strain shear cracks, *J. Geophys. Res.*, 81, no. 32, 5679-5687, doi: 10.1029/JB081i032p05679.
- Andrews, D. J. (1976), Rupture propagation with finite stress in antiplane strain, *J. Geophys. Res.*, 81(20), 3575-3582, doi: 10.1029/JB081i020p03575.
- Andrews, D. J. (1999), Test of two methods for faulting in finite-difference calculations, *Bull. Seismol. Soc. Am.*, 89, 931-937.
- Andrews, D. J. (2005). Rupture dynamics with energy loss outside the slip zone. *J. of Geophys. Res.*, 110(B1), 307.
- Andrews, D. J., and M. Barall (2011). Specifying initial stress for dynamic heterogeneous earthquake source models, *Bull. Seismol. Soc. Am.*, 101, 2408-2417
- Andrews, D. J., and S. Ma (2016). Validating a dynamic earthquake model to produce realistic ground motion, *Bull. Seismol. Soc. Am.*, 106, no. 2, 665-672, doi: 10.1785/0120150251
- Baumann, C. and L. A. Dalguer (2014). Evaluating the Compatibility of Dynamic Rupture-Based Synthetic Ground Motion with Empirical Ground-Motion Prediction Equations, *Bull. Seismol. Soc. Am.*, doi:10.1785/0120130077
- Bizzarri, A. (2010). On the relations between fracture energy and physical observables in dynamic earthquake models. *J. Geophys. Res.*, 115, B10307. doi:10.1029/2009JB007027.
- Bizzarri, A. (2012). Rupture speed and slip velocity: What can we learn from simulated earthquakes? *Earth and Planetary Science Letters*, 317, 196-203.

- Broberg, K. (1978). Transient sliding motion. *Geophysical Journal of the Royal Astronomical Society* 52: 397432.
- Broberg, K. (1999). Cracks and Fracture. London: Academic Press.
- Candela, T., F. Renard, Y. Klinger, K. Mair, J. Schmittbuhl, and E. E. Brodsky (2012), Roughness of fault surfaces over nine decades of length scales, *J. Geophys. Res.*, 117, B08409, doi:10.1029/2011JB009041.
- Chester, F. M., and J. S. Chester (2000), Stress and deformation along wavy frictional faults, *J. Geophys. Res.*, 105(B10), 23,421-23,430, doi:10.1029/2000JB900241.
- Day, S. M. (1982). Three-dimensional simulation of spontaneous rupture: the effect of nonuniform prestress. *Bull. Seismol. Soc. Am.*, 72, 1881-1902.
- Day, S. M., L. A. Dalguer, N. Lapusta, and Y. Liu (2005), Comparison of finite difference and boundary integral solutions to three-dimensional spontaneous rupture, *J. Geophys. Res.*, 110(B12), 123, doi:10.1029/2005JB003813.
- Day, S. M., S. H. Gonzalez, S.H., R. Anooshehpour, J. N. Brune (2008). Scale-model and numerical simulations of near-fault seismic directivity. *Bull. Seismol. Soc. Am.* 98, 1186-1206.
- Day, S. M., D. Roten, and K. B. Olsen (2012). Adjoint analysis of the source and path sensitivities of basin-guided waves, *Geophys. J. Int.*, Vol 189, pp. 1103-1124, doi: 10.1111/j.1365-246X.2012.05416.x
- Dieterich, J. H., and D. E. Smith (2009), Nonplanar faults: Mechanics of slip and off-fault damage, *Pure Appl. Geophys.*, 166(1011), 1799-1815, doi:10.1007/s00024-009-0517-y
- Duan, B., and S. M. Day (2008), Inelastic strain distribution and seismic radiation from rupture of a fault kink. *J. Geophys. Res.*, 113(B12), 119. doi:10.1029/2008JB005847.
- Dunham, E. M., D. Belanger, L. Cong, and J. E. Kozdon (2011a). Earthquake ruptures with strongly rate-weakening friction and off-fault plasticity, part 1: Planar faults, *Bull. Seismol. Soc. Am.*, 101, no. 5, 2296-2307, doi: 10.1785/0120100075.
- Dunham, E. M., D. Belanger, L. Cong, and J. E. Kozdon (2011b). Earthquake ruptures with strongly rate-weakening friction and off-fault plasticity, Part 2: Nonplanar faults, *Bull. Seismol. Soc. Am.*, 101, no. 5, 2308-2322, doi: 10.1785/0120100076.

- Dreger, D.S., G.C. Beroza, S.M. Day, C.A. Goulet, T.H. Jordan, P.A. Spudich, J.P. Stewart (2015). Validation of the SCEC Broadband Platform V14.3 Simulation Methods Using Pseudospectral Acceleration Data, *Seismological Research Letters*, 86, p. 39-47, doi:10.1785/0220140118
- Ely, G. P., S. M. Day, and J.-B. H. Minster (2008). A support-operator method for visco-elastic wave modeling in 3-D heterogeneous media. *Geophysical Journal International*, 172, 331344.
- Ely, G. P., S. M. Day, and J.-B. H. Minster (2009). A support-operator method for 3-D rupture dynamics. *Geophysical Journal International*, 177, 11401150.
- Ely, G. P., S. M. Day, and J.-B. H. Minster (2010), Dynamic rupture models for the southern San Andreas Fault, *Bull. Seismol. Soc. Am.*, 100(1), 131150, doi:10.1785/0120090187.
- Fang, Z., and E. M. Dunham (2013). Additional shear resistance from fault roughness and stress levels on geometrically complex faults, *J. Geophys. Res.*, 118, no. 7, 36423654, doi: 10.1002/jgrb.50262.
- Freund, L. B. (1979). The mechanics of dynamic shear crack propagation, *J. Geophys. Res.* 84, 21992209
- Freund, L., and J. Hutchinson (1985), High strain-rate crack growth in rate-dependent plastic solids, *J. Mech. Phys. Solids*, 33(2), 169–191, doi:10.1016/0022-5096(85)90029-8.
- Ida, Y. (1973), The maximum acceleration of seismic ground motion, *Bull. Seismol. Soc. Am.*, 63(3), 959968.
- Gabriel, A. A., Ampuero, J. P., Dalguer, L. A., Mai, P. M. (2013). Source properties of dynamic rupture pulses with offfault plasticity. *Journal Geophysical Research*, 118,41174126. doi:10.1002/jgrb.50213.
- Goovaerts, P. (1997). Geostatistics for natural resources evaluation. *Soil Sci.* 126:364 Oxford Univ. Press, New York.
- Graves, R. W., Pitarka, A. (2010). Broadband ground-motion simulation using a hybrid approach. *Bull. Seismol. Soc. Am.*, 100(5A)(20952123.
- Guatteri, M., P. M. Mai, and G. Beroza (2004). A pseudo-dynamic approximation to dynamic rupture models for strong ground motion prediction, *Bull. Seismol. Soc. Am.*, 94, no. 6(20512063, doi: 10.1785/ 0120040037.
- Guatteri, M., P. M. Mai, G. C. Beroza, and J. Boatwright (2003). Strong ground-motion prediction from stochastic-dynamic source models, *Bull. Seismol. Soc. Am.*, 93, no. 1, 301313, doi: 10.1785/0120020006.

- Kaneko, Y., Lapusta, N., Ampuero, J.-P., 2008. Spectral element modeling of spontaneous earthquake rupture on rate and state faults: effect of velocity-strengthening friction at shallow depths. *J. Geophys. Res.* 113.
- Kaneko, Y., and N. Lapusta (2010), Supershear transition due to a free surface in 3-D simulations of spontaneous dynamic rupture on vertical strike-slip faults, *Tectonophysics*, 493(34), 272284, doi:10.1016/j.tecto.2010.06.015.
- Kostrov, B. V. (1964). Self-similar problems of propagation of shear cracks. *Journal of Applied Mathematics and Mechanics*, 28, 10771087.
- Ma, S., and D. J. Andrews (2010), Inelastic off-fault response and three dimensional dynamics of earthquake rupture on a strike-slip fault, *J. Geophys. Res.*, 115(B4), 116. doi:10.1029/2009JB006382.
- Madariaga, R. (1977). High-frequency radiation from crack (stress drop) models of earthquake faulting, *Geophys. J. Roy. Astron. Soc.* 51, no. 3, 625651, doi: 10.1111/j.1365-246X.1977.tb04211.x.
- Mai, P.M., Imperatori, W., Olsen, K. B. (2010). Hybrid broadband ground-motion simulations: combining long-period deterministic synthetics with high-frequency multiple S-to-S backscattering. *Bull. Seismol. Soc. Am.*, 100, 21242142. doi:10.1785/0120080194
- Nelder, J. A., and R. Mead (1965), A simplex method for function minimization, *Comput. J.*, 7, 308 313.
- Nielsen, S., and R. Madariaga (2003), On the self-healing fracture mode, *Bull. Seismol. Soc. Am.*, 93(6), 2375 2388, doi:10.1785/0120020090
- Oglesby, D. D., and S. M. Day (2002). Stochastic fault stress: Implications for fault dynamics and ground motion, *Bull. Seismol. Soc. Am.*, 92, no. 8, 30063021, doi: 10.1785/0120010249.
- Oglesby, D. D., P. M. Mai, K. Atakan, and S. Pucci. (2008), Dynamic models of earthquakes on the North Anatolian fault zone under the Sea of Marmara: Effect of hypocenter location., *Geophys. Res. Lett.*, 35, L18302, doi:10.1029/2008GL035037.
- Olsen, K. B. Akinci, A. Rovelli, A. Marra, F. Malagnini, L. (2006). 3D Ground-Motion Estimation in Rome, Italy, *Bull. Seismol. Soc. Am.*, 95, 133 - 146.
- Olsen, K. B., S. M. Day, J. B. Minster, Y. Cui, A. Chourasia, M. Faerman, R. Moore, P. Maechling, and T. Jordan (2006). Strong shaking in Los Angeles expected from southern San Andreas earthquake, *Geophysical Research Letters*, 33, L07305, doi:10.1029/2005GL025472.

- Olsen, K. B., S. M. Day, L. Dalguer, J. Mayhew, Y. Cui, J. Zhu, V.M. Cruz-Atienza, D. Roten, P. Maechling, T.H. Jordan, and A. Chourasia (2009). ShakeOut-D: Ground Motion Estimates Using an Ensemble of Large Earthquakes on the Southern San Andreas Fault With Spontaneous Rupture Propagation, *Geophysical Research Letters* 36L04303, doi:10.1029/2008GL036832.
- Olsen, K.B., Madariaga, R., Archuleta, R.J. (1997). Three-dimensional dynamic simulation of the 1992 Landers earthquake. *Science*, 278, 834838.
- Olsen, K.B., Minster, J.B., Cui, Y., Chourasia, A., Okaya, D., Maechling, P., Jordan, T. (2008). TeraShake2: spontaneous rupture simulations of Mw 7.7 earthquakes on the southern San Andreas fault. *Bull. Seismol. Soc. Am.*, 98 (3), 11621185.
- Palmer, A. C., and J. R. Rice (1973). The growth of slip surfaces in the progressive failure of overconsolidated clay, *Proc. Math. Phys. Sci.*, 332, 527548
- Power, W. L., and T. E. Tullis (1991). Euclidean and fractal models for the description of rock surface roughness. *Journal Geophysical Research*, 96, 415424.
- Ripperger, J., J. P. Ampuero, P. M. Mai, and D. Giardini (2007). Earthquake source characteristics from dynamic rupture with constrained stochastic fault stress, *J. Geophys. Res.*, 112, no. B04311, doi: 10.1029/2006JB004515.
- Ripperger, J., P. M. Mai, and J. P. Ampuero (2008). Variability of near-field ground motion from dynamic earthquake rupture simulations, *Bull. Seismol. Soc. Am.*, 98, no. 3, 12071228, doi: 10.1785/0120070076
- Roten, D., K.B. Olsen, S.M. Day, Y. Cui, and D. Fah (2014). Expected seismic shaking in Los Angeles reduced by San Andreas fault zone plasticity, *Geophys. Res. Lett.*, 2769-2777, DOI: 10.1002/2014GL059411.
- Schmedes, J., Archuleta, R. J., Lavallee, D. (2010). Correlation of earthquake source parameters inferred from dynamic rupture simulations. *Journal Geophysical Research*, 115, B03304. doi:10.1029/2009JB006689.
- Schmedes, J., R. J. Archuleta, and D. Lavallee (2012). A kinematic rupture model generator incorporating spatial interdependency of earthquake source parameters, *Geophys. J. Int.* 192, 11161131, doi: 10.1093/gji/ggs021
- Shi, Z., and S. M. Day (2013). Rupture dynamics and ground motion from 3-D rough-fault simulations, *J. Geophys. Res.*, 118, no. 3, 11221141, doi: 10.1002/jgrb.50094.
- Song, S. G., and P. Somerville (2010). Physics-based earthquake source characterization and modeling with geostatistics, *Bull. Seismol. Soc. Am.*, 100, no. 2, 482496, doi: 10.1785/0120090134.

- Song, S. G., A. Pitarka, and P. Somerville (2009). Exploring spatial coherence between earthquake source parameters, *Bull. Seismol. Soc. Am.*, *99*, no. 4, 25642571, doi: 10.1785/0120080197.
- Song, S. G., and L. A. Dalguer (2013). Importance of 1-point statistics in earthquake source modelling for ground motion simulation, *Geophys. J. Int.*, *192*, no. 3, 12551270, doi: 10.1093/gji/ggs089.
- Spudich, P., and L. Frazer (1984), Use of ray theory to calculate high-frequency radiation from earthquake sources having spatially variable rupture velocity and stress drop, *Bull. Seismol. Soc. Am.*, *74*(6)(20612082).
- Tinti, E., Fukuyama, E., Piatanesi, A., Cocco, M. (2005). A kinematic source-time function compatible with earthquake dynamics. *Bull. Seismol. Soc. Am.*, *95*, 12111223.
- Trugman, D. T., Dunham, E. M. (2014). A 2D pseudo-dynamic rupture model generator for earthquakes on geometrically complex faults. *Bull. Seismol. Soc. Am.*, *104*(1), 95112. doi:10.1785/0120130138
- Yao. Q., S. M. Day and Z. Shi, Supershear Transition Analysis in 3D Rough Fault Dynamic Simulations, Abstract 16-699 presented at 2016 Annual Meeting, SSA, Fall Meeting, AGU, Reno, Nevada, 20-22, April.
- Yoffe, E. (1951). The moving Griffith crack, *Phil. Mag.* *42*, 739750

Table 2.1: Model Parameters

Parameter	Value
P Wave Velocity (<i>km/s</i>)	6000
S Wave Velocity (<i>km/s</i>)	3464
Density (<i>kg/m³</i>)	2670
Dynamic Friction Coefficient	0.525
Static Friction Coefficient	0.75
Slip Weakening Distance(m)	0.2
Normal Stress (MPa)	70
Shear Strss (MPa)	120
Nucleation Width (m)	4000
Time Step Size (s)	0.004
Gird Size (m)	50
Number of Fault Surface Seeds	20
Number of Fault Roughness Levels	5
Number of Possible Nucleation Centers	4

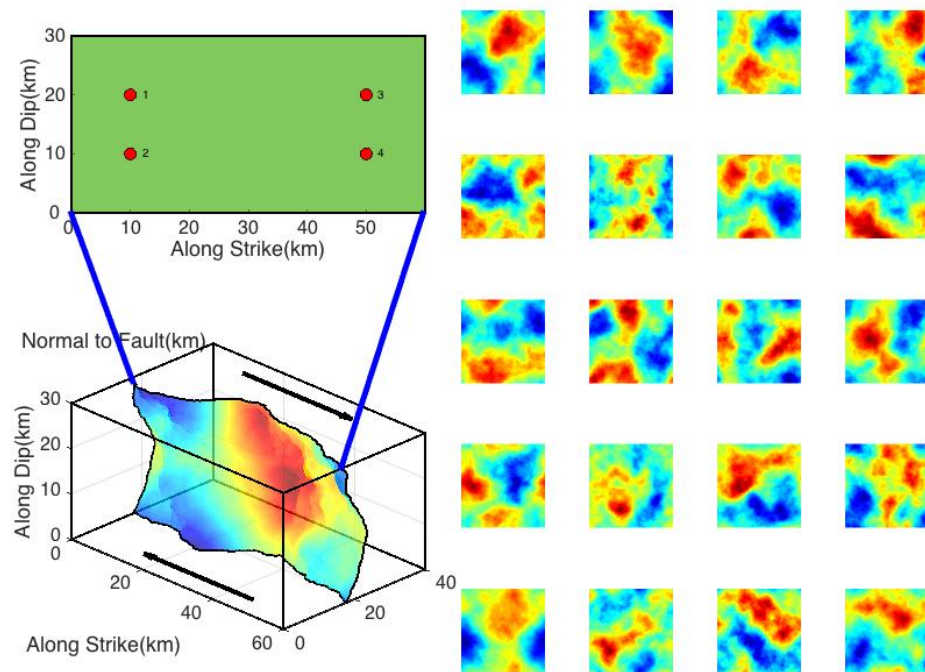


Figure 2.1: Model geometry and dimensions for 3D earthquake dynamic rupture. Ruptures are nucleated at 4 possible nucleation centers on the fault plane. (right) Examples of 20 random rough fault surfaces. We apply different amplitude to the surface elevation to adjust for the fault roughness level.

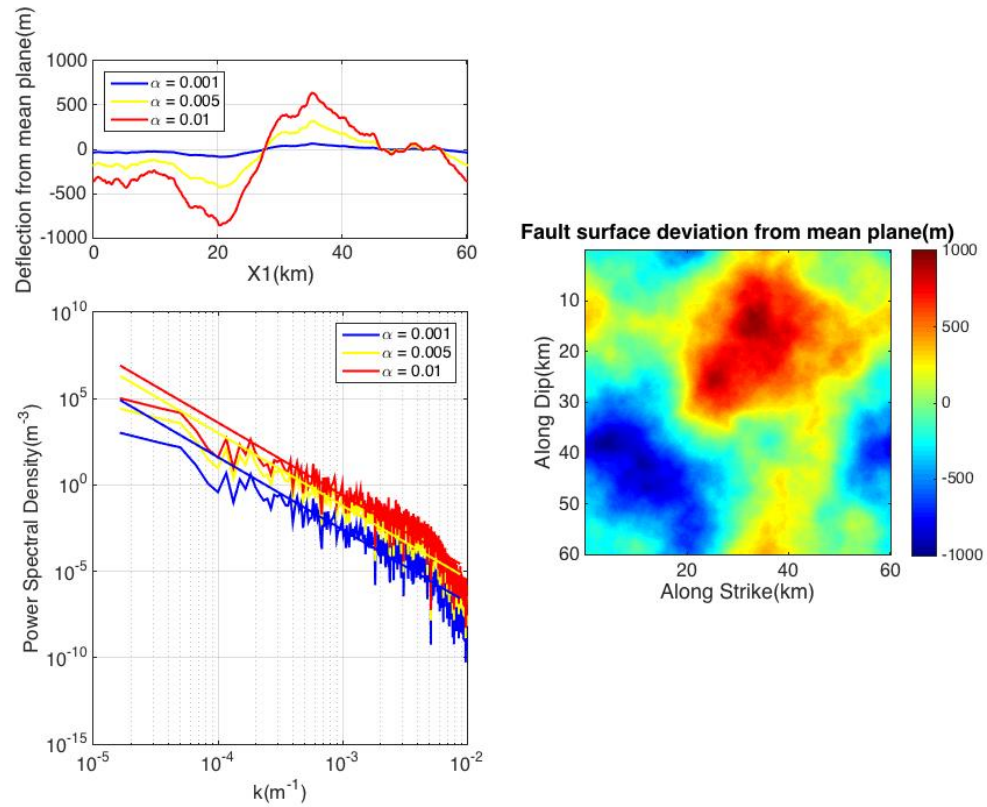


Figure 2.2: Example of 1d fault profiles selected from surface in (right) with α equals 0.001, 0.005 and 0.01 and their power spectral densities. (right) One 2D rough fault surface with minimum wavelength 200m.

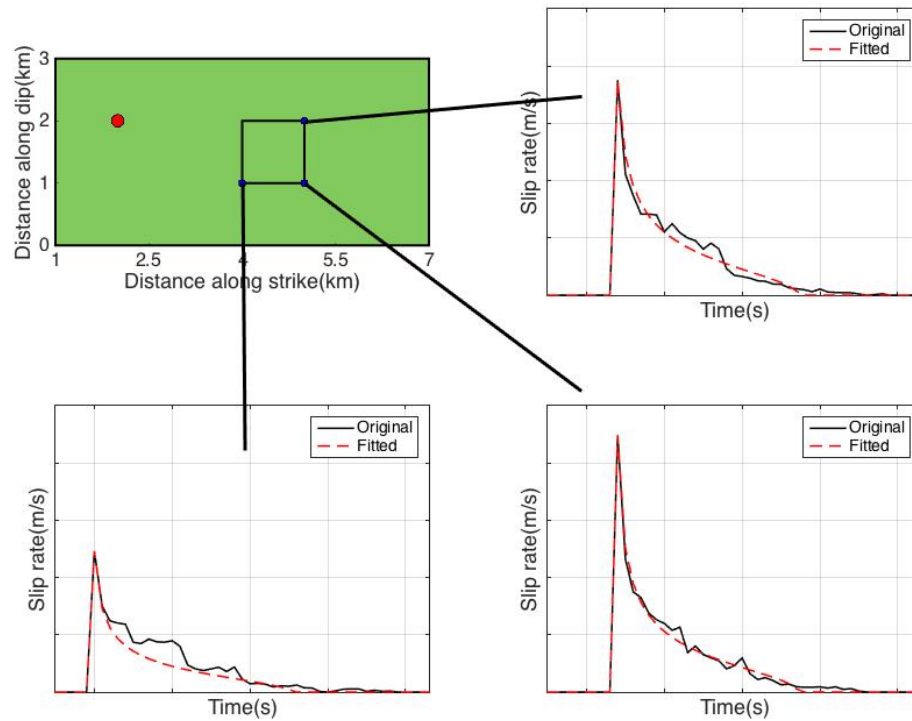


Figure 2.3: Illustration that shows how to fit the slip rate function. (left) top shows the fault plane with the red circle as hypocenter. (left) bottom, (right) top and (right) bottom show computer slip rate (black) and fitted slip rate (red) from three selected points on the fault plane (three blue points in (left) top). The slip rate function fit procedure is similar to *Schemedes et al. 2010*.

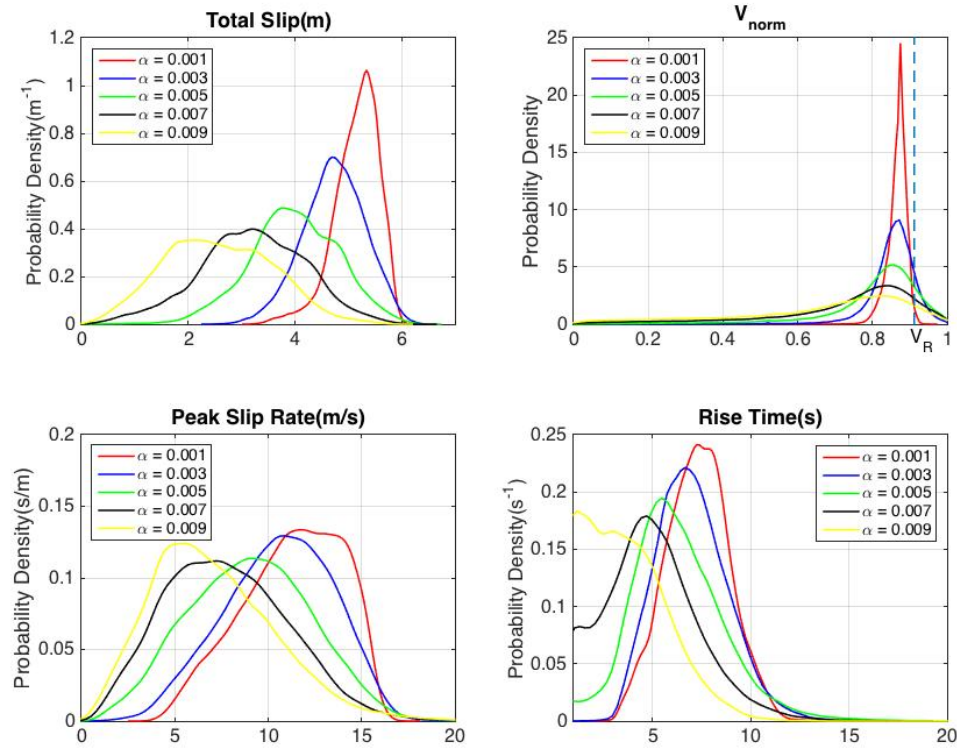


Figure 2.4: Probability density function for various source parameters computed on points for each dynamic rupture simulation, which is dependent on fault roughness amplitude. We only consider points on the fault plane that have slipped and with sub-shear rupture velocity. (left) Top shows total slip, and bottom shows peak slip rate. (right) shows normalized rupture velocity, V_R is Rayleigh wave velocity. Bottom shows rise time.

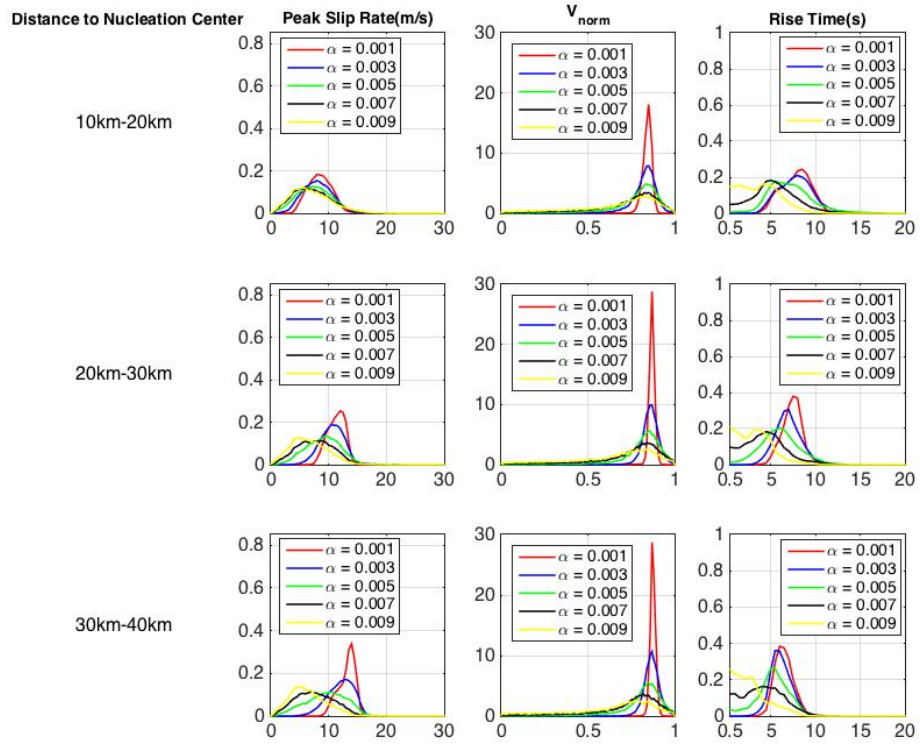


Figure 2.5: Probability density function for various source parameters with different fault roughness levels computed on points. The probability density function is dependent on the distance to the nucleation center. We only consider sub-shear and slipped regions in each simulation. (left column) shows peak slip rate, (middle column) shows normalized rupture, and (right column) shows rise time.

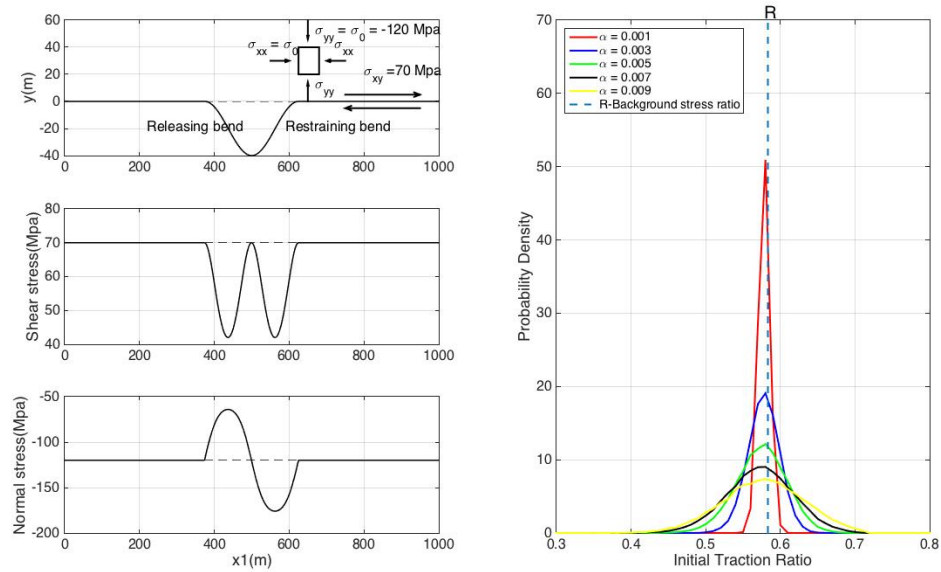


Figure 2.6: (left) Example of 1D sin kink, the initial homogeneous background normal and shear stress are applied in the right lateral direction. Normal tractions increase at releasing bends and reduce at restraining bends. (right) Probability density function of ratio of initial shear traction to initial normal traction at different fault roughness levels. Green dashed line is the ratio of initial background shear stress to initial background normal stress.

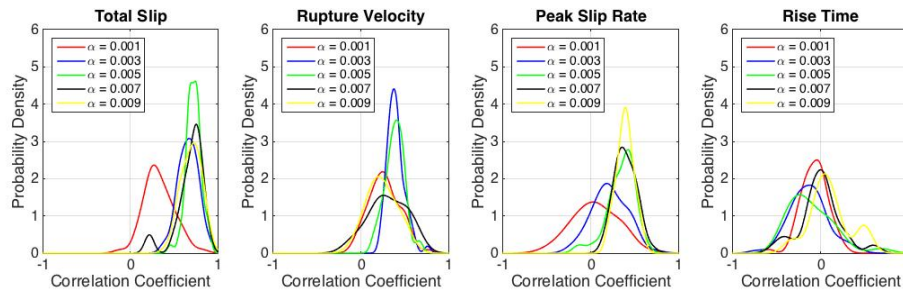


Figure 2.7: Variation of correlation-coefficient distribution of source parameter and initial traction ratio at different fault roughness levels. Total slip, rupture velocity and peak slip rate show positive correlation with initial traction ratio at all levels of rough faults. Rise time shows no correlation with initial traction ratio.

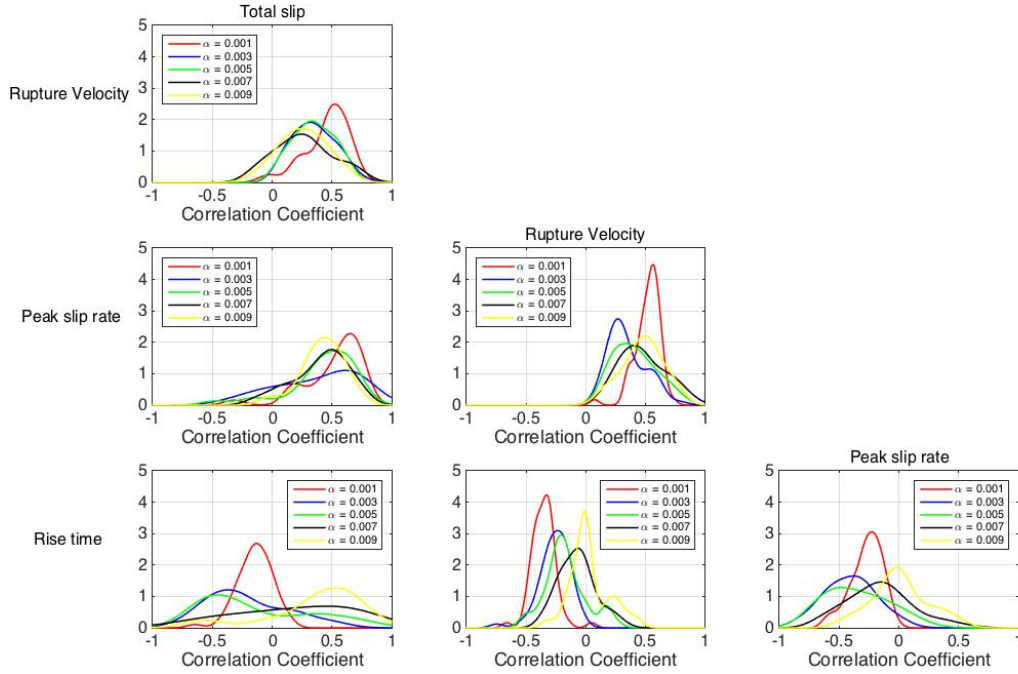


Figure 2.8: Variation of correlation-coefficient distribution of source parameter pairs with different fault roughness level. The main parameters are total slip, peak slip rate, rupture velocity and rise time. Total slip shows positive correlation with peak slip rate, rupture velocity when α is non-zero. The correlation of rise time and total slip is negative when α is small, and become positive when α is large. Peak slip rate shows high correlation with rupture velocity, and rise time is negatively correlated with rupture velocity and peak slip rate at all fault roughness level.

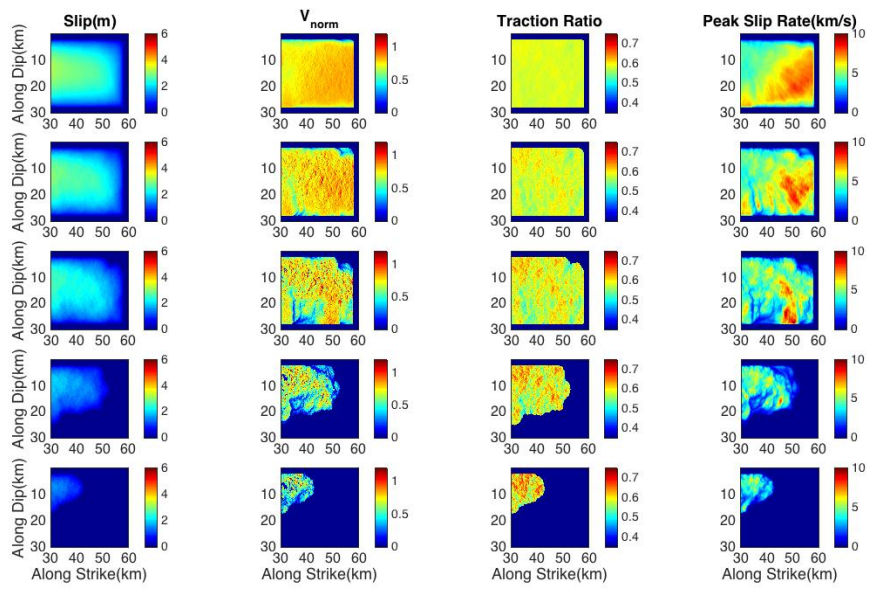


Figure 2.9: Example of slip, normalized rupture velocity, initial traction ratio and peak slip rate distributions on fault plane in one realization. From top to bottom, the fault roughness level changes from 0.001, 0.003, 0.005, 0.007 to 0.009.

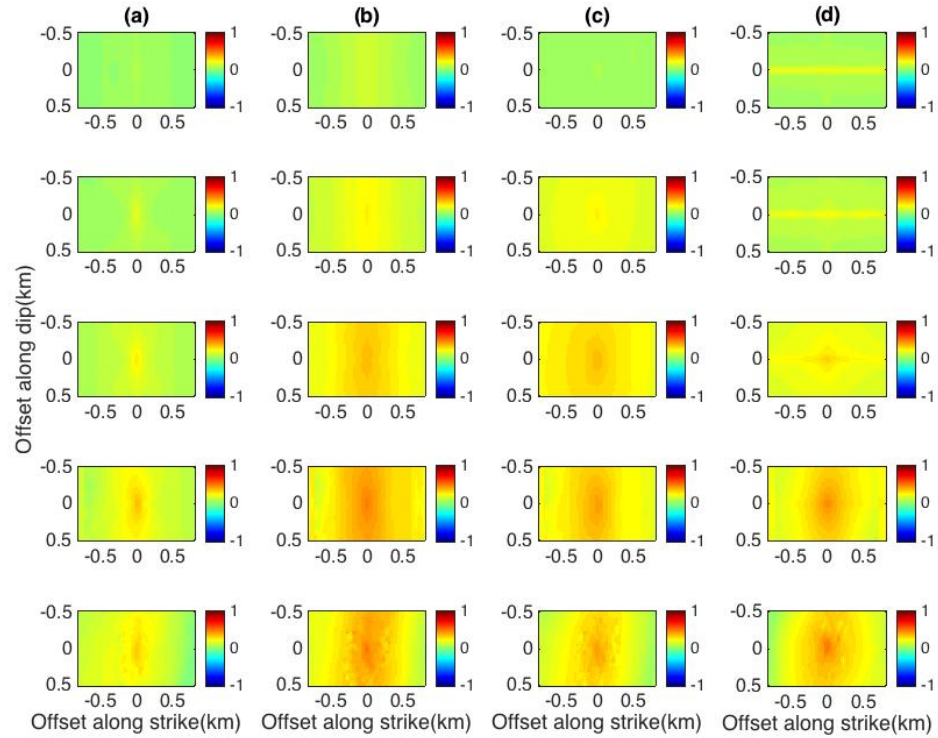


Figure 2.10: Spatial coherence of different source parameters. (a), (b) and (c) are correlogram distributions of rupture velocity, total slip and peak slip rate with initial traction ratio. (d) shows correlogram distributions of rupture velocity with peak slip rate. From top to bottom, the fault roughness level changes from 0.001, 0.003, 0.005, 0.007 to 0.009.

Chapter 3

Supershear Transition Analysis in 3D Rough Fault Dynamic Simulations

Supershear rupture propagation has been documented from seismic observations of natural faulting and observed in laboratory experiments. Rough-fault dynamic simulations approximate the geometric complexity seen at all scales on natural faults. Such simulations in 2D have shown that increasing fault roughness favors the initiation of supershear episodes, while disfavoring their growth to large area. We consider similar models in 3D, analyzing supershear transitions in a database of more than 500 3D rupture simulations. Triggering mechanisms for supershear rupture on rough faults in 3D include several already found in planar-fault simulations, including free-surface-triggered supershear, favorable stress heterogeneity on releasing bends, and stress focusing near restraining bends. We find two distinct classes of supershear events. The first class comprises buried supershear episodes, i.e., that are disjoint from the free surface. For this class, our results roughly mirror previous 2D results, in that moderate levels of fault roughness (up to $\alpha = 0.005$ in our models) favor occurrences of supershear rupture, though this effect appears to saturate at higher roughness level. These buried supershear events tend to be short bursts, with many probably below the size threshold for observability. Events of the second class, supershear transitions induced by free-surface

interactions, contrast sharply with those of the first, in that the surface supershear episodes are favored by smoother fault surfaces, and tend to be sustained over large areas. These surface events are more frequent, more likely to have seismically observable consequences (because of their size and shallowness), and more consistent with empirical evidence that supershear transitions are favored on simpler, smoother fault traces. An approximation to the rough model in which initial shear and normal traction variations associated with fault roughness are mapped onto a flat fault, gives similar results, but slightly over-predicts rupture velocity, a result that can be qualitatively understood as the result of the neglect in the approximate model of so-called roughness drag.

3.1 Introduction

Supershear ruptures have been investigated analytically (e.g., *Burridge, 1973; Freund, 1979*), numerically (e.g., *Andrews, 1976; Day, 1982*) and experimentally (e.g., *Xia et al., 2004*). Such ruptures have also been observed for natural earthquakes, especially large strike slip earthquake, including, for example, the 1979 Imperial Valley earthquake (*Archuleta, 1984*), the Izmit earthquake (*Bouchon et al., 2000, 2001*), the 2002 Denali, Alaska earthquake (*Dunham et al., 2004*), the 2001 Kunlunshan earthquake (*Bouchon and Vallée, 2003; Robinson et al., 2006; Vallée et al., 2008*), and the 2013 Craig, Alaska earthquake (*Yue et al., 2013*). The numerical study of *Andrews (1976)* shows a mechanism for the supershear transition in Mode II rupture under slip weakening friction. In that mechanism, a daughter crack is initiated by shear stress at the S wave arrival ahead of the main rupture on fault plane. *Andrews's* study shows that, on a planar fault with uniform stress, strength and friction parameters, the occurrence of the supershear transition is governed by the S ratio, defined by $S = (T_s - T_0)/(T_0 - T_d)$, where T_s is the static strength, T_0 is the background shear stress, and T_d is the dynamic strength. When the S ratio is smaller than 1.77, the supershear transition happens after subshear rupture has propagated a sufficient distance. *Dunham (2007)* shows that the critical value of the S ratio for a homogeneously prestressed fault in 3D

models is 1.19, which means the 3D models generally require a larger prestress to trigger the supershear transition than 2D models do.

Several numerical studies show that supershear rupture can happen when there is a heterogeneous stress condition or strength condition on a planar fault (*Liu and Lapusta, 2008; Dunham et al., 2003*). *Schmedes et al. (2010)* demonstrated that a highly auto-correlated heterogeneous background stress field enhances supershear transitions. Fault geometry which contributes to fault complexity could be a potential factor to trigger supershear rupture. In support of that possibility, note that in the 2001 Kunlun earthquake, the supershear transition location corresponds to a geometrically complex area, as found on the basis of seismic observations (*Vallée et al., 2008*).

Natural faults show different degrees and types of geometrical complexity from large scale features such as branching, to small scale features such as short-wavelength deflections of the fault from the mean fault surface (e.g., *Power and Tullis, 1991; Sage and Brosky, 2009; Candela et al., 2009, 2012*). Between seismic events, the geometric irregularities of the fault plane generate local variations of the stress distribution around the fault. During an earthquake, the fault roughness may have a significant influence on the rupture processes (*Chester and Chester, 2000*). Local complex geometry perturbs the dynamic stress field as rupture propagates along a rough fault, and rupture fronts rapidly accelerate or decelerate, leading to high-frequency radiation and resulting in heterogeneous distributions of slip rate, peak slip rate and final slip. These effects of self-similar fault roughness on dynamic rupture propagation have been numerically investigated in both 2D and 3D (*Dunham et al., 2011b; Shi and Day, 2013*).

Supershear transitions have been observed in 2D plane strain dynamic simulations on rough faults (*Bruhat et al., 2016*), which documented effects of background shear stress level and roughness level on occurrence of supershear in simulations of dynamic ruptures. The 2D simulations of rupture on rough faults provide a starting point for understanding super-shear transitions in strike slip earthquakes. However, in natural seismic events, free-surface interactions and 3-D seismic wave propagation effects may play important roles, and those effects can

only be accounted for in 3D simulations. Furthermore, barriers to slip formed by fault-surface irregularities can be expected to respond differently in 3D than in 2D. For example, the fault-surface irregularities in 3D may be surrounded and bypassed by rupture, whereas rupture can only overcome barriers in 2D models by jumping over them.

Kinematic earthquake models (i.e. source models defined directly by a model of fault slip) are usually applied to efficiently compute ground motion simulations (*Herrero and Bernard, 1994; Guatteri et al., 2003, 2004*). Those models can be informed by results and insights from dynamic rupture models (*Oglesby and Day, 2002; Schmedes et al., 2010; Song et al., 2009; Guatteri et al., 2003*), which may improve the formulation of the kinematic models and help avoid misleading predictions. For example, the degree of correlation assumed between slip parameters can affect the amount of variance in an ensemble of ground motion predictions, as noted by (*Oglesby and Day, 2002*). In their dynamic simulations, they find significant correlation between local values of stress drop and rupture velocity, suggesting that it may not be appropriate to vary those parameters independently in a kinematic simulation ensemble. Rupture velocity heterogeneity retrieved from dynamic rupture models also informs kinematic methods (*Graves and Pitarka, 2010; Crempien and Archuleta, 2015*).

In this work, we examine the supershear transition in several sets of 3D strike slip dynamic rupture simulations on rough fault surfaces governed by a slip weakening friction law. The simulations are done using the SORD (*Ely et al., 2008, 2009; Shi and Day, 2013*) code (a finite difference method generalized to permit meshes that are irregular, though structured). From the simulated datasets, we demonstrate different types of supershear triggering mechanisms that operate in 3D on a rough fault, such as a daughter crack generated by favorable geometry, focusing effects produced by unfavorable geometry and free-surface triggering. We also explore the effect of fault roughness level and background shear stress level on both the frequency of occurrence and spatial extent of supershear rupture episodes. Then, we compare those results with the rupture behaviors of what we call a pseudo-stress model. The latter uses the fault surface-resolved stress state induced

by fault roughness, but applies those shear and normal stresses to a planar fault. The dynamics of that model are broadly similar to those of the rough-fault model, but, because the pseudo-stress model neglects roughness drag (*Fang and Dunham, 2013*), the pseudo-stress approximation predicts generally higher rupture velocity, larger rupture area and higher probability of supershear transitions than does the rough-fault model. Finally, we examine how different nucleation strategies, and different fault domain lengths and widths, influence the occurrence and size of connected supershear patches.

3.2 Dynamic Rupture Models

In this study, we develop several sets of 3D strike slip dynamic rupture simulations on rough fault models. The bulk of the analysis is based on a simulation ensemble called SET1 (shown in Table 3.2). The fault geometry is 30km (length) \times 15km(width), and we have fixed boundaries at four sides to avoid slip outside the fault plane. The model setup is in Table 3.1. There is no free surface in the SET1 model. The reason for suppressing the free surface is that we have found that supershear transitions associated with the interaction of rupture with the free surface have a very different character from those transitions triggered on fault patches that occur at depth, isolated from the free surface. The SET1 ensemble permits us to study the latter without interference from the former.

To examine free surface effects, we introduce another set of simulations called SET2, which have the same model setup, except that SET2 simulations have a free surface at the top, rather than fixed boundary (the other three sides still have the fixed boundary condition, as in SET1). Keeping SET2 very similar to SET1 helps clarify the role of free surface interactions, but the absence of any depth dependence in the frictional or loading parameters leads to a strong rupture pulse at the free surface breakout of the rupture, which may be affected by this simplification. Therefore, instead of a homogenous friction coefficient on the fault plane, the third set of simulations, SET3, adopts tapered friction parameters near the free surface. The dynamic friction coefficient μ_d increases linearly from 0.525

at 1.5 km depth to 0.75 at 0.75km depth, and remains at 0.75 from 0.75km to free surface. The static friction value is constant at 0.75, so this has the effect of producing smaller stress drops near the free surface, which may be more realistic compared to the SET2 assumption of uniform stress drops at different depths.

Since the occurrence of supershear transients is favored at higher shear stress levels [Bruhat et al., 2016], we also test the sensitivity of supershear to different levels of background shear stress. Therefore, SET4 adapts background shear stress of 71MPa instead of the value of 70MPa used in the first three ensembles, which decreases the S ratio by 16.87% (from 2.857 to 2.375), and the actual S value on the rough surface is of course variable, and here we cite as a representative value the S as calculated for the mean plane of the fault).

In an approximate sense, we can think of the geometrical roughness as having two somewhat distinct effects. The first is a static perturbation to the initial tractions, and the second is the geometrically induced drag that occurs during rupture and sliding on the irregular surface. To separate these effects, another set of simulations, SET5, uses the same initial resolved traction (shear and normal) distributions as in SET1, but eliminates the rough geometry and just applies these initial conditions to a planar fault.

Another set of simulations, called SET6, entails expanding the 30 km length of simulation domain used in SET1 to 90km. The purpose of SET6 is to study how rupture length affects the occurrence and connectivity of supershear patches. Finally, we introduce SET7 in order to study whether different nucleation strategies and fault plane width play an important role in controlling supershear patches. In SET7, the simulation domain size is 60km(length) * 30km(width) and rupture is initiated by applying an initial minimum rupture velocity near the hypocenter. Ensembles SET4-SET7 were all done without a free surface, to facilitate direct comparison with SET1. The simulation ensembles in this study are summarized in Table 3.2.

In each set of simulations (except SET5) the fault is a 2D self-similar surface that is band-limited. The fault roughness level is defined as the ratio of root-mean-

square (RMS) deviations from the mean plane to the fault length L :

$$\alpha = \frac{h_{RMS}}{L}. \quad (3.1)$$

The level of fault roughness has been found to be related to the maturity of a fault, as measured by total accumulated slip (e.g., *Sage and Brodsky, 2009; Brodsky et al., 2011*), with high values of α corresponding to immature (low-slip) faults. Most natural faults are characterized by α ranging from 0.001 to 0.01 (*Power and Tullis, 1991; Andrew and Barall, 2011*). For SET1-SET5, we generate 20 random realizations of a self-similar fault surface, and scale each to 5 different roughness levels α from 0.001 to 0.009, which form an ensemble of 100 fault model realizations. In SET6-SET7, we scale the 20 realizations only to the single level $\alpha = 0.005$. In SET1 and SET7, we further expand the ensembles by selecting four nucleation centers for each fault model realization, to obtain 400 simulations for SET1 and 80 simulations for SET7. The fault surfaces are constructed by the Fourier transform method described in *Shi and Day (2013)*. Finally, in each case, the 2D rough fault is embedded into the 3D homogeneous medium.

The initial stress state resolves to uniform normal and shear stresses of 120 MPa and 70MPa, respectively, on the mean plane of the fault (71 MPa initial shear in the case of SET4). This simplified initial stress state permits us to isolate the geometrical effects on rupture dynamic, whereas the stress-heterogeneity effects, in the absence of geometrical complexity have been the focus of previous studies (*Schmedes et al., 2010; Oglesby and Day, 2002*). Nonetheless, the initial shear traction and normal traction projected on the actual fault surface do vary with local geometry in our rough-fault model. We have applied a linear slip weakening friction law in the study, and the friction parameters are spatially uniform. The S ratio defined in terms of the mean-plane tractions is uniform, and the actual S ratio varies spatially.

In all cases except SET7, the rupture is nucleated by imposing a shear traction perturbation at time $t = 0$ on a circular fault patch centered at with radius $R = 2.3\text{km}$, and of the same form as used in *Shi and Day (2013)*,

$$\Delta\tau_0(x_1, x_2) = \exp\left(\frac{r^2}{r^2 - R^2} H(R - r)\tau_0(x_1, x_2)\right), \quad (3.2)$$

where H is the Heaviside step function, $r = \sqrt{(x_1 - x_1^0)^2 + (x_2 - x_2^0)^2}$, and $\tau_0(x_1, x_2)$ is the shear traction resolved by initial stresses onto the rough fault plane. In the case of SET7, there is no initial stress perturbation, and instead an initial minimum rupture velocity of 1800 m/s is applied in a patch of radius 4 km to initiate rupture.

3.3 Supershear Rupture Styles

The rough-fault rupture simulations show a wide range of rupture behaviors. These include secondary pulses on previously ruptured areas, rupture arrest due to local geometry and supershear transitions. Generally, increasing fault roughness imposes additional drag, leading to smaller ruptured area (e.g., *Fang and Dunham*, 2013). The local geometry plays an important role in governing the rupture dynamics on a rough fault (*Yao et al.*, 2015). Generally, at a restraining bend, the rupture slows down or dies out, and, conversely, the rupture velocity tends to accelerate at a releasing bend. Slip pulses sometimes surround and bypass local surface barriers and focus in a small area that then ruptures very energetically. We also observe slip pulses triggered by re-rupturing of pre-slipped areas, due to the fault irregularity. Occasionally, we find slip pulses that temporarily die out due to fault roughness, and subsequently grow to much larger areas, sometimes accompanied by supershear rupture.

In this section, we show examples of several characteristic supershear transition mechanisms that we have identified in the simulation ensembles. We relate these to similar mechanisms already known from flat-fault simulations.

Previous work has identified several different supershear transition styles that happen in simulations of faulting on a simple plane. On a planar fault, a daughter crack is sometimes nucleated by the shear-stress peak traveling with shear wave velocity in front of the main Mode II rupture, and this mechanism is often seen in simulations done under uniform loading and friction parameters, and with sufficiently high loading (as measured by the dimensionless S ratio). The supershear transition occurs when the daughter crack merges with the main sub-

Rayleigh rupture (*Andrews, 1976; Burridge, 1973*). Supershear also happens in the presence of favorable heterogeneity, such as a small patch of higher prestress. The main rupture propagates with sub-Rayleigh speeds, a higher prestress patch causes the rupture to transition to supershear and the rupture remains supershear afterward (*Liu and Lapusta, 2008*). Supershear rupture initiation near the free surface has been documented in a number of 3D dynamic ruptures simulations (*Olsen et al., 1997; Aagaard, 2001; Day et al., 2008; Kaneko et al., 2008; Olsen et al., 2008*). *Kaneko and Lapusta (2010)* have explored the theoretical basis for this supershear transition at shallow depth, and its consequences for dynamic ruptures, in more detail. When rupture intersects the free surface, the rupture front may transition to supershear due to intersection of the stress field induced by near-surface sliding and SV-P conversion along the free surface. Another supershear mechanism happens in a barrier model when the rupture front encircles a fault-plane barrier, and then breaks it after the stress ahead of the barrier is concentrated by convergence of the encircling rupture fronts (and it is notable that this mechanism is specific to 3D models, i.e., it only operates when the fault surface is two-dimensional). When the barrier breaks, a slip pulse traveling at the P wave velocity is induced (e.g., *Dunham et al., 2003*). In the rough fault simulations, we see recognizable analogues of each of these types of supershear transition. It is also likely that many instances of supershear rupture occur through a combination of these, and similar, mechanisms.

Supershear transitions that combine elements of the favorable-heterogeneity mechanism of *Liu and Lapusta (2008)* and the Burridge-Andrew daughter-crack mechanism have been observed in our rough-fault simulations. The rough-fault cases differ in that, for the models of *Liu and Lapusta (2008)*, the favorable heterogeneity is from existing higher prestress areas or subcritical cracks, whereas in this study, the favorable heterogeneity is of geometric origin. For example, this type of transition typically occurs in association with releasing bends. Figure 3.1 (left column) shows the rupture pulse evolution on a rough fault where the presence of favorable geometry leads to a daughter-crack type supershear transition. This example is for one realization when α equals 0.005. The slip pulse expands

from the nucleation center from $t = 0$, and when the rupture front starts to fall into the rupture-favorable area near (17km, 9km) at $t = 1.8$ s, a crack is generated ahead of the rupture front. The local geometry is illustrated in the right column of Figure 3.1. After entering into rupture-favorable area, the slip pulse is enhanced and generates a transient supershear pulse, reaching to (21km, 8km) at 2.4s. This example is characteristic in the sense that supershear transients of this sort happen mainly in areas of high initial traction ratio, by which we mean the ratio of initial resolved shear traction to normal traction on the fault, analogous to releasing bends in 2D geometry.

Another pattern of supershear transition is triggering by the focusing of strong slip pulses at an otherwise unfavorable area, which is very similar to the phenomenon in (*Dunham et al.*, 2003). More typically, in our simulations, if there is unfavorable geometry, the rupture weakens or even dies out. However, exceptions occur that lead to supershear transients. In those cases, when the rupture front encounters an unfavorable geometry, such as a patch of low initial traction ratio (analogous to a restraining bend), the rupture front splits into different paths surrounding the unfavorable geometry. If the split rupture fronts are strong enough that they do not die out in along those paths, the subsequently merging pulses can trigger supershear rupture. Figure 3.2 illustrates the snapshots of rupture pulse evolution on a rough fault when such an unfavorable geometry is present. This case is a realization when α equals 0.005. The rupture pulse is very strong after initiation, and begins to split into several strong pulses after encountering the geometrical barrier at 5.2s. At 6.4s, the two rupture paths merge at a point, and the resulting stress concentration is strong enough to generate a short-lived supershear pulse.

A third pattern we have observed is the free-surface triggered supershear transition. In the set of simulations SET2, in which a free surface is present at the top edge of the fault surface (and stress levels are the same as in SET1 that is, they are not tapered with depth), a supershear rupture is observed in almost every simulation having $\alpha \leq 0.005$, while increasing roughness causes the supershear episodes to become more transient, less connected and more limited to shallow

depth. Figure 3.3 is an example, demonstrating that this supershear mechanism, common in flat-fault simulations, also operates efficiently on a rough fault. After the earthquake nucleates, the rupture pulse travels to the free surface point (42km, 0km) at 4.0s, and then a SV-P converted wave coming from the free surface causes the rupture front to accelerate to supershear speed.

The free-surface supershear event in Figure 3.3 is much larger in spatial extent than the buried-event examples in Figures 3.1 and 3.2. This contrast in size between surface and buried supershear events is a characteristic result of this study, and these two classes of events have quite distinct behaviors in other respects, as we show later. The classification is not always a sharp one, however. We have also observed cases where slip pulses due to free surface reflections interfere with the rupture at depth, leading to a buried supershear transition that then merges with a surface supershear rupture to produce a hybrid of the two types.

3.4 Analysis of Supershear Rupture

We find that fault roughness influences supershear rupture styles in a complex manner. In particular, increasing fault roughness reduces the frequency of occurrence and sustainability of supershear that is triggered along the free surface (free-surface supershear”), but enhances the occurrence of supershear on parts of the fault that are not influenced by the free-surface interaction (buried supershear). We have tested how fault roughness level affects free surface triggered supershear in SET2, and how fault roughness level changes buried supershear in SET1.

An increase of fault roughness level, α , reduces the frequency of occurrence, total area, and degree of connectivity of free-surface supershear events. When the fault is relatively smooth, those areas have wide depth extent and are relatively continuous. When fault becomes rougher, the supershear areas become smaller and more fragmented. The left column of Figure 3.4 shows the rupture velocity distribution for SET2 simulations done with one realization of the fault surface, scaled to five different levels of fault roughness. The color saturation is set such that supershear areas appear in yellow. At the highest roughness levels (α equals

0.007 and 0.009), the rupture stops before rupturing the entire surface. The supershear areas along the free surface (x coordinate 0-3 km, and 15-20 km) become progressively more fragmented as roughness increases. The behavior of this example is representative, as shown in the right-hand panel of Figure 3.4. The lower right panel of Figure 3.4 shows the probability density of rupture velocity in the depth interval from the free surface to 2km depth, at different fault roughness levels. The upper right panel shows the supershear portion in detail, and indicates that increased roughness significantly reduces the near-surface supershear area. It appears that geometric irregularities weaken the slip pulses, sometimes even causing them to die out, thereby minimizing the development of supershear pulses. Another factor is that the irregularities also reduce the coherence of the free-surface P wave conversion.

The free-surface transitions are sensitive to the shallow stress drop and frictional parameters. In SET3, friction parameters are tapered near the free surface, resulting in much smaller shallow stress drops, compared to the uniform frictional parameters in SET2. As an example, Figure 3.5 gives an example comparing the same realization of fault geometry, for the SET2 and SET3 parameter inputs. The comparison shows that tapering of the friction coefficient diminishes the near-surface supershear occurrence at all level of fault roughness. At all fault roughness levels, the supershear near free surface has been almost completely suppressed by these smaller stress drops.

In contrast to this behavior of the free surface-influenced supershear, increasing the fault roughness level enhances, rather than reduces, the buried supershear events, i.e., occurrences on parts of the fault plane remote from free surface influence. This is most easily analyzed with SET1 (which was done without a free surface). Figure 3.6 gives an example of how the rupture velocity distribution changes when the α varies with fixed fault surface shape. Analysis of all simulations in SET1 shows that supershear occurrence is enhanced when α changes over the range 0.001 to 0.005, and then is little affected by further increases in roughness.

In this example, the occurrence of supershear patches is very low in all cases,

and those that occur are highly fragmented into very small, disconnected areas. Evidently, the parameter choices for SET1 did not yield a very significant overall incidence of supershear rupture. Nonetheless, the systematic result that roughness enhances the incidence of supershear may become important for other parameter inputs. In any case, it calls for some further comment, since fault roughness can be interpreted as a secondary source of resistance to slip (roughness drag, as discussed by *Fang and Dunham* (2013), acting in addition to frictional resistance. And increasing frictional resistance (with other parameters fixed) reduces the tendency for supershear transitions to occur in flat-fault simulations, the opposite of the behavior of SET1.

Our analysis is similar to *Bruhat et al.* (2016), who explored 2D rough-fault simulations. They related supershear incidence to local slope of the (1D) fault trace. To adapt this idea to 3D, we use the initial traction ratio, which is the ratio of initial shear traction and initial normal traction, and gives guidance to how favorable the local geometry is for rupture (e.g., a higher initial traction ratio indicates a point on the fault that is at a rupture-favorable bend). Figure 3.7 illustrates how the probability density of initial traction ratio on all points at supershear regions is different from that at sub-shear regions in SET1. The supershear behaviors mainly happen at releasing bend regions, which correspond to high initial stress ratio. At all levels of α , the observation is consistent. Thus, the principal effect of roughness in SET1 is simply to make available areas of high initial stress ratio to host supershear events, and this is consistent with the fragmented, unsustainable nature of those events (compared with the well-connected, sustained shallow events that are characteristic of SET2).

We follow up on this idea by comparing results from SET1 with SET5, where the latter replaces the SET1 rough faults with planar faults, but projects the initial traction distributions from SET1 onto the flat fault. We refer to this arrangement as a pseudo-stress model. Figure 3.8 gives an example showing how the local tractions vary due to the resolution of the uniform stress field onto rough fault geometry.

Figure 3.9 shows an example comparing rupture velocity distributions for

a SET1 (left column) simulation and the corresponding SET5 (middle column) simulation. The pseudo-stress model leads to larger rupture area at the same roughness level in the same geometry, although the difference is small. The initial condition of traction is the primary influence on the rupture behaviors, though the dynamic interactions with local geometry during the rupture process leads to some small effects. The probability density of rupture velocity in all simulations in SET1, and the same quantity for SET5, are illustrated in the right column in Figure 3.9. At the same roughness level, the pseudo-stress model tends to have somehow larger rupture velocity compared to rough model, with upward shifts in median rupture velocity for the pseudo-stress model of about 0.3%, 3%, 7%, 12%, and 19% for α values of 0.001, 0.003, 0.005, 0.007, and 0.009, respectively. At relatively high α , i.e., in the range 0.005 to 0.009, the pseudo-stress model has higher probability to generate supershear. These rupture velocity differences are small, but systematic, and can be roughly understood in terms of the *Fang and Dunham* (2013) concept of roughness drag, in which slip on a rough fault removes energy otherwise available for rupture by repartitioning it into the short-wavelength strain field around the fault irregularities.

Schmedes et al. (2010) studied supershear transitions in simulations of buried faults, where the fault geometry is flat and the background shear stress is heterogeneous in the form of a 2D self-similar distribution on the fault plane. In that model, the smoother the stress field, the more likelihood supershear occurs, which is in contrast to the conclusions for the buried faults in our study. In *Schmedes et al.* (2010), the smoother models use a higher spectral exponent (in wavenumber space), whereas in our model, the models maintain the same spectral shape, and roughness is controlled by scaling the prefactor of the spectral model. As *Schmedes et al.* note, their model gives more highly correlated initial stresses as it becomes smoother, which facilitates supershear.

Another factor that plays an important role in the supershear transition is background shear stress. Increasing background shear stress from 70Mpa (SET1) to 71Mpa (SET4) in our simulations translates to a decrease of around 17% in the mean-plane S ratio. Figure 3.10 (left and middle) gives an example compar-

ing rupture velocity distributions for the two initial stress levels, with α varying (for a fixed realization of fault geometry). The right panels of Figure 3.10 show probability density of rupture velocity for the SET1 ensemble (all fault points, for all simulations) as solid lines, with comparable results for the SET4 ensemble as dashed lines. Increasing background shear stress favors supershear rupture at all levels of fault roughness.

Finally, SET6 and SET7 allow us to explore effects, on buried supershear events, that are associated with the proximity to the nucleation point and the conditions of nucleation. In SET6, the fault length is extended to 90km to allow a wide range of distances from nucleation, and also to potentially accommodate any large supershear patches that might develop. There is no free surface, so that we are examining here the potential for buried supershear transients, and their size (area) distribution, without interference from the free surface effect. We will see that the nucleation by over-stressing, following Equation 2 (the nucleation mechanism used in all cases except SET7) leads to a concentration of supershear patches near the nucleation site, so to see which distance effects are independent of nucleation artifices, we compare with SET7, in which rupture is initiated without applying a stress inhomogeneity at the hypocenter. Many simulated ruptures stop spontaneously before reaching the allowed limits of the fault surface, and we limit this part of the analysis to simulations whose rupture area is larger than 20% of that allowable area. For each simulation realization selected, we adapt the breadth first search algorithm (Zuse, 1972) to retrieve each of the connected areas where the rupture velocity is larger than shear wave velocity. We only consider connected supershear areas whose area is no smaller than $0.5km^2$.

In Figure 3.11, we plot the area of each connected supershear patch vs distance to the nucleation center. Results are shown for $\alpha = 0.005$ cases for SET1, SET6, and SET7, and we distinguish events in the nucleation regions (left), and outside of the nucleation regions (middle). In both SET1 and SET6 (which use nucleation by overstressing), there are many connected supershear patches observed in the nucleation regions in Figure 3.11 (left), while, there is only one connecting supershear patch in the nucleation region in SET7 (since the nucleation is highly

artificial, we do not attribute any physical significance to the events inside the nucleation area, and only show them to illustrate some of the differences in behavior associated with the different nucleation strategies). In SET1 and SET6, the stress perturbation strategy generates high energy release rate, which accounts for the numerous supershear patches inside, and just outside, the nucleation region. The smooth acceleration in the nucleation process in SET7 generates very few connected supershear patches in those same regions. Outside of the nucleation regions, the patterns of connecting supershear patches and distances to the nucleation center are very similar for SET6 and SET1 in areas close to the nucleation region. However, the upper limit of the connected area of the supershear patches which is 50km^2 in SET6 is higher than the 10km^2 in SET1. In SET6, the connected supershear patches appear beyond 35km distance from the nucleation center. These differences are the results of adoption of larger fault length in SET6, which enables the fault to accommodate larger ruptures, and therefore also larger supershear patches at larger distances. Extending the fault width from 15km in SET6 and SET1 to 30km in SET7 generates many more connected supershear patches, whose centroid locations range from 4km to 50km away from the the nucleation centers. The upper limit of the connected supershear patch size increases with distance up to about 20 km from the nucleation point, where it reaches around 100km^2 . The distance saturation of the upper limit can be roughly understood in terms of simple crack theory, in that the stress intensity factor of a crack initially grows with square root of rupture length, but that growth saturates at distances of the order of the narrow dimension of a high-aspect ratio fault (*Day, 1982; Andrews, 2005*). The same line of argument is qualitatively consistent with the higher incidence of supershear events in SET7 (which has higher fault width, and therefore higher stress intensity at most distances).

Figure 3.11, right panel, shows the same information as do the left and middle panels, but in a different format. The right panel compares the ratio of the area of each connected supershear patch to total ruptured area of the fault in the corresponding simulation, and with this scaling the upper limits in the three datasets are very similar, at around 5% of total rupture area.

3.5 Discussion

In our simulation datasets, there are two distinct types of supershear transitions based on the locations where supershear transitions happen. One type is induced by interference between a rupture front and surface reflected wavefront, which may be more effective when both fronts are relatively coherent and not much distorted by roughness of the surface. The other type is initiated by heterogeneity, either favorable or unfavorable bend on the fault surface.

In our simulation set SET2, supershear transitions near the free surface have been observed in every simulation up to roughness level α of 0.005 (although at α 0.005 many are sufficiently fragmented spatially as to be of questionable seismological significance). At higher roughness levels, the free surface supershear episodes become rarer, more fragmented, less sustained spatially. Thus, the presence of the free surface is clearly an important factor in the triggering of supershear, but with the added complication that free-surface triggered supershear is also sensitive to near-surface stress drop. The transition is suppressed when stress drop tapers to very low values near the free surface, as in SET3 (compare Figure 3.4 with Figure 3.5). The 2001 M7.8 Kunlun earthquake produced a 350-km-long surface rupture at supershear speed (*Bouchon and Vallée, 2003; Robinson et al., 2006; Vallée et al., 2008; Walker and Shearer, 2009; Wen et al., 2009*). The 2002 Denali Fault earthquake ruptured the earths surface over about 340km, with unknown length of supershear surface rupture based on the observation that the rupture passed the near-fault station at supershear speed (*Aagaard and Heaton, 2004; Dunham et al., 2004; Ellsworth et al., 2004*). Both of these earthquakes have characteristics consistent with our free surface type supershear, in that the supershear segments are present at the surface, and they are sustained over long enough distances to have observable seismic signatures once they are triggered. They are also associated with relatively smooth fault traces (*Bouchon et al., 2010*). That is, our free-surface type supershear transitions have behavior consistent with the inference from field observations (*Bouchon et al., 2010*), that smoother or geometrically simple fault segments are more likely to host supershear propagation.

Buried supershear shows different behaviors compared with free surface type

supershear. In major datasets of our study, the buried supershear transitions are more transient, with smaller connected supershear areas compared to free surface type supershear at the same level of fault roughness level, suggesting that buried supershear transitions would be more difficult to observe. Only 20% of simulated events have buried supershear episodes exceeding $2km^2$ in area, which is probably already far below the lower limit of resolvability for finite fault inversions. A few exceed $50km^2$, however (Figure 3.11). A buried supershear transient of that order of magnitude in size has been inferred for the 1979 Imperial Valley earthquake, on the basis of strong motion accelerograms (e.g., *Archuleta, 1984; Spudich and Frazer, 1984*). This may be a natural analogue of our buried supershear episodes triggered by fault irregularity.

Our study shows fault roughness favors buried supershear transitions, which agrees with 2D supershear analysis on rough faults (Bruhat et al., 2016). While 3D simulations confirm this feature of the 2D simulations, the 3D simulations reveal the contrasting behavior of supershear transitions induced by free-surface interactions, which are favored by geometrically simple faults, and suppressed by geometrical complexity. Thus, the 3D results provide one means to reconcile the result from 2D simulations that supershear transitions are favor by roughness with the inference from field observations (*Bouchon et al., 2010*) that supershear is favored by smoothness of the fault trace. The latter observation may also be explained in part by the observation by Bruhat et al. (2016) that, while roughness favors supershear triggering, smooth fault segments favor large supershear rupture areas.

Using pseudo-stress model as an approximation of the rough model overestimates the possibility of supershear transitions when α is at relatively high level in the range from 0.005 to 0.009. The pseudo-stress model tends to generate higher probability of supershear when α falls into that range. At all fault roughness levels, the pseudo-stress model tends to have somehow larger rupture velocity compared to that in rough model. These systematic differences are small, but can be understood as roughness drag (Fang and Dunham, 2013). When the roughness level α is low, pseudo-stress model is a good approximation to rough model.

One limitation of the study is the simplification of the slip weakening friction law. This simplicity can help us understand the complex rupture process on irregular fault surface. However, strongly dynamic rate weakening during rupture process has been observed in high-speed friction experiments (e.g., *Tsutsumi and Shimamoto, 1997; Di Toro et al., 2004; Hirose and Shimamoto, 2005; Han et al., 2010; Goldsby and Tullis, 2011; Brown and Fialko, 2012*). The rate and state friction law with strong dynamic weakening can support self-sustaining slip pulses both on planar and nonplanar faults (*Dunham et al., 2011a,b; Gabriel et al., 2013; Shi and Day, 2013*). The use of rate and state friction law can provide more types of rupture and perhaps more realistic rupture process. In slip weakening friction law, high stress drop is expected to nucleate a earthquake on rough fault, generally generating crack-like pulses. However, low stress drop could host rupture propagation on rough faults using rate and state friction law (*Dunham et al., 2011b*), and could generating self-healing pulse. In a few preliminary explorations, adopting dynamic weakening in a rate and state friction law does not seem to affect the main qualitative results of this study. That is, while the alternative friction law can give different rupture velocity distributions on faults, compared to slip weakening law, given the same bulk properties and fault roughness properties, the factors which contributes to supershear transitions are the same, such as degree of roughness, background shear stress, tapered shallow friction parameters and existence of free surface. A more complete study would be required to support any quantitative conclusions and to assess the degree to which frequency of occurrence of supershear transitions is sensitive to choice of friction law.

We adopt simple homogeneous stress distribution on fault plane without considering the volumetric stress fields generated around the fault after many earthquake cycles, which is clearly not a realistic assumption. Another important factor which should be considered is off fault plasticity. Off fault deformation which is expressed in the form of minor secondary faulting, microcracking and rigid-block rotation etc, can vary from 0 to 100% of surface deformation along coseismic ruptures, as measured from numerous strike-slip faults based on surface deformation observations (e.g., *Nelson and Jones, 1987; Miller and Yount, 2002;*

Rockwell et al., 2002; Treiman et al., 2002; Kimurah et al., 2004; Shelef and Oskin, 2010; Van Dissen et al., 2011; Quigley et al., 2012; Milliner et al., 2015). Incorporating plasticity typically reduces rupture velocity (e.g., *Andrews, 2005; Duan and Day, 2004*) and may be expected to reduce the probability of supershear transitions by releasing strain energy as off fault deformations. These effects could be addressed in future simulation-based studies.

3.6 Conclusions

Dynamic rupture simulations on 3D self-similar rough faults show supershear transitions having mechanisms that are similar to those that have been identified in flat-fault simulations. The dependence of the transitions of fault roughness is different for two classes that appear in the simulations. The first class, buried supershear episodes not influenced by free surface interaction, are favored by rougher faults, a result already seen in 2D simulations (*Bruhat et al., 2016*). Most such buried events are probably too small to have seismological significance, but a few in our simulation ensembles have rupture areas approaching 100km^2 (5% of the total ruptured area of the fault). The second class, supershear episodes induced by free surface interactions, are favored by smoother faults, and tend to be relatively large in area. The latter result is consistent with field observations (*Bouchon et al., 2010*) that have associated large supershear episodes with the presence of relatively simple fault traces. Increasing background shear stress level enhances supershear events of all types, and free-surface induced supershear transitions are especially sensitive to shallow stress drop. The size distribution of buried supershear events, and their distribution with respect to hypocentral distance, are both influenced by the rupture initiation method in the simulations, as well as by the overall rupture dimensions.

We introduce a so-called pseudo-stress model to assess the extent to which the kinematics associated with a rough fault can be mimicked by a flat fault loaded with the same initial traction distribution. Statistically, the rupture in pseudo-stress model predicts higher rupture velocity, larger rupture area and higher prob-

ability of supershear transition than rough model. The median rupture velocity at pseudo-stress model increases 0.3%, 3%, 7%, 12% to 19% comparing to rough model when α increases in equal steps from 0.001 to 0.009. These differences can be qualitatively understood by viewing the dynamics of the rough model as a result of modifying the pseudo-stress model with the addition of roughness drag.

3.7 Acknowledgements

This work was supported by NSF award EAR-1135455. Simulations were done using the generalized finite difference code SORD at Blue Waters supercomputer at the National Center for Supercomputing Applications. Input files to reproduce the simulation results are available upon request.

Chapter 3, in full, is a reformatted version of a paper currently being prepared for submission for publication to Journal of Geophysical Research: Yao, Q. and S. M. Day, Supershear Transition Analysis in 3D Rough Fault Dynamic Simulations. (2017). I was the primary investigator and author of this paper.

References

- Aagaard, B.T., Heaton, T.H., Hall, J.F. (2001). Dynamic earthquake ruptures in the presence of lithostatic normal stresses: implications for friction models and heat production. *Bull. Seismol. Soc. Am.* 91(6) 11,765-11,796.
- Aagaard, B. T. and T. H. Heaton (2004). Near-source ground motions from simulations of sustained intersonic and supersonic fault ruptures. *Bull. Seismol. Soc. Am.* 94, 2064-2078.
- Andrews, D. J. (1976), Rupture velocity of plane strain shear cracks, *J. Geophys. Res.*, 81(32), 5679-5687, doi:10.1029/JB081i032p05679.
- Andrews, D. J. (1985), Dynamic plane-strain shear rupture with a slip-weakening friction law calculated by a boundary integral method, *Bull. Seismol. Soc. Am.*, 75(1), 1-21.
- Andrews, D. J. (2005). Rupture dynamics with energy loss outside the slip zone. *J. of Geophys. Res.*, 110(B1), 307.

- Andrews, D. J., and M. Barall (2011). Specifying initial stress for dynamic heterogeneous earthquake source models, *Bull. Seismol. Soc. Am*, *101*, 2408-2417
- Archuleta, R. J. (1984), A faulting model for the 1979 Imperial Valley earthquake, *J. Geophys. Res.*, *89*(B6), 4559-4585, doi:10.1029/JB089iB06p04559.
- Bouchon, M., and M. Vallée (2003), Observation of long supershear rupture during the magnitude 8.1 Kunlunshan earthquake, *Science*, *301*(5634), 824-826, doi:10.1126/science.1086832.
- Bouchon, M., N. Toksz, H. Karabulut, M. P. Bouin, M. Dietrich, M. Aktar, and M. Edie (2000), Seismic imaging of the 1999 Izmit (Turkey) rupture inferred from the near-fault recordings, *Geophys. Res. Lett.*, *27*(18), 3013-3016, doi:10.1029/2000GL011761.
- Bouchon, M., M. P. Bouin, H. Karabulut, M. Nafi Toksz, M. Dietrich, and A. J. Rosakis (2001), How fast is rupture during an earthquake? New insights from the 1999 Turkey earthquakes, *Geophys. Res. Lett.*, *28*(14), 2723-2726, doi:10.1029/2001GL013112.
- Bouchon, M., H. Karabulut, M. P. Bouin, J. Schmittbuhl, M. Valle, R. Archuleta, S. Das, F. Renard, and D. Marsan (2010), Faulting characteristics of supershear earthquakes, *Tectonophysics*, *493*(3-4), 244-253, doi:10.1016/j.tecto.2010.06.011.
- Brodsky, E. E., J. J. Gilchrist, A. Sagy, and C. Collettini (2011), Faults smooth gradually as a function of slip, *Earth Planet. Sci. Lett.*, *302*(1-2), 185-193, doi:10.1016/j.epsl.2010.12.010.
- Brown K, Fialko Y (2012) 'Melt welt' mechanism of extreme weakening of gabbro at seismic slip rates. *Nature.*, *488*(7413):638-41. PMID: 22932388.
- Bruhat, L., Z. Fang, and E. M. Dunham(2016), Rupture complexity and the supershear transition on rough faults, *J. Geophys. Res. Solid Earth*, *121*, doi:10.1002/2015JB012512.
- Burridge, R. (1973), Admissible speeds for plane-strain self-similar shear cracks with friction but lacking cohesion, *Geophys. J. R. Astron. Soc.*, *35*(4), 439-455, doi:10.1111/j.1365-246X.1973.tb00608.x.
- Candela, T., F. Renard, M. Bouchon, A. Brouste, D. Marsan, J. Schmittbuhl, and C. Voisin (2009), Characterization of fault roughness at various scales: Implications of three-dimensional high resolution topography measurements, *Pure Appl. Geophys.*, *166*(10-11), 1817-1851, doi:10.1007/s00024-009-0521-2.
- Candela, T., F. Renard, Y. Klinger, K. Mair, J. Schmittbuhl, and E. E. Brodsky (2012), Roughness of fault surfaces over nine decades of length scales, *J. Geophys. Res.*, *117*, B08409, doi:10.1029/2011JB009041.

- Chester, F. M., and J. S. Chester (2000), Stress and deformation along wavy frictional faults, *J. Geophys. Res.*, *105*(B10), 23,421-23,430, doi:10.1029/2000JB900241.
- Crempien, J. G. F., and R. Archuleta (2015), UCSB method for simulation of broadband ground motion from kinematic earthquake sources, *Seismol. Res. Lett.*, *86*(1), 61-67, doi:10.1785/0220140103.
- Day, S. M. (1982). Three-dimensional simulation of spontaneous rupture: the effect of nonuniform prestress. *Bull. Seismol. Soc. Am.*, *72*, 1881-1902.
- Day, S. M., L. A. Dalguer, N. Lapusta, and Y. Liu (2005), Comparison of finite difference and boundary integral solutions to three-dimensional spontaneous rupture, *J. Geophys. Res.*, *110*(B12), 1-23, doi:10.1029/2005JB003813.
- Day, S.M., Gonzalez, S.H., Anooshehpour, R., Brune, J.N., 2008. Scale-model and numerical simulations of near-fault seismic directivity. *Bull. Seismol. Soc. Am.* *98*, 1186-1206.
- Di Toro, G., D. L. Goldsby, and T. E. Tullis (2004), Friction falls toward zero in quartz rock as slip velocity approaches seismic rates, *Nature*, *427*, 436-439, doi:10.1038/nature02249.
- Duan, B., and S. M. Day (2008), Inelastic strain distribution and seismic radiation from rupture of a fault kink. *J. Geophys. Res.*, *113*(B12), 119. doi:10.1029/2008JB005847.
- Dunham, E. M. and R. J. Archuleta (2004), Near-source ground motion from steady state dynamic rupture pulses, *Geophysical Research Letters*, *32*, L03302, doi:10.1029/2004GL021793.
- Dunham, E. M. (2007), Conditions governing the occurrence of supershear ruptures under slip-weakening friction, *J. Geophys. Res.*, *112*, B07302, doi:10.1029/2006JB004717.
- Dunham, E. M., P. Favreau, and J. M. Carlson (2003), A supershear transition mechanism for cracks, *Science*, *299*(5612), 1557-1559.
- Dunham, E. M., and R. J. Archuleta (2004), Evidence for a supershear transient during the 2002 Denali fault earthquake, *Bull. Seismol. Soc. Am.*, *94*(6B), S256-S268, doi:10.1785/0120040616.
- Dunham, E. M., D. Belanger, L. Cong, and J. E. Kozdon (2011a), Earthquake ruptures with strongly rate-weakening friction and off-fault plasticity, Part 1: Planar faults, *Bull. Seismol. Soc. Am.*, *101*(5), 2296-2307, doi:10.1785/0120100075.

- Dunham, E. M., D. Belanger, L. Cong, and J. E. Kozdon (2011b), Earthquake ruptures with strongly rate-weakening friction and off-fault plasticity, Part 2: Nonplanar faults, *Bull. Seismol. Soc. Am.*, *101*(5), 2308-2322, doi:10.1785/0120100076.
- Ellsworth, W. L., M. Celebi, J. R. Evans, E. G. Jensen, R. Kayen, M. C. Metz, D. J. Nyman, J. W. Roddick, P. Spudich, C. D. Stephens (2004). Near-field ground motion of the 2002 Denali Fault, Alaska, earthquake recorded at Pum Station 10. *Earthquake Spectra* *20*, 597-615
- Ely, G. P., S. M. Day, and J.-B. H. Minster (2008). A support-operator method for visco-elastic wave modeling in 3-D heterogeneous media. *Geophysical Journal International*, *172*, 331-344.
- Ely, G. P., S. M. Day, and J.-B. H. Minster (2009). A support-operator method for 3-D rupture dynamics. *Geophysical Journal International*, *177*, 1140-1150.
- Ely, G. P., S. M. Day, and J.-B. H. Minster (2010), Dynamic rupture models for the southern San Andreas Fault, *Bull. Seismol. Soc. Am.*, *100*(1), 131-150, doi:10.1785/0120090187.
- Fang, Z., and E. M. Dunham (2013), Additional shear resistance from fault roughness and stress levels on geometrically complex faults, *J. Geophys. Res. Solid Earth*, *118*, 3642-3654, doi:10.1002/jgrb.50262.
- Freund L. B. (1979). The mechanics of dynamic shear crack propagation, *J. geophys. Res.*, *84*, 2199-2209.
- Gabriel, A. A., Ampuero, J. P., Dalguer, L. A., Mai, P. M. (2013). Source properties of dynamic rupture pulses with offfault plasticity. *Journal Geophysical Research*, *118*,4117-4126. doi:10.1002/jgrb.50213.
- Goldsby, D. L., and T. E. Tullis (2011), Flash heating leads to low frictional strength of crustal rocks at earthquake slip rates, *Science*, *334*, 216-218, doi:10.1029/1126/science.1207902.
- Graves, R. W., Pitarka, A. (2010). Broadband ground-motion simulation using a hybrid approach. *Bull. Seismol. Soc. Am.*, *100*(5A), 2095-2123.
- Guatteri, M., P. M. Mai, and G. Beroza (2004). A pseudo-dynamic approximation to dynamic rupture models for strong ground motion prediction, *Bull. Seismol. Soc. Am.*, *94*, no. 6, 2051-2063, doi: 10.1785/ 0120040037.
- Guatteri, M., P. M. Mai, G. C. Beroza, and J. Boatwright (2003). Strong ground-motion prediction from stochastic-dynamic source models, *Bull. Seismol. Soc. Am.*, *93*, no. 1, 301-313, doi: 10.1785/0120020006.

- Kaneko, Y., Lapusta, N., Ampuero, J.-P., 2008. Spectral element modeling of spontaneous earthquake rupture on rate and state faults: effect of velocity-strengthening friction at shallow depths. *J. Geophys. Res.* *113*.
- Kaneko, Y., and N. Lapusta (2010), Supershear transition due to a free surface in 3-D simulations of spontaneous dynamic rupture on vertical strike-slip faults, *Tectonophysics*, *493*(3-4), 272-284, doi:10.1016/j.tecto.2010.06.015.
- Han, R., T. Hirose, and T. Shimamoto (2010), Strong velocity weakening and powder lubrication of simulated carbonate faults at seismic slip rate, *J. Geophys. Res.*, *115*, B03412, doi:10.1029/2008JB006136.
- Herrero, A. and P. Bernard (1994). A kinematic self-similar rupture process for earthquake, *Bull. seism. Soc. Am.*, *84*, 1216-1228.
- Hirose, T., and T. Shimamoto (2005), Growth of molten zone as a mechanism of slip weakening of simulated faults in gabbro during frictional melting, *J. Geophys. Res.*, *110*, B05202, doi:10.1029/2004JB003207.
- Kimurah, H., Y. Itoh, and H. Tsutsumi (2004), Quaternary strike-slip crustal deformation around an active fault based on paleomagnetic analysis: A case study of the Enako fault in central Japan, *Earth Planet. Sci. Lett.*, *226*, 321-334, doi:10.1016/j.epsl.2004.08.003.
- Liu, Y., and N. Lapusta (2008), Transition of mode II cracks from sub-Rayleigh to intersonic speeds in the presence of favorable heterogeneity, *J. Mech. Phys. Solids*, *56*(1), 25-50, doi:10.1016/j.jmps.2007.06.005.
- Ma, S. (2008). A physical model for widespread near-surface and fault zone damage induced by earthquakes. *Geochemistry Geophysics Geosystems*, *9*(11), 009.
- Mai, P. M., and G. C. Beroza (2002). A spatial random-field model for complex earthquake slip, *J. Geophys. Res.*, *107*(B11), 2308, doi:10.1029/2001JB000588.
- Mello, M., Bhat, H. S., Rosakis, A. J., and Kanamori, H. (2014). Reproducing the supershear portion of the 2002 Denali earthquake rupture in laboratory. *Earth and Planetary Science Letters*, *387*, 89-96.
- Mena, B., L. A. Dalguer, and P. M. Mai (2012), Pseudodynamic source characterization for strike-slip faulting including stress heterogeneity and super-shear ruptures, *Bull. Seismol. Soc. Am.*, *102*(4), 1654-1680, doi:10.1785/0120110111.
- Miller, D. M., and J. C. Yount (2002), Late Cenozoic tectonic evolution of the north-central Mojave Desert inferred from fault history and physiographic evolution of the Fort Irwin area, California, *Mem. Geol. Soc. Am.*, *195*, 173-197

- Milliner, C., J. Dolan, J. Hollingsworth, S. Leprince, F. Ayoub, and C. Sammis (2015), Quantifying near-field and off-fault deformation patterns of the 1992 Mw 7.3 Landers earthquake, *Geochemistry, Geophysics, Geosystems*, *16*(5), 1577-1598.
- Nelson, M. R., and C. H. Jones (1987), Paleomagnetism and crustal rotations along a shear zone, Las Vegas Range, southern Nevada, *Tectonics*, *6*, 13-33, doi:10.1029/TC006i001p00013.
- Oglesby, D. D., and S. M. Day (2002). Stochastic fault stress: Implications for fault dynamics and ground motion, *Bull. Seismol. Soc. Am.*, *92*, no. 8, 3006-3021, doi:10.1785/0120010249.
- Olsen, K.B., Madariaga, R., Archuleta, R.J. (1997). Three-dimensional dynamic simulation of the 1992 Landers earthquake. *Science*, *278*, 834-838.
- Olsen, K.B., Minster, J.B., Cui, Y., Chourasia, A., Okaya, D., Maechling, P., Jordan, T. (2008). TeraShake2: spontaneous rupture simulations of Mw 7.7 earthquakes on the southern San Andreas fault. *Bull. Seismol. Soc. Am.*, *98* (3), 1162-1185.
- Power, W. L., and T. E. Tullis (1991), Euclidean and fractal models for the description of rock surface roughness, *J. Geophys. Res.*, *96*(B1), 415-424, doi:10.1029/90JB02107.
- Power, W. L., T. E. Tullis, and J. D. Weeks (1988), Roughness and wear during brittle faulting, *J. Geophys. Res.*, *93*(B12), 15,268-15,278, doi:10.1029/JB093iB12p15268.
- Quigley, M., R. Van Dissen, N. Litchfield, P. Villamor, B. Duffy, D. Barrell, K. Furlong, T. Stahl, E. Bilderback, and D. Noble (2012), Surface rupture during the 2010 M(w) 7.1 Darfield (Canterbury) earthquake: Implications for fault rupture dynamics and seismic-hazard analysis, *Geology*, *40*, 55-58.
- Robinson, D. P., C. Brough, and S. Das (2006), The Mw 7.8, 2001 Kunlunshan earthquake: Extreme rupture speed variability and effect of fault geometry, *J. Geophys. Res.*, *111*, B08303, doi:10.1029/2005JB004137.
- Rockwell, T. K., S. Lindvall, T. Dawson, R. Langridge, W. R. Lettis, and Y. Klinger (2002), Lateral offsets on surveyed cultural features resulting from the 1999 Izmit and Duzce Earthquakes, Turkey, *Bull. Seismol. Soc. Am.*, *92*, 79-94, doi:10.1785/0120000809.
- Roten, D., K.B. Olsen, S.M. Day, and Y. Cui (2016). Quantification of fault zone plasticity effects with spontaneous rupture simulations, *Pure and Applied Geophysics*, Special issue on Best Practices in Physics-based Fault Rupture Models

- for Seismic Hazard Assessment of Nuclear Installations, doi:10.1007/s00024-017-1466-5, p. 1-23.
- Sagy, A., and E. E. Brosky (2009), Geometric and rheological asperities in an exposed fault zone. *J. Geophysics. Res.*, *114*. B02301, doi:10.1029/2008JB005701.
- Schmedes, J., R. J. Archuleta, and D. Lavalle (2010). Dependency of supershear transition and ground motion on the autocorrelation of initial stress, *Tectonophysics*, *493*, 222-235, doi:10.1016/j.tecto.2010.05.013
- Shelef, E., and M. Oskin (2010), Deformation processes adjacent to active faults: Examples from eastern California, *J. Geophys. Res.*, *115*, B05308, doi:10.1029/2009JB006289.
- Shi, Z., and S. M. Day (2013), Rupture dynamics and ground motion from 3-D rough-fault simulations, *J. Geophys. Res. Solid Earth*, *118*, 1122-1141, doi:10.1002/jgrb.50094.
- Song, S. G., A. Pitarka, and P. Somerville (2009). Exploring spatial coherence between earthquake source parameters, *Bull. Seismol. Soc. Am.*, *99*, no. 4, 2564-2571, doi: 10.1785/0120080197.
- Spudich, P., and L. Frazer (1984), Use of ray theory to calculate high-frequency radiation from earthquake sources having spatially variable rupture velocity and stress drop, *Bull. Seismol. Soc. Am.*, *74*(6), 2061-2082.
- Tsutsumi, A., and T. Shimamoto (1997), High-velocity frictional properties of gabbro, *Geophys. Res. Lett.*, *24*(6), 699-702.
- Treiman, J. A., K. J. Kendrick, W. A. Bryant, T. K. Rockwell and S. F. McGill (2002), Primary surface rupture associated with the Mw 7.1 16 October 1999 Hector Mine earthquake, San Bernardino County, California, *Bull. Seismol. Soc. Am.*, *92*, 1171-1191, doi:10.1785/0120000923.
- Vallée, M., M. Lands, N. M. Shapiro, and Y. Klinger (2008), The 14 November 2001 Kokoxili (Tibet) earthquake: High-frequency seismic radiation originating from the transitions between sub-Rayleigh and supershear rupture velocity regimes, *J. Geophys. Res.*, *113*, B07305, doi:10.1029/2007JB005520
- Van Dissen, R., et al. (2011), Surface rupture displacement on the Greendale Fault during the M (sub w) 7.1 Darfield (Canterbury) earthquake, New Zealand, and its impact on man-made structures, in *Proceedings Ninth Pacific Conference on Earthquake Engineering, Building an Earthquake-Resilient Society*, Pap. 186, 8 pp., N. Z. Soc. for Earthquake Eng., Auckland

- Walker, K.T., P. M. Shearer (2009). Illuminating the near-sonic rupture velocities of the intracontinental Kokoxili Mw 7.8 and Denali Fault Mw 7.9 strike-slip earthquakes with global P-wave back projection imaging. *J. Geophys. Res.*, 114, B02304. doi:10.1029/2008JB005738.
- Wen, Y. Y., K. F. Ma, T. R. A. Song, W. D. Mooney (2009). Validation of the rupture properties of the 2001 Kunlun, China (Ms= 8.1), earthquake from seismological and geological observations. *Geophys. J. Int.*, 177, 555-570.
- W. L., and T. E. Tullis (1995), A review of the fractal character of natural fault surfaces with implications for friction and the evolution of fault zones, in *Fractals in the Earth Sciences*, pp. 89-105, Springer, New York.
- Xia, K., Rosakis, A.J. and Kanamori, H., Laboratory Earthquakes: The Sub-Rayleigh-to-Supershear Rupture Transition, *Science*, 303, Issue 5665, 1859-1861, 2004
- Yao. Q., S. M. Day and Z. Shi, Earthquake source-parameter relationships from 3D rough fault dynamic ruptures, Abstract S43E-08 presented at 2015 Fall Meeting, AGU, San Francisco, Calif, 14-18, Dec.
- Yue, H., T. Lay, J. T. Freymueller, K. Ding, L. Rivera, N. A. Ruppert, and K. D. Koper (2013), Supershear rupture of the 5 January 2013 Craig, Alaska (Mw7.5) earthquake, *J. Geophys. Res. Solid Earth*, 118, 5903-5919, doi:10.1002/2013JB010594.
- Zuse, Konrad (1972), *Der Plankalkl* (in German), Konrad Zuse Internet Archive. See pp. 96-105 of the linked pdf file (internal numbering 2.47-2.56)

Table 3.1: Model Parameters

Parameter	Value
P Wave Velocity (km/s)	6000
S Wave Velocity (km/s)	3464
Density (kg/m^3)	2670
Dynamic Friction Coefficient	0.525
Static Friction Coefficient	0.75
Slip Weakening Distance(m)	0.4
Normal Stress (MPa)	70
Shear Strss (MPa)	120
Nucleation Width (m)	2300
Time Step Size (s)	0.002
Gird Size (m)	25
Number of Fault Surface Seeds	20

Table 3.2: Different Sets of Simulation Ensembles

Simulation Ensemble	Free Surface	Background Shear Stress (MPa)	Possible Nucleation Centers	Fault Roughness Level (α)	Simulation Size Length(km) * Width(km)
SET1	No	70	4	0.001-0.009	30*15
SET2	Yes	70	1	0.001-0.009	30*15
SET3	Yes, tapered dynamic friction coefficient	70	1	0.001-0.009	30*15
SET4	No	71	1	0.001-0.009	30*15
SET5	No	70 (projected traction as stress on planar fault)	1	0.001-0.009	30*15
SET6	No	70	1	0.005	90*15
SET7	No	70	4	0.005	60*30

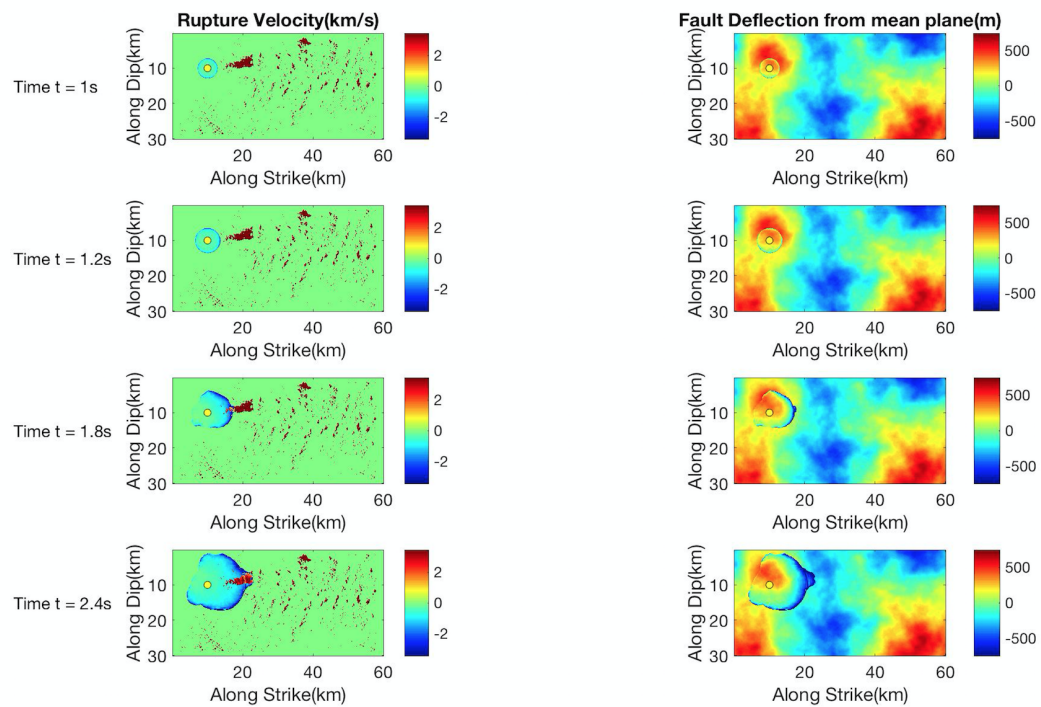


Figure 3.1: Snapshots of slip pulse evolution on rough fault with presence of favorable geometry, generating daughter crack like supershear. The yellow dot at (10km, 10km) at each figure is the hypocenter. (Left) Slip rate distribution superimposed on rupture velocity distribution. All red parts are supershear areas. The blue pulses are slip rate pulses. (Right) Slip rate distribution superimposed on fault geometry.

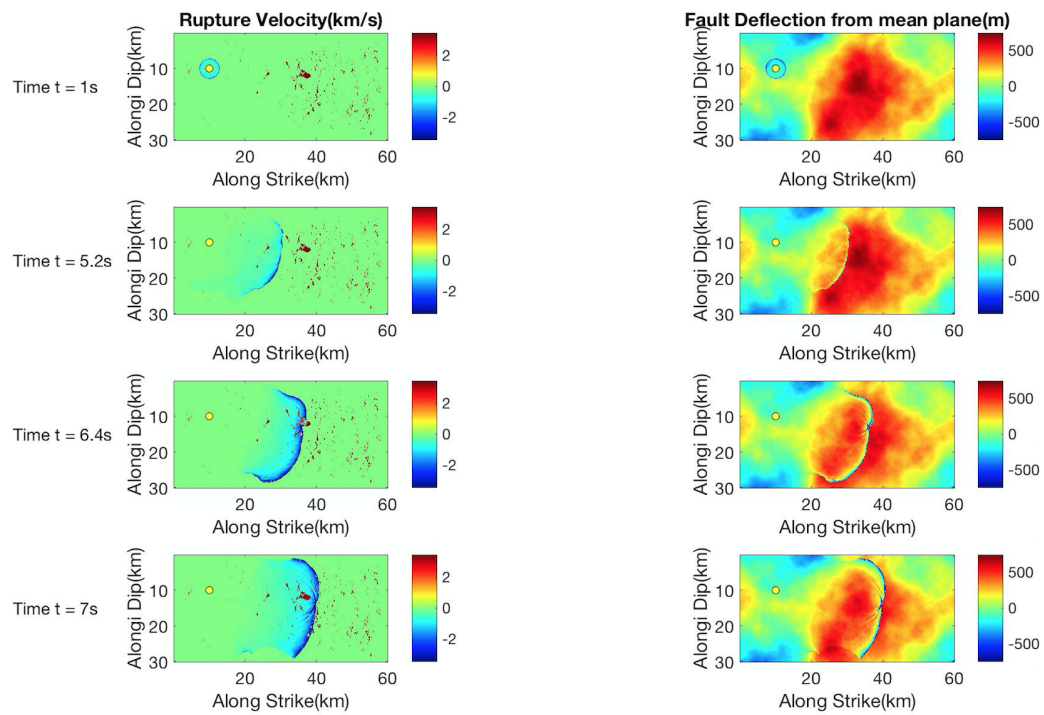


Figure 3.2: Snapshots of slip pulse evolution on rough fault with pulse-focusing effect like supershear. The yellow dot at (10km, 10km) at each figure is the hypocenter. Same as above.

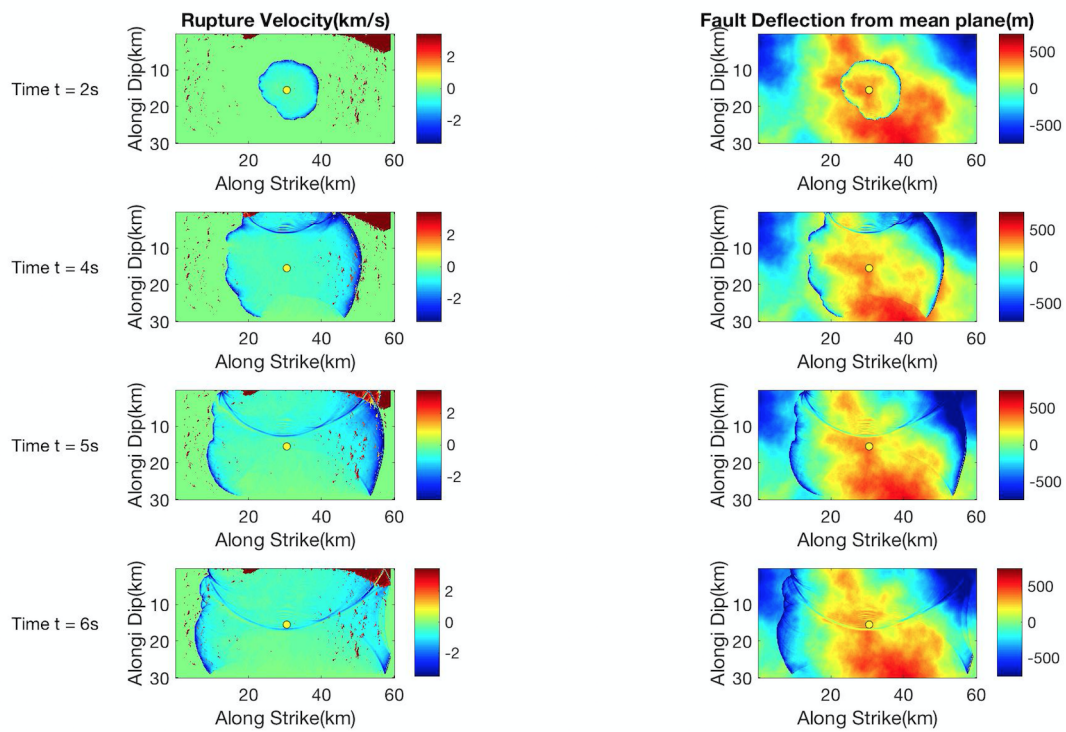


Figure 3.3: Snapshots of slip pulse evolution on rough fault with free surface triggered supershear. The yellow dot at (30km, 15km) at each figure is the hypocenter. Same as above.

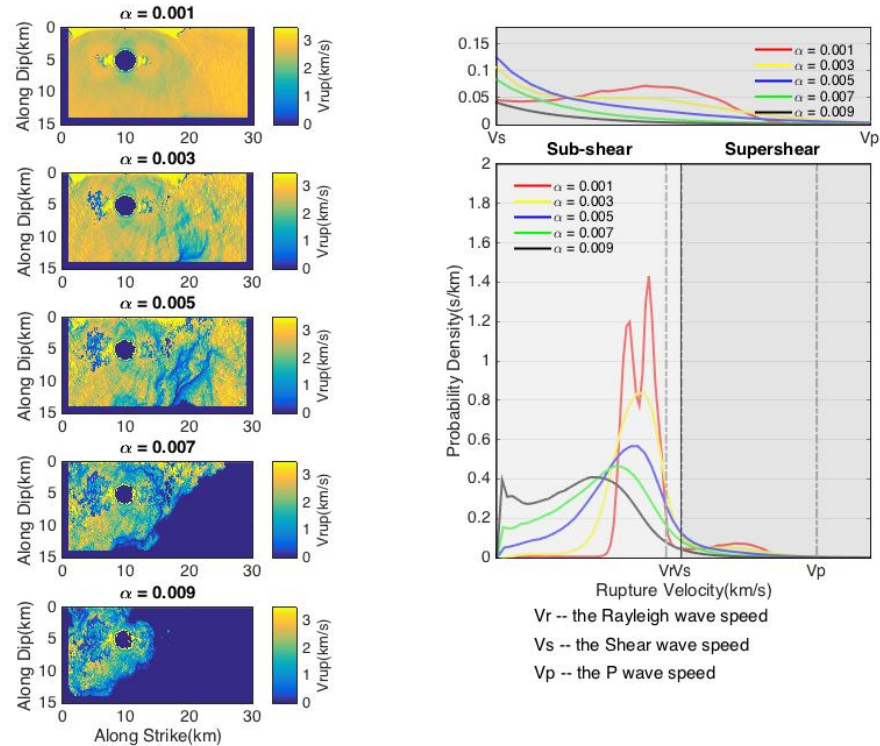


Figure 3.4: Fault roughness reduces supershear at the free surface in SET2. (Left) Comparison of rupture velocity distribution on the fault at different levels of fault roughness in one realization. From top to bottom, α is from 0.001 to 0.009. (Right) Bottom is probability density of rupture velocity at all points free surface to 2km depth at different levels of fault roughness. Top is the zoom in session of bottom at supershear regions

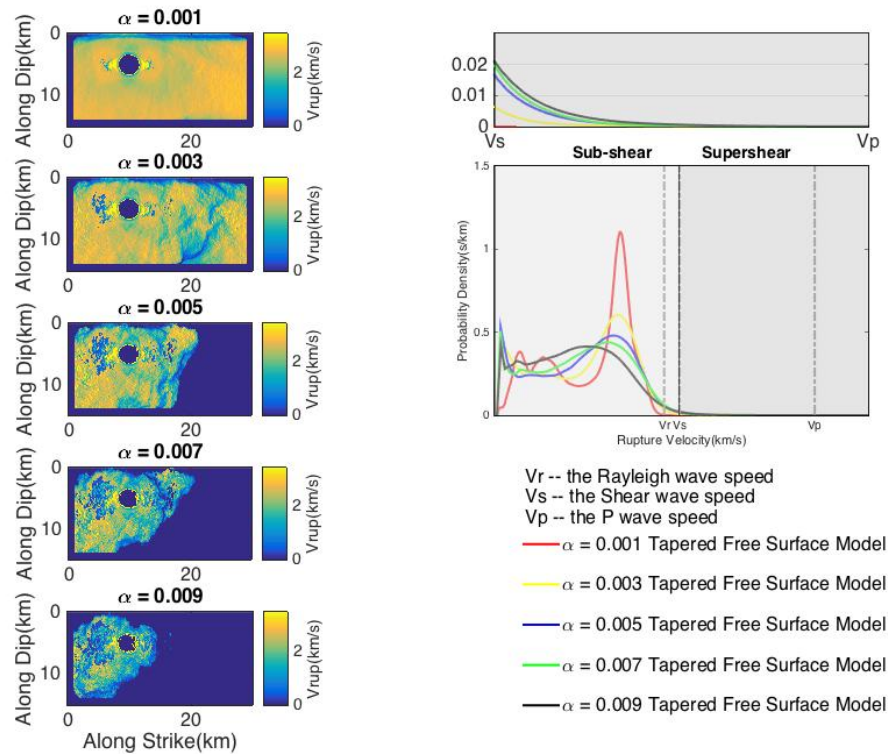


Figure 3.5: (Left) Rupture velocity distribution on the fault at all levels of fault roughness level in one realization in SET3, and α is from 0.001 to 0.009. The friction coefficients near free surface are tapering. (Right) Probability densities of rupture velocity in all simulations in SET3.

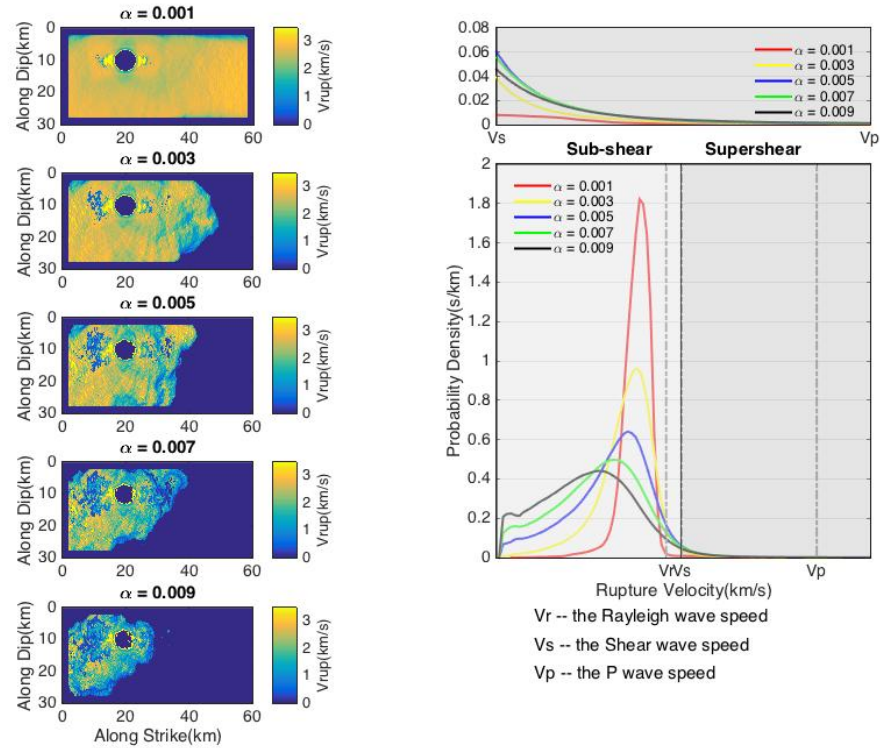


Figure 3.6: Fault roughness enhances supershear on the fault plane in SET1. (Left) Comparison of rupture velocity distribution on the fault on different levels of fault roughness in one realization. From top to bottom, α is from 0.001 to 0.009. (Right) Bottom is probability density of rupture velocity at all points on fault plane at different levels of fault roughness. Top is the zoomed out session of bottom at supershear regions.

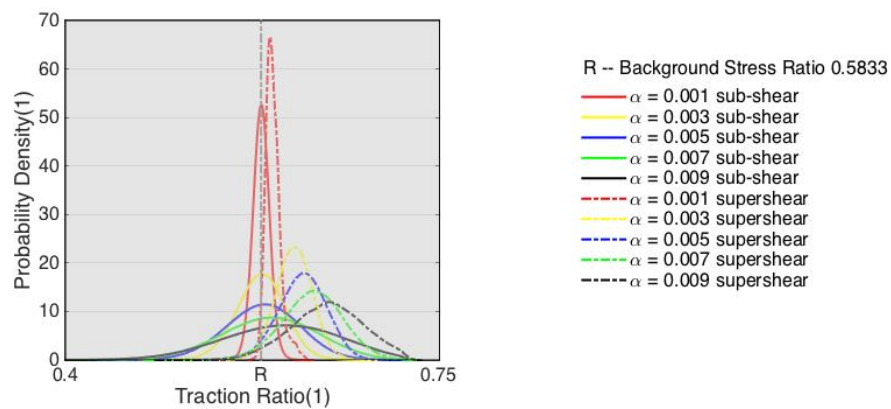


Figure 3.7: Probability density of local traction ratio for supershear points vs. subshear points for α from 0.001 to 0.009. The solid lines are for points in sub-shear regions, and the dashed lines are for points in supershear regions. R is the background stress ratio which is the ratio of background shear stress and background normal stress, which is 0.5833.

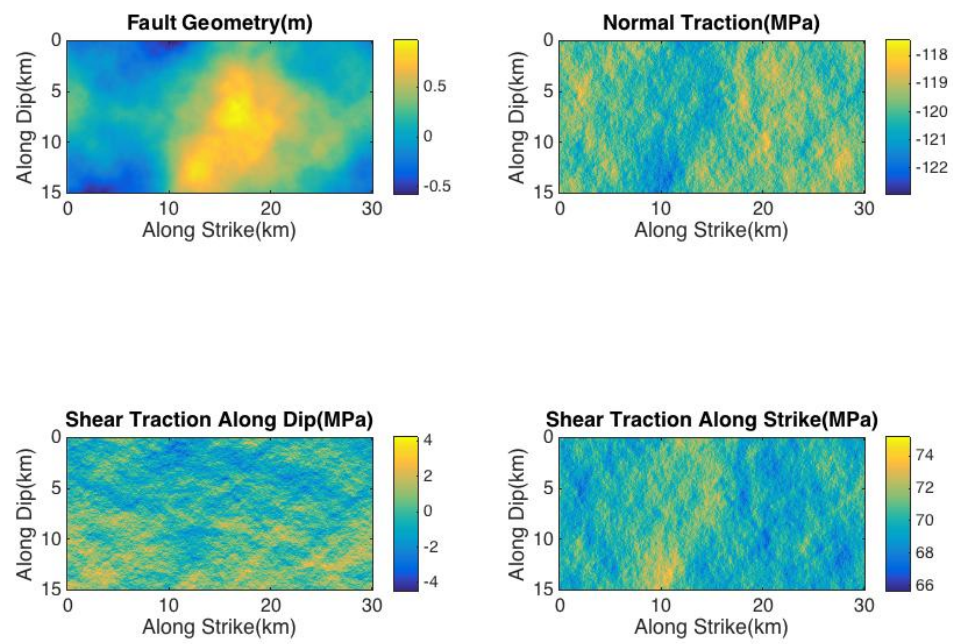


Figure 3.8: Pseudo-stress Model. (Top) left shows the fault geometry in one simulation in SET1. Right is distribution of normal traction projected on the fault plane from background stress. (Bottom) left is distribution of shear traction along dip direction as before, right is the distribution of shear traction along strike direction as before.

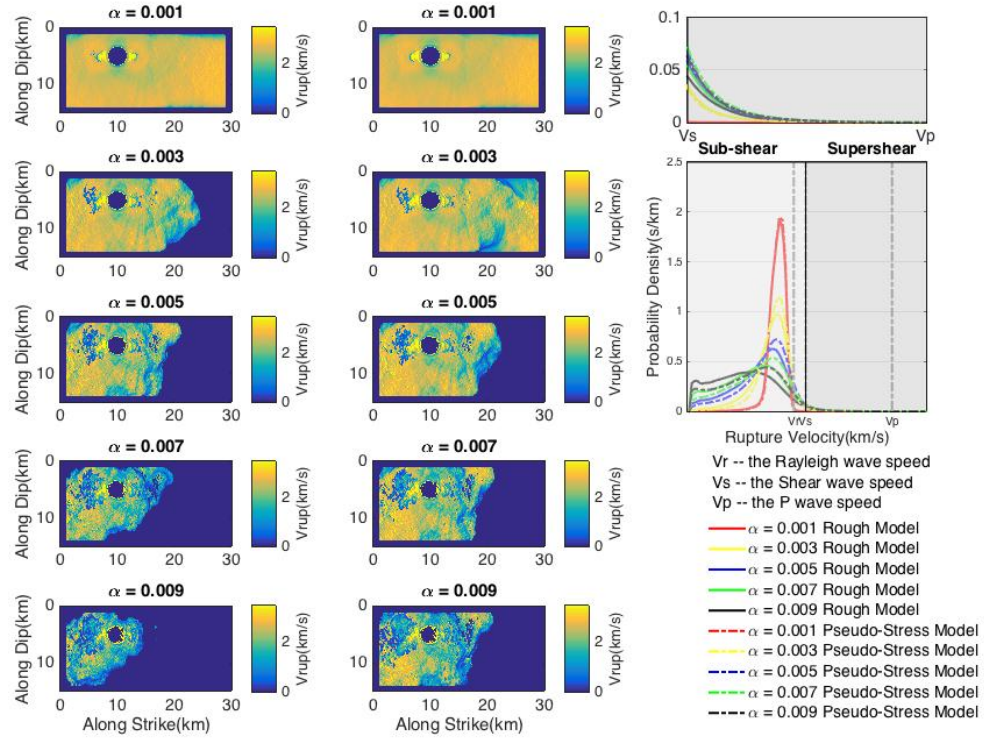


Figure 3.9: Comparison between the same case in pseudo-stress model and rough model at all level of fault roughness. (Left) Distribution of rupture velocity at each simulation in rough model in SET1, and α is increasing from top to bottom. (Middle) same as before in pseudo-stress model in SET5. (Right) Probability densities of rupture velocity in all simulation in SET1 and SET5.

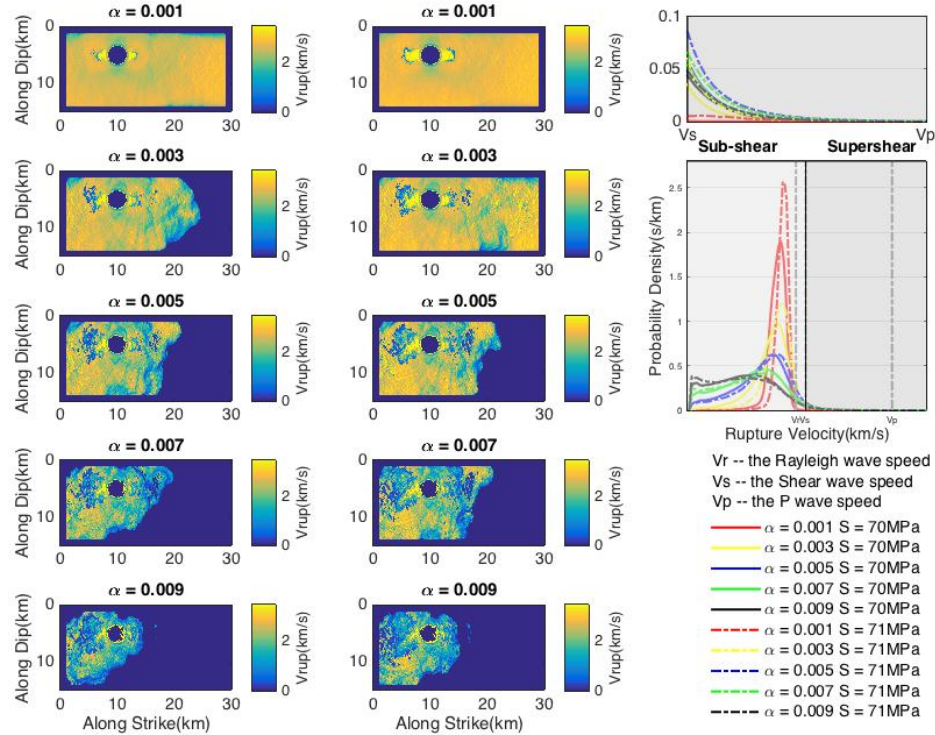


Figure 3.10: (Left) Rupture velocity distribution on the fault at different levels of fault roughness in one realization when background shear stress is 70MPa. From top to bottom, α is increasing from 0.001 to 0.009. (Middle) Rupture velocity distribution on the fault at different levels of fault roughness in one realization when background shear stress is 71MPa. From top to bottom, α is increasing from 0.001 to 0.009. (Right) Middle figure is probability densities of rupture velocity in all simulation in SET1 and SET4. The solid lines are for probability densities in SET1, and dashed lines are for probability densities in SET4. Increasing background shear stress increases supershear phenomena. Top figure is the zoomed out of supershear region in the middle figure.

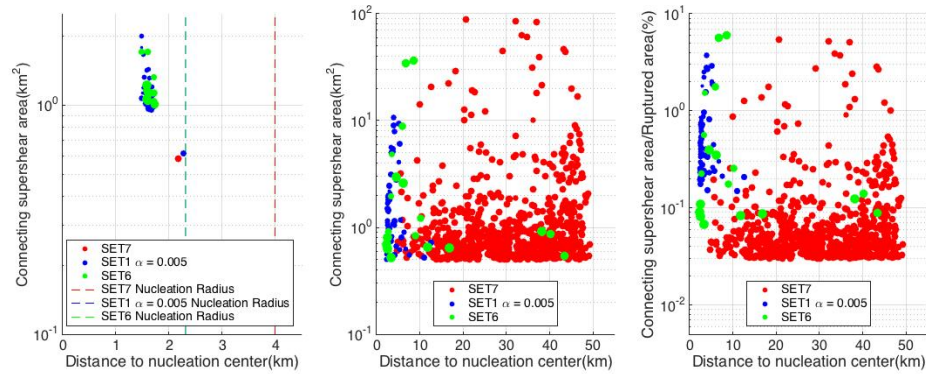


Figure 3.11: Connecting supershear patches depend on the distance to the nucleation center, nucleation strategy, fault length and fault width. (left) shows comparisons of all connecting supershear patches areas whose area are no smaller than 0.5km^2 vs distance to nucleation center in SET7, SET1 $\alpha = 0.005$ and SET6 in the nucleation regions. (middle) shows the same as before, except outside of the nucleation regions. (right) shows comparisons of ratio of all connecting supershear patches areas and ruptured areas vs distance to nucleation center in SET7, SET1 $\alpha = 0.005$ and SET6. The circle size for each point is proportional to the ruptured area in that simulation event.

Chapter 4

Surface Lateral Slip and Shallow Slip Deficit from 3D Rough Fault Simulations

Natural faults deviate from planarity, with scaled rms deflections from the mean plane ranging from 0.001 to 0.01, depending on the degree of fault surface roughness. Fault surface roughness has strong influence on the stress concentration around the fault, and affects the dynamics of the earthquake process. The irregular stress concentration induced by fault surface roughness leads to inelastic deformation of off-fault material. In the 1999 Izmit Earthquake and the 1940 Imperial Valley Earthquake, surface measurements have demonstrated lateral variability of slip distributions on all scales. In the 1992 Landers Earthquake, off-fault deformations accounted for up to 40% of lateral slip. In this study, we simulate 3D dynamic rupture propagation on a self-similar non-planar fault with elastoplastic material off the fault and examine the effects of varying fault surface roughness. We have observed that the surface lateral slips on-fault and off-fault within different damage zone widths are self-affine, and the Hurst exponent H is dependent on the fault roughness level. The Hurst exponent of on- plus off-fault displacements in our study across damage zones always falls into the range from 0.5 to 1, which is larger than 0.44 measured in the 1992 Landers Earthquake (*Milliner et al.*, 2015, 2016). Coseismic slip shows SSD (Shallow Slip Deficit) on fault, and the

ratio of the slip at the surface to the slip at depth decreases when fault roughness level increases. Off-fault deformation near the Earth surface due to plastic yielding contributes to the permanent SSD. The amount of plastic strain heterogeneity at the surface near damage zone increases when fault roughness increases, and the amount of plastic strain at depth is more related to the slip amount on fault, which decreases when fault roughness increases.

4.1 Introduction

Recent improvement of space geodetic data (e.g., Interferometric Synthetic Aperture Radar and Global Positioning System) provides detailed information of coseismic slip on fault plane, indicating the slip at depth around 4-5km in large ($M \geq 7$) strike slip earthquakes is systematically larger than the slip near the Earth surface (e.g. *Reilinger et al.*, 2000; *Simons et al.*, 2002; *Fialko*, 2004a; *Fialko et al.*, 2005; *Bilham*, 2010). Examples include, but are not limited to, the 1992 M7.3 Landers earthquake, the 1999 M7.1 Hector Mine earthquake, the 2003 M6.5 Bam earthquake and the 2010 M7.0 Haiti earthquake. Since the origin of the shallow slip deficit (SSD) is very important to analyzing earthquake physics and estimating seismic hazard, it is crucial to have a good understanding about what factors contribute to the SSD.

Many studies have investigated the possible origins of SSD. The slip on a fault plane should be uniform at different depths, and equal to the sum of the co-, post- and inter- seismic slip after many earthquake cycles (*Tse and Rice*, 1986). Large magnitude of the discrepancy between the slip near the free surface and the slip at depth around 20%~80% during the coseismic period can not be fully explained by shallow creep promoted by velocity strengthening of fault gouge or shallow sediments (*Rice and Tse*, 1986) nor by after slip or other aseismic events during post- and interseismic period in aforementioned earthquakes (*Fialko et al.*, 2005). Another explanation is inelastic off-fault deformation, which has been documented for many strike-slip earthquakes, such as the 1992 M7.3 Landers earthquake (*Milliner et al.*, 2015) and the 1999 M7.5 Izmit earthquake (*Rockwell*

et al., 2002).

Numerical studies have been carried out to study dynamic rupture with off-fault plasticity during earthquakes (*Yamashita*, 2000; *Ben-Zion and Shi*, 2005; *Templeton and Rice*, 2008; *Andrews*, 1976a, 2005; *Duan and Day*, 2008), which generates a "flower-like" structure near the Earth surface since the confining pressure is relatively low near the free surface (*Ma*, 2008; *Ma and Andrews*, 2010). Off-fault deformation accounts for about 15% SSD at the uppermost few kilometers by plastic yielding in 2D dynamic rupture models (*Kaneko and Fialko*, 2011). Kinematic inversion on basis of elastic response introduces another bias up to 10% SSD (*Kaneko and Fialko*, 2011). *Roten et al.* (2017b) have carried out 3D dynamic rupture simulations of the 1992 Landers earthquake, which generate 44-53% SSD, comparable with 30-60% SSD reported by geological observations (*Milliner et al.*, 2015).

Another potential factor to influence SSD during plastic yielding is the maturity of fault. Fault maturity, characterized by fault roughness, can be represented by a random field of fault surface deflection that is approximately self-similar on natural faults. Fault roughness, which is related to maturity of a fault, is defined as the ratio of the root-mean-square(RMS) deviations from the mean plane h_{RMS} to fault length L , $\alpha = h_{RMS}/L$, that typically falls into range from 10^{-3} to 10^{-2} (e.g. *Power and Tullis*, 1991; *Candela et al.*, 2012; *Shi and Day*, 2013; *Dunham et al.*, 2011b). The agreement of geological and geodetic slip rates on mature faults potentially gives insight that young or infrequently slipping faults may result in SSD (*Fialko*, 2006). Geological observations indicate structurally mature, large-cumulative-displacement faults produce larger ratios of the slip at the surface to the slip at depth than faults that are structurally immature and small-cumulative-slip (*Dolan and Haravitch*, 2014). The effect of fault maturity may be important to understand the origins of SSD on faults because amount of accumulated plastic strain and stored elastic strain energy around the fault irregularity can be affected by fault roughness.

Another reason to highlight the importance of fault roughness is that high-resolution imaging of earthquake surface displacement shows fluctuations of fault

surface slip. Large along-strike fluctuations in slip have been observed for both the 1999 Izmit and the 1940 Imperial Valley earthquakes (*Rockwell et al.*, 2002; *Rockwell and Klinger*, 2013). Free surface lateral slip correlates with along-strike fault trace geometry for the 2001 Kokoxili earthquake (*Klinger et al.*, 2006). Coseismic surface rupture shows variability at all observable length scales and the final slip is self-affine fractal in the 1992 Landers earthquake (*Milliner et al.*, 2015). The rough fault simulations allow us to investigate the extent to which observed characteristics of surface slip heterogeneity may be related to the geometrical roughness of faults.

In this study, we run 3D dynamic simulations with off-fault plasticity on rough faults to examine how SSDs vary with different roughness levels. We have investigated the distributions of surface lateral slips, both on fault and across different damage zone widths, which are self-affine. In our study, we have found that SSD, plastic strain and fault parallel displacements on the free surface are sensitive to fault maturity. The Hurst exponent H for on- plus off-fault displacements across different damage zone widths usually falls into the range from 0.5 to 1, which is larger than 0.44 measured from field observations in the 1992 Landers Earthquake (*Milliner et al.*, 2015, 2016).

4.2 Model Setup

The simulations are done using SORD (*Ely et al.*, 2008, 2009) code (a generalized finite difference method to permit irregular structured meshes), with an elasto-plastic solver, based on trial-stress formulation (*Shi and Day*, 2013). For all simulations in this study, rupture is nucleated by imposing a shear traction perturbation at time $t = 0$ on a circular fault patch centered at $(x_1^0, x_2^0) = (15km, 12km)$ with radius $R = 2km$, and of the same form as used in (*Shi and Day*, 2013),

$$\Delta\tau_0(x_1, x_2) = \exp\left(\frac{r^2}{r^2 - R^2}H(R - r)\tau_0(x_1, x_2)\right), \quad (4.1)$$

where H is the Heaviside step function, $r = \sqrt{(x_1 - x_1^0)^2 + (x_2 - x_2^0)^2}$, and $\tau_0(x_1, x_2)$ is the shear traction resolved by initial stresses onto the rough fault plane.

The fault dimensions are 60km (along strike) \times 30km (along dip), which are illustrated in Figure 4.1. The 2D self-similar fault surface is constructed by the same Fourier transform method described in *Shi and Day* (2013). We randomly choose a fault surface realization, and scale it to 5 different roughness levels α , ranging from 0.001 to 0.009. The minimum wavelength of rough fault, which is the lower wavelength cutoff when constructing the self-similar fault surface, is 200m, and the Hurst exponent H is 1.

Rather than using homogeneous initial stress condition, we consider the effects of lithostatic loading and hydrostatic pore pressure. The effective initial normal stresses are given by $\sigma_{11} = \sigma_{22} = \sigma_{33} = -(\rho - \rho_w)gx_2$, where g is gravitational acceleration, and ρ and ρ_w are densities of rock and water, respectively. The initial shear stresses are assumed to be $\sigma_{31} = \sigma_{22} \times 7/12$ and $\sigma_{12} = \sigma_{23} = 0$.

We employ a rate- and state-dependent (RSD) friction with strongly rate-weakening features to simulate the fault frictional behavior. Strong dynamic rate weakening during rupture process has been observed in high-speed friction experiments (e.g. *Tsutsumi and Shimamoto*, 1997; *Di Toro et al.*, 2004; *Han et al.*, 2010; *Goldsby and Tullis*, 2011; *Brown and Fialko*, 2012). The laboratory data indicates the frictional behavior of the uppermost brittle layer is velocity strengthening (e.g. *Marone et al.*, 1991). The rate and state friction law supports self-sustaining slip pulses both on planar and nonplanar faults, even with off-fault plasticity (*Dunham et al.*, 2011a,b; *Gabriel et al.*, 2013; *Shi and Day*, 2013).

We adopt Drucker-Prager plasticity model (*Drucker and Prager*, 1952) to describe the pressure-dependent inelastic yielding of material. To avoid extreme plastic deformation localization, we use a Maxwellian viscoplasticity scheme (e.g. *Andrews*, 2005; *Duan and Day*, 2008; *Ma and Andrews*, 2010) to adjust stress to Drucker-Prager yield surface. We use 5MPa for cohesion and 0.75 for internal friction coefficient. All of the elastic and viscoplastic properties of the bulk material in this model are summarized in Table 4.1 and Figure 4.2. To better understand rupture properties in plastic cases, we also carry out another set of simulations (elastic cases) without inelastic yielding of material.

4.3 Result

In this section, we present simulation results focusing on the effects of fault roughness on the surface lateral slip, shallow slip deficit, off-fault displacement and plastic strain.

4.3.1 Surface Lateral Slip

Figure 4.3 shows the final slip distributions on fault plane at 5 different fault roughness values α , ranging from 0.001 to 0.009. The pattern of final slip distributions correlates well with the restraining and releasing bends, which shows a great amount of heterogeneity. The mean slip amplitudes on faults generally decrease with increasing fault roughness level, which can be explained by additional fault roughness drag induced by fault roughness (*Fang and Dunham, 2013; Yao et al., 2015; Dieterich and Smith, 2009*).

The final fault slips along the surface fault trace at 5 different fault roughness levels show some amount of heterogeneity at all levels of fault roughness. With higher fault roughness level, the slip distributions show smaller average amplitudes and larger percent of slip variations in Figure 4.4a. There is a power-law relation between the amplitude and wavelength of the final slip along the fault trace at each of the 5 different levels of fault roughness, both in elastic cases (Figure 4.4b) and plastic cases (Figure 4.4c).

At the same fault roughness level, the Hurst exponent for plastic case is larger than that in elastic case. Plastic yielding reduces the amount of slip, which is mainly controlled by fault roughness level and minimum wavelength of the rough fault in elastic cases. As introduced by *Fang and Dunham (2013)*, roughness contributes an additional resistance to slip, the roughness drag, given by $\tau^{drag} \propto \alpha^2/\lambda_{min}$ in elastic cases. λ_{min} is minimum wavelength of the rough fault. The plasticity further reduces the slip. In our simulations, the heterogeneity of plastic strain on a rough fault induced by plastic yielding enhances the surface slip heterogeneity, leading to larger amount of slip variations at different wavelengths. The plastic strain is heterogenous along the whole fault trace, and the amount of

plastic strain heterogeneity differs point to point, therefore it contributes to larger amplitudes of slip variations.

There seem to be two somewhat distinct contributions to slip distributions in plastic cases compared to elastic cases, larger slip variation and smaller average amplitude of slip induced by fault roughness drag with plastic yielding. The first factor is very important to spectrum analysis because slip variation is the one affecting power spectral density, rather than absolute slip amount. Plastic yielding produces wavelength-dependent and fault-roughness-dependent effects upon power spectral density of slip on fault. When $\alpha = 0.001$, the plastic strain distribution is more uniform near fault, and the power spectral density in the plastic case increases without large change of the Hurst exponent compared to that of elastic case. When $\alpha = 0.009$, power spectral density increases at high wavelength and decreases a little at low wavelength in plastic case compared to that in elastic case, resulting in an increase in the Hurst exponent compared to the elastic case. In this case, the high fault roughness results in the plastic strains near the fault becoming strongly localized (as we discuss later).

The Hurst exponent H for both plastic and elastic cases increases when fault roughness increases systematically. Large variations of surface slip induced by fault roughness are mainly enhanced at wavelength ranging from 10^{-4} to 5×10^{-3} in both cases. The Hurst exponent change from 0.59 to 1.19 in plastic cases, and from 0.57 to 0.84 in elastic cases from $\alpha = 0.001$ to $\alpha = 0.009$. In elastic cases, the slip variations due to fluctuations of fault geometry (plus variations of plastic strain heterogeneity in plastic cases) give higher amplitude of slip variations at high wavelength on rougher faults, and almost constant at low wavelength at all levels of fault roughness levels. This wavelength-dependent property at different fault roughness levels may be related to the strain localization, but a full explanation will require further exploration..

4.3.2 Shallow Slip Deficit

The ratio of the mean surface slip along fault trace to the mean slip at depth has been investigated. The depth at which the maximum slip occurs varies

a little for different cases, therefore we use the depth where the maximum slip occurs rather than fixed depth to calculate the ratio. Figure 4.5(left) shows SSDs at 5 different fault roughness levels for both plastic and elastic cases. The slip amount drops quickly when the direct-effect friction parameter a starts to increase from 4km to the surface for both elastic and plastic cases. In plastic cases, plastic yielding tends to suppress the mean slip in the uppermost crust (less than 2km) with low values of confining stress (e.g. pre-damaged rock) and promote inelastic strain accumulation, which does not affect much the slips at depth. This part of SSD is permanent, representing irreversible deformation in the near-site rocks or sediments. Another factor to reduce magnitude of coseismic slip near the Earth surface is smaller stress drop which is linearly dependent on depth in our model. For rougher cases, the shallow slip reduction is accompanied by increased elastic strain energy stored in short-wavelength strain fluctuations near fault. Over multiple earthquake cycles, this buildup of stored strain energy will eventually have to be expressed as inelastic deformation. The free surface itself, on the contrary, promotes coseismic slip accumulations. Overall, the slips near the free surface are always smaller than those at depth, and the ratios between these two variables are smaller than 1 at all fault roughness levels, in both plastic and elastic cases.

In our study, we have found that coseismic SSD is dependent on fault roughness level. Figure 4.5(right) shows how SSD varies with fault roughness level. When the fault is rougher, coseismic slips at depth and near the Earth surface are both reduced by fault roughness drag (*Fang and Dunham, 2013; Yao et al., 2015*), and the ratio between the slips at free surface and at depth becomes smaller. The ratio increases when the fault gets smoother, which is consistent with the study by *Dolan and Haravitch (2014)* that structurally mature faults give smaller SSD than faults these are structurally immature. This part of the SSD in our simulations is not due to plastic strain, but due to buildup of the stored elastic strain energy around the fault irregularity, which will eventually have to be expressed as inelastic strain in later earthquakes.

4.3.3 Off-Fault Displacement and Plastic Strain

As mentioned before, the reduction of slip near the surface by plastic yielding has been observed in plastic cases in Figure 4.5(left). Figure 4.6a shows the mean off-fault displacements (averaged along strike directions) at free surface in both plastic and elastic cases. The reduction of fault parallel displacements at the surface is observed gradually near fault mainly from -5km~5km in plastic cases, at all fault roughness levels. *Milliner et al.* (2015) found that off-fault deformation is higher near geometrically complex parts of the 1992 Landers rupture. In our simulations, the average slip amplitude on fault decreases when the fault roughness increases, and the corresponding off-fault deformation decreases too. In Figure 4.6b, the reduction of fault parallel displacement near fault is larger in plastic cases when the fault roughness level is larger.

As we discussed in section 4.3.1, the slips on fault are self-affine at 5 different roughness levels in plastic cases. We have also found that the surface displacements across the fault plus damage zone are also self-affine. This result is shown in Figure 4.7, and is similar to geological observations of the 1992 Landers earthquake. *Milliner et al.* [2015] investigated the total surface deformation across the Landers damage zone. They found along-strike variability at all observable length scales, with a power-law power spectrum, and inferred that surface slip can be represented as a self-affine fractal. In the simulations, the surface inelastic deformation decays gradually away from the fault. We have investigated the effects of including varying widths ("damage zone widths") of that deformation zone in the total displacement calculation. In the simulations, when $\alpha = 0.001$, across different damage zone widths, the Hurst exponents of total displacements show small variability. When $\alpha = 0.009$, the displacement variations at all wavelengths reduce with larger damage zone width due to the reductions of plastic strain heterogeneity as distance from the fault increases. Within the same damage zone width, for example within -0.5~0.5km off-fault, displacement variations change more rapidly at low wavelength than high wavelength when α increases. Even though the Hurst exponent increases with α for each damage zone width, this trend is weaker for larger damage zone width. In our simulated datasets, the difference of Hurst ex-

ponents of total displacements on fault at $\alpha = 0.001$ and $\alpha = 0.009$ on fault is 102%, and reduced to 68%, 48% and 34% when the damage zone width is 0.5km (-0.25~0.25km off-fault), 1.0km (-0.5~0.5km off-fault), and 1.5km (-0.75~0.75km off-fault), respectively.

The degree of plastic deformation near the surface is proportional to the amount of SSD (*Kaneko and Fialko, 2011*). Figure 4.8 shows permanent plastic strain distributions across the fault at $x_1 = 10km$ at 5 different fault roughness levels. On smooth fault when $\alpha = 0.001$, the plastic strain is larger and more widely spreading since there is smaller fault roughness drag (*Fang and Dunham, 2013; Yao et al., 2015*), leading to a larger amount of slip on fault. The fault roughness promotes heterogeneity of plastic strain distributions. In Figure 4.9, plastic strain distributions on fault surface have been illustrated. There is a lack of plastic strain around $x_1 = 30km$, therefore, the difference of the slip amplitude at $x_1 = 30km$ and the slip at the end of fault trace is very large in plastic cases (Figure 4.4a). Plastic strain heterogeneity on the free surface has been observed, and the amount of plastic strain heterogeneity near fault increases when fault roughness increases.

4.4 Discussion

In our study, we have observed that the off-fault displacements within different damage zone widths are self-affine, which is consistent with the field observations (*Milliner et al., 2015*). *Milliner et al. (2015)* found that the total on- and off-fault deformation is self-affine, and the Hurst exponent H of the total on- plus off-fault deformation over about 100m~200m (mean 154m) wide damage zone in the 1992 Landers earthquake is 0.44 based on their spectral slopes (*Milliner et al., 2015, 2016*). *Milliner et al. (2015)* have found the correlation between slip complexity and geometrical complexity, and both the magnitude and width of distributed deformation are largest in stepovers and bends. In our simulations, more intense off-fault deformations have observed in smoother cases, but this is primarily because those cases have more total slip. The slip-normalized off-fault

deformation is similar across the different roughness levels, and that deformation is more intensely localized in the rough cases.

The Hurst exponents of on-fault slip at 5 different fault roughness levels from $\alpha = 0.001$ to $\alpha = 0.009$ are 0.59, 0.78, 0.94, 1.07 and 1.2. Adding off-fault deformation moves H values toward lower values. In our simulations, The Hurst exponent of on- plus off-fault displacements across damage zones usually falls into the range from 0.5 to 1, which is higher than 0.44 measured in the 1992 Landers earthquake (*Milliner et al.*, 2015, 2016). The Hurst exponent of the off-fault displacements within damage zone widths $-0.25\text{km}\sim 0.25\text{km}$ in our simulations at 5 different fault roughness levels from $\alpha = 0.001$ to $\alpha = 0.009$ are 0.55, 0.63, 0.73, 0.83 and 0.93, respectively. More realistic cohesion model (smaller cohesion values in the crust) as in *Roten et al.* (2017b) could change our H values, maybe towards smaller values. Real fault like the Landers system have more complex types of geometry, which are not modeled by our simulations, like small stepovers and minor intersecting fault segments, all of which might explain lower values of H.

A significant limitation of the study is the homogeneity of the cohesion model and initial stress model. The cohesion value in our model is 5MPa, and the internal friction coefficient is 0.75, both of which are uniform on the whole fault plane, and the initial shear and normal stress on mean plane are linearly dependent on depth. By excluding all parameter heterogeneity, we can isolate and more easily interpret the effects of fault roughness on rupture dynamics. However, it is not realistic to assume homogeneous stress distribution on fault plane without considering the volumetric stress fields generated around the fault after many earthquake cycles. Also, the cohesion model which does not consider variations of rock properties with depth (lower cohesion value near the Earth surface) (*Roten et al.*, 2017b) could affect the plastic yielding along with rupture dynamics. A more realistic cohesion and stress heterogeneity should be assumed in future study.

As illustrated by *Kaneko and Fialko* (2011), the inversion of geodetic data based on purely elastic models introduces an artificial deficit of SSD up to 10 percent of maximum slip for 2D strike slip faults, and *Kaneko and Fialko* (2011) also

point out that the 3D geometry may be important to the analysis. The amount of slip at depth is typically calculated by inversion of surface static displacements in natural earthquakes using elastic Green's function. In 3D dynamic elasto-plastic simulations, the plastic yielding changes the fault slip distributions and surface static displacements compared with pure elastic cases. It is worthwhile to investigate how much bias could be introduced into the calculations of SSD based on the inversion results by inelastic behaviors and how fault roughness level effects the extent of this bias.

As we discussed in section 4.3.1, the plastic yielding suppresses the amount of slip near the surface; however it is important to know how fault roughness affects the permanent SSD. In our model, the amounts of mean slip (averaged along strike) at different fault roughness are different. Therefore it is a good extension of this study to build models which generate the same amounts of mean slip at the depths of maximum slip at different fault roughness levels, but allow the slip near the surface to vary with fault roughness level. Then it is more straightforward to measure how much SSD is due to plastic yielding at different fault roughness levels.

In our study, all the dynamic simulations are carried out on one fault surface realization. A large ensemble of models can provide more robustness and reliability of the results. With more realistic models developed in the future, it is possible that we can link our simulated data to the field observations more accurately.

4.5 Conclusion

3D dynamic rupture simulations on rough faults with plastic yielding have been investigated in this study. We demonstrate that fault roughness can play an important role in determining the surface slip, shallow slip deficit, off-fault displacements and plastic strain near fault. The numerical simulations in this study employ the rate and state friction law with dynamic weakening, combined with Drucker-Prager elasto-plasticity (with viscous regularization). The fault roughness in this study is assumed to be self-similar with rms deflections ranging from 10^{-3}

to 10^{-2} times the fault length .

We find that the surface lateral slip in this model is self-affine with Hurst exponent increasing when the fault roughness level increases in both elastic cases and plastic cases. even though plastic strain reduces the total amount of slip, it increases the spatial variability of slip, and this is in part because fault roughness causes plastic strain heterogeneity that are highly variable along strike. We have found plastic yielding shows wavelength-dependent and fault-roughness-dependent behaviors that affect the power spectral density of slip on the fault. The process results in Hurst exponents in plastic cases that are always higher than those in elastic cases, though a more complete understanding of the mechanism controlling this difference will require further studies.

We also investigate how individual event SSD on rough faults is sensitive to the roughness level of the fault. The coseismic slip near the Earth surface and at depth are larger when α is smaller, and the ratio between them is larger. Part of the SSD is induced by permanent plastic strain accumulated near the surface. The other contributions to the SSD in our models, including velocity-strengthening and reduced stress drop near the surface, are transient effects that eventually have to be compensated for by large slips or inelastic relaxations in subsequent events.

We also find that the Hurst exponents of on- plus off-fault displacements across different damage zone widths also show self-affine property, and the Hurst exponent increases when fault roughness level increases. The Hurst exponent of on- plus off-fault displacements in our study always falls into the range of 0.5 to 1, which is larger than 0.44 which is measured by *Milliner et al.* (2015, 2016) in the 1992 Landers Earthquake. If the lower Milliner et al. H estimate proves to be representative of other similar events, it may be indicative of additional sources of natural complexity (e.g., stepovers, subsidiary intersecting faults, heterogeneities in yield strength) that are absent in the current numerical model.

4.6 Acknowledgements

This work was supported by NSF award EAR-1135455. Simulations were done using the generalized finite difference code SORD at Blue Waters supercomputer at the National Center for Supercomputing Applications. Input files to reproduce the simulation results are available upon request.

Chapter 4, in full, is a reformatted version of a paper currently being prepared for submission for publication to *Geophysical Research Letters*: Yao, Q. and S. M. Day, Free Surface Lateral Slip and Shallow Slip Deficit from 3D Rough Fault Simulations. (2017). I was the primary investigator and author of this paper.

References

- Andrews, D. (1976a), Rupture propagation with finite stress in antiplane strain, *J. Geophys. Res.*, *81*(20), 35753582.
- Andrews, D. (1976b), Rupture velocity of plane strain shear cracks, *J. Geophys. Res.*, *81*(32), 56795687.
- Andrews, D. (2005), Rupture dynamics with energy loss outside the slip zone, *J. Geophys. Res.*, *110*(B1), B01,307.
- Ben-Zion, Y., and Z. Shi (2005), Dynamic rupture on a material interface with spontaneous generation of plastic strain in the bulk, *Earth and Planetary Science Letters*,(1), 486496.
- Bilham, R. (2010), Lessons from the Haiti earthquake, *Nature*, *463*(7283), 878879.
- Bizzarri, A. (2010), How to promote earthquake ruptures: Different nucleation strategies in a dynamic model with slip-weakening friction, *Bull. Seism. Soc. Am.*, *100*(3), 923-940.
- Brown K, Fialko Y (2012) 'Melt welt' mechanism of extreme weakening of gabbro at seismic slip rates. *Nature.*, *488*(7413):638-41. PMID: 22932388.
- Bruce E. Shaw, Surface slip gradients of large earthquakes, *Bull. Seism. Soc. Am.*, *101*, 792, doi:10.1785/0120100053, 2011.
- Bryant, W. (1992), Surface fault rupture along the Johnson Valley, Homestead Valley, and related faults associated with the Ms 7.5 28 June 1992 Landers earthquake, Fault Eval. Rep. FER-234, Calif. Dep. of Conserv., Div. of Mines and Geol., Sacramento, Calif.

- Bryant, W. (1994), Surface fault rupture along the Homestead Valley, Emerson, and related faults associated with the Mw 7.3 28 June 1992 Landers earthquake, Fault Eval. Rep. FER-239, Calif. Dep. of Conserv., Div. of Mines and Geol., Sacramento, Calif.
- Candela, T., F. Renard, M. Bouchon, A. Brouste, D. Marsan, J. Schmittbuhl, and C. Voisin (2009), Characterization of fault roughness at various scales: Implications of three-dimensional high resolution topography measurements, *Pure Appl. Geophys.*, *166*(1011), 18171851, doi:10.1007/s00024-009-0521-2.
- Candela, T., F. Renard, Y. Klinger, K. Mair, J. Schmittbuhl, and E. E. Brodsky (2012), Roughness of fault surfaces over nine decades of length scales, *J. Geophys. Res.*, *117*, B08409, doi:10.1029/2011JB009041.
- Chester, F. M., and J. S. Chester (2000), Stress and deformation along wavy frictional faults, *J. Geophys. Res.*, *105*(B10), 23,42123,430, doi:10.1029/2000JB900241.
- Cochran, E. S., Y.-G. Li, P. M. Shearer, S. Barbot, Y. Fialko, and J. E. Vidale (2009), Seismic and geodetic evidence for extensive, long-lived fault damage zones, *Geology*, *37*(4), 315318.
- Cohee, B. P., and G. C. Beroza (1994), Slip distribution of the 1992 Landers earthquake and its implications for earthquake source mechanics, *Bull. Seism. Soc. Am.*, *84*(3), 692712.
- Cui, Y., K. Olsen, K. Lee, J. Zhou, P. Small, D. Roten, G. Ely, D. Panda, A. Chourasia, J. Levesque, S. Day, and P. Maechling (2010), Scalable earthquake simulation on petascale supercomputers, in Proceedings of SC10, November 13-19, New Orleans, LA.
- Day, S., and C. Bradley (2001), Memory-efficient simulation of anelastic wave propagation, *Bull. seism. Soc. Am.*, *91*(3), 520.
- Day, S. M., L. A. Dalgner, N. Lapusta, and Y. Liu (2005), Comparison of finite difference and boundary integral solutions to three-dimensional spontaneous rupture, *J. Geophys. Res.*, *110*(B12), 123, doi 10.1029/2005JB003813.
- Di Toro, G., D. L. Goldsby, and T. E. Tullis (2004), Friction falls toward zero in quartz rock as slip velocity approaches seismic rates, *Nature*, *427*, 436439, doi:10.1038/nature02249.
- Dieterich, J. H., and D. E. Smith (2009), Nonplanar faults: Mechanics of slip and off-fault damage, *Pure Appl. Geophys.*, *166*, 17991815, doi:10.1007/s00024-009-0517-y

- Dolan, J. F., and B. D. Haravitch (2014), How well do surface slip measurements track slip at depth in large strike-slip earthquakes? The importance of fault structural maturity in controlling on-fault slip versus off-fault surface deformation, *Earth and Planetary Science Letters*, *388*, 3847.
- Drucker, D. C., and W. Prager (1952), Soil mechanics and plastic analysis of limit design, *Q. Appl. Math.*, *10*, 157165.
- Duan, B., and S. M. Day (2008), Inelastic strain distribution and seismic radiation from rupture of a fault kink. *J. Geophys. Res.*, *113*(B12), 119. doi:10.1029/2008JB005847.
- Dunham, E. M., D. Belanger, L. Cong, and J. E. Kozdon (2011a), Earthquake ruptures with strongly rate-weakening friction and off-fault plasticity, Part 1: Planar faults, *Bull. Seism. Soc. Am.*, *101*(5), 22962307.
- Dunham, E. M., D. Belanger, L. Cong, and J. E. Kozdon (2011b), Earthquake ruptures with strongly rate-weakening friction and off-fault plasticity, Part 2: Nonplanar faults, *Bull. Seism. Soc. Am.*, *101*(5), 23082322.
- Ely, G. P., S. M. Day, and J.-B. H. Minster (2008). A support-operator method for visco-elastic wave modeling in 3-D heterogeneous media. *Geophysical Journal International*, *172*, 331344.
- Ely, G. P., S. M. Day, and J.-B. H. Minster (2009). A support-operator method for 3-D rupture dynamics. *Geophysical Journal International*, *177*, 11401150.
- Ely, G. P., S. M. Day, and J.-B. H. Minster (2010), Dynamic rupture models for the southern San Andreas Fault, *Bull. Seismol. Soc. Am.*, *100*(1), 131150, doi:10.1785/0120090187.
- Fang, Z., and E. M. Dunham (2013). Additional shear resistance from fault roughness and stress levels on geometrically complex faults, *J. Geophys. Res.* *118*, no. 7, 36423654, doi: 10.1002/jgrb.50262.
- Fialko, Y. (2004a), Probing the mechanical properties of seismically active crust with space geodesy: Study of the coseismic deformation due to the 1992 Mw 7.3 Landers (southern California) earthquake, *Journal of Geophysical Research: Solid Earth* (19782012), *109*(B3).
- Fialko, Y. (2004b), Evidence of fluid-filled upper crust from observations of post-seismic deformation due to the 1992 Mw 7.3 Landers earthquake, *Journal of Geophysical Research: Solid Earth*, *109*(B8).
- Fialko, Y., D. Sandwell, D. Agnew, M. Simons, P. Shearer, and B. Minster (2002), Deformation on nearby faults induced by the 1999 Hector Mine earthquake, *Science*, *297*(5588), 18581862.

- Fialko, Y., D. Sandwell, M. Simons, and P. Rosen (2005), Three-dimensional deformation caused by the Bam, Iran, earthquake and the origin of shallow slip deficit, *Nature*, *435*(7040), 295299.
- Fialko, Y. (2006), Interseismic strain accumulation and the earthquake potential on the southern San Andreas fault system, *Nature*, *441*, doi:10.1038/nature04797, 968-971.
- Frey Mueller, J., N. King, and P. Segall (1994), The co-seismic slip distribution of the Landers earthquake, *Bull. Seism. Soc. Am.*, *84*(3), 646659.
- Gabriel, A. A., J. P. Ampuero, L. A. Dalguer, and P. M. Mai (2013), Source properties of dynamic rupture pulses with off-fault plasticity, *J. Geophys. Res. Solid Earth*, doi:10.1002/jgrb.50213.
- Goldsby, D. L., and T. E. Tullis (2011), Flash heating leads to low frictional strength of crustal rocks at earthquake slip rates, *Science*, *334*, 216218, doi:10.1029/1126/science.1207902.
- Graves, R., and R. Pitarka (2016), Kinematic ground motion simulations on rough faults including effects of 3D stochastic velocity perturbations, *Bull. Seism. Soc. Am.*, *106*(5), 21362153.
- Han, R., T. Hirose, and T. Shimamoto (2010), Strong velocity weakening and powder lubrication of simulated carbonate faults at seismic slip rates, *J. Geophys. Res.*, *115*, B03412, doi:10.1029/2008JB006136.
- Harris, R., M. Barall, R. Archuleta, E. Dunham, B. Aagaard, J. Ampuero, H. Bhat, V. Cruz-Atienza, L. Dalguer, P. Dawson, et al. (2009), The SCEC/USGS dynamic earthquake rupture code verification exercise, *Seism. Res. Lett.*, *80*(1), 119126.
- Harris, R. A., M. Barall, D. Andrews, B. Duan, S. Ma, E. Dunham, A.-A. Gabriel, Y. Kaneko, Y. Kase, B. Aagaard, J.-P. Oglesby, J. Ampuero, T. Hanks, and N. Abrahamson (2011), Verifying a computational method for predicting extreme ground motion, *Seism. Res. Lett.*, *82*(5), 638644.
- Hartleb, R. D., J. F. Dolan, H. S. Akyz, T. E. Dawson, A. Z. Tucker, B. Yerli, T. K. Rockwell, E. Toraman, Z. akir, A. Dikbas, et al. (2002), Surface rupture and slip distribution along the Karadere segment of the 17 August 1999 Izmit and the western section of the 12 November 1999 Dzce, Turkey, earthquakes, *Bull. Seism. Soc. Am.*, *92*(1), 6778.
- Hoek, E. (1994), Strength of rock and rock masses, *ISRM News Journal*, *2*(2), 416.
- Hoek, E., and E. T. Brown (1997), Practical estimates of rock mass strength, *International Journal of Rock Mechanics and Mining Sciences*, *34*(8), 11651186.

- Kaneko, Y., and Y. Fialko (2011), Shallow slip deficit due to large strike-slip earthquakes in dynamic rupture simulations with elasto-plastic off-fault response, *Geophysical Journal International*, *186*(3), 13891403.
- Klinger, Y., R. Michel, and G. C. P. King (2006), Evidence for an earthquake barrier model from $M_w \times 7.8$ Kokoxili (Tibet) earthquake slip-distribution, *Earth Planet. Sci. Lett.*, *242*, 354364. doi:10.1016/j.epsl.2005.12.003.
- Ma, S. (2008), A physical model for widespread near-surface and fault zone damage induced by earthquakes, *Geochem. Geophys. Geosyst.*, *9*(11), Q11,009.
- Ma, S., and D. Andrews (2010), Inelastic off-fault response and three-dimensional dynamics of earthquake rupture on a strike-slip fault, *Journal of Geophysical Research: Solid Earth* (19782012), *115*(B4).
- Marinos, V., P. Marinos, and E. Hoek (2005), The geological strength index: applications and limitations, *B. Eng. Geol. Environ*, *64*(1), 5565.
- Marone, C. J., C. Scholtz, and C. Bilham (1991), On the mechanics of earthquake afterslip, *J. Geophys. Res.*, *96*(B5), 84418452.
- Milliner, C., J. Dolan, J. Hollingsworth, S. Leprince, F. Ayoub, and C. Sammis (2015), Quantifying near-field and off-fault deformation patterns of the 1992 M_w 7.3 Landers earthquake, *Geochem. Geophys. Geosyst.*, *16*(5), 15771598.
- Milliner, C., J. Dolan, J. Hollingsworth, S. Leprince, and F. Ayoub (2016), Comparison of coseismic near-field and off-fault surface deformation patterns of the 1992 m_w 7.3 Landers and 1999 m_w 7.1 Hector mine earthquakes: Implications for controls on the distribution of surface strain, *Geophys. Res. Lett.*, *43*(19).
- Olsen, K. B., R. Madariaga, and R. J. Archuleta (1997), Three-Dimensional Dynamic Simulation of the 1992 Landers Earthquake, *Science*, *278*, 834838.
- Power, W. L., and T. E. Tullis (1991), Euclidean and fractal models for the description of rock surface roughness, *J. Geophys. Res.*, *96*(B1), 415424, doi:10.1029/90JB02107.
- Reilinger, R., S. Ergintav, R. Brgmann, S. McClusky, O. Lenk, A. Barka, O. Gurkan, L. Hearn, K. Feigl, R. Cakmak, et al. (2000), Coseismic and postseismic fault slip for the 17 August 1999, $M = 7.5$, Izmit, Turkey earthquake, *Science*, *289*(5484), 15191524.
- Rice, J. (1993), Spatio-temporal complexity of slip on a fault, *J. Geophys. Res.*, *98*(B6), 98859907.
- J. R. Rice and S. T. Tse (1986), Dynamic Motion of a Single Degree of Freedom System following a Rate and State Dependent Friction Law, *J. Geophys. Res.*, *91*, pp. 521-530.

- Rockwell, T. K., and Y. Klinger (2013), Surface rupture and slip distribution of the 1940 Imperial Valley earthquake, Imperial Fault, Southern California: Implications for rupture segmentation and dynamics, *Bull. Seismol. Soc. Am.*, *103*(2A), 629640.
- Rockwell, T. K., S. Lindvall, T. Dawson, R. Langridge, W. Lettis, and Y. Klinger (2002), Lateral offsets on surveyed cultural features resulting from the 1999 Izmit and Duzce earthquakes, Turkey, *Bull. Seism. Soc. Am.*, *92*(1), 7994.
- Roten, D., K. Olsen, Y. Cui, and S. Day (2017), Quantification of fault zone plasticity effects with spontaneous rupture simulations, *Pure and Applied Geophysics*, pp. 123, doi:DOI10.1007/s00024-017-1466-5.
- Roten, D., K.B. Olsen, and S.M. Day (2017). Off-fault deformations and shallow slip deficit from dynamic rupture simulations with fault zone plasticity, *Geophys. Res. Lett.*, accepted.
- Scholz, C. H. (1998), Earthquakes and friction laws, *Nature*, *391*(6662), 3742.
- Shi, Z., and S. M. Day (2013), Rupture dynamics and ground motion from 3-D rough-fault simulations, *J. Geophys. Res.*, *118*(3), 11221141.
- Simons, M., Y. Fialko, and L. Rivera (2002), Coseismic deformation from the 1999 Mw7.1 Hector Mine, California, earthquake as inferred from InSAR and GPS observations, *Bull. Seism. Soc. Am.*, *92*(4), 13901402.
- Templeton, E., and J. Rice (2008), Off-fault plasticity and earthquake rupture dynamics: 1. dry materials or neglect of fluid pressure changes, *Journal of Geophysical Research: Solid Earth* (19782012), *113*(B9).
- Tsutsumi, A., and T. Shimamoto (1997), High-velocity frictional properties of gabbro, *Geophys. Res. Lett.*, *24*(6), 699702.
- S. T. Tse and J. R. Rice (1986), Crustal Earthquake Instability in Relation to the Depth Variation of Frictional Slip Properties, *J. Geophys. Res.*, *91*, pp 9452-9472.
- Xu, X., X. Tong, D. T. Sandwell, C. W. Milliner, J. F. Dolan, J. Hollingsworth, S. Leprince, and F. Ayoub (2016), Refining the shallow slip deficit, *Geophysical Journal International*, *204*(3), 18671886.
- Yamashita, T. (2000), Generation of microcracks by dynamic shear rupture and its effects on rupture growth and elastic wave radiation, *Geophysical Journal International*, *143*(2), 558 395406.
- Yao. Q., S. M. Day and Z. Shi, Earthquake source-parameter relationships from 3D rough fault dynamic ruptures, Abstract S43E-08 presented at 2015 Fall Meeting, AGU, San Francisco, Calif, 14-18, Dec.

Zhang, H., C. Thurber, and P. Bedrosian (2009), Joint inversion for V_p , V_s , and V_p/V_s at SAFOD, Parkfield, California, *Geochem. Geophys. Geosyst.*, *10*, Q11002, doi:10.1029/2009GC002709

Zinke, R., J. Hollingsworth, and J. F. Dolan (2014), Surface slip and off-fault deformation patterns in the 2013 Mw 7.7 Balochistan, Pakistan earthquake: Implications for controls on the distribution of near-surface coseismic slip, *Geochem. Geophys. Geosyst.*, *15*(12), 50345050.

Table 4.1: Model Parameters

Parameter		Value
P Wave Velocity (km/s)	C_p	6000
S Wave Velocity (km/s)	C_s	3464
Possion's ratio	ν	0.25
Density (kg/m^3)	ρ	2670
Cohesion(MPa)	c	5
Internal friction coefficient	$\tan(\Phi)$	0.75
Evolution-effect parameter	b	0.14
Reference slip rate($\mu m/s$)	V_0	1
Steady-state coefficient at slip rate V_0	f_0	0.7
Evolution distance of state variable ψ	L	0.2
Fully weakened friction coefficient(m)	L_{pc}	0.2
Initial fault slip rate(m/s)	V^{ini}	6×10^{-11}
Nucleation Width (m)		2000
Time Step Size (s)	dt	0.004
Number of Fault Roughness Levels		5

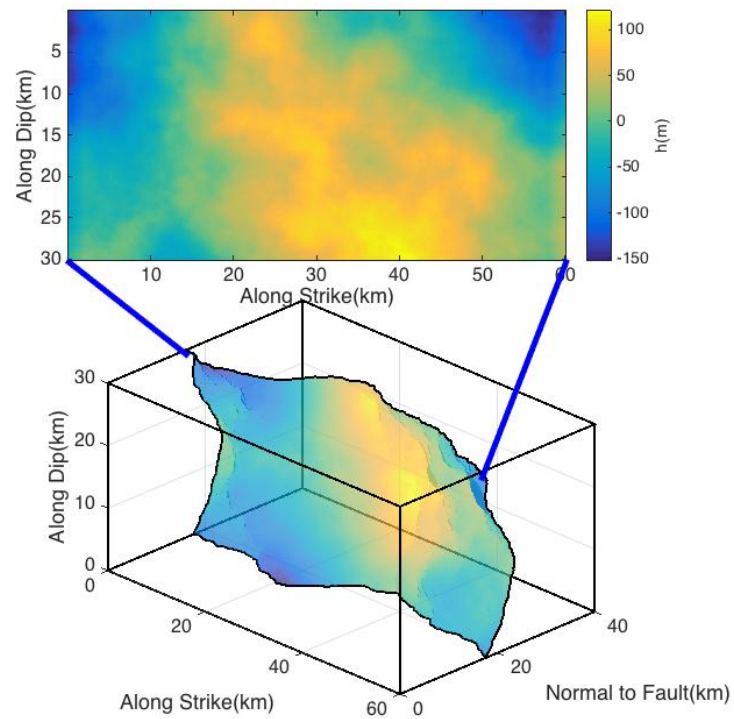


Figure 4.1: Model Geometry and dimensions for 3D earthquake dynamic rupture. (Top) Example of rough fault surface. The color scale denotes deviation of the rough-fault surface. For better view, the fault deviation has been greatly exaggerated in the 3D plot.

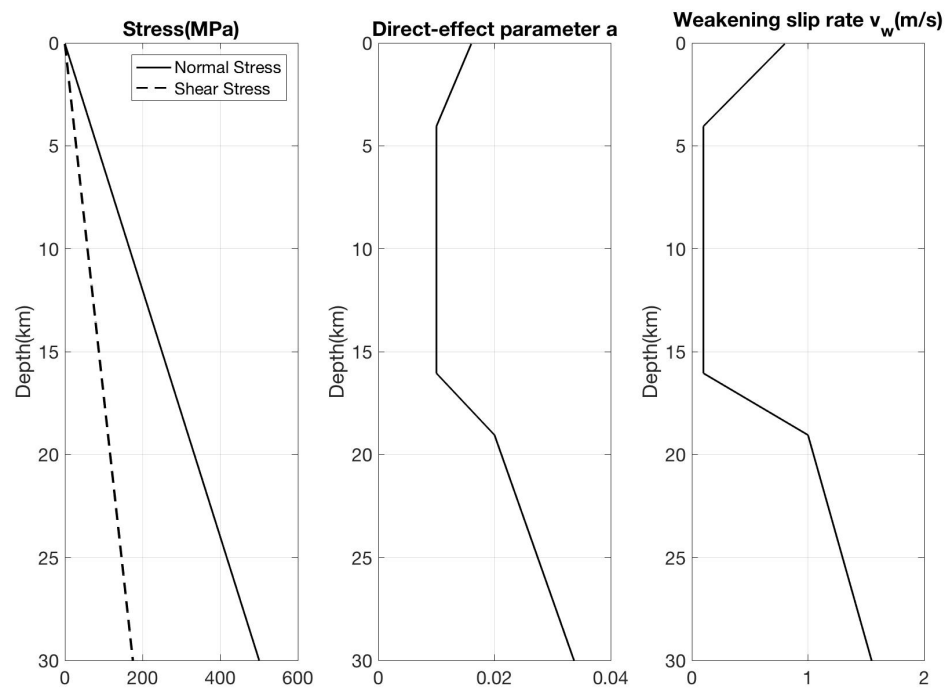


Figure 4.2: Initial normal and shear stresses resolved onto the mean fault plane, RSD friction parameters (b and v_w).

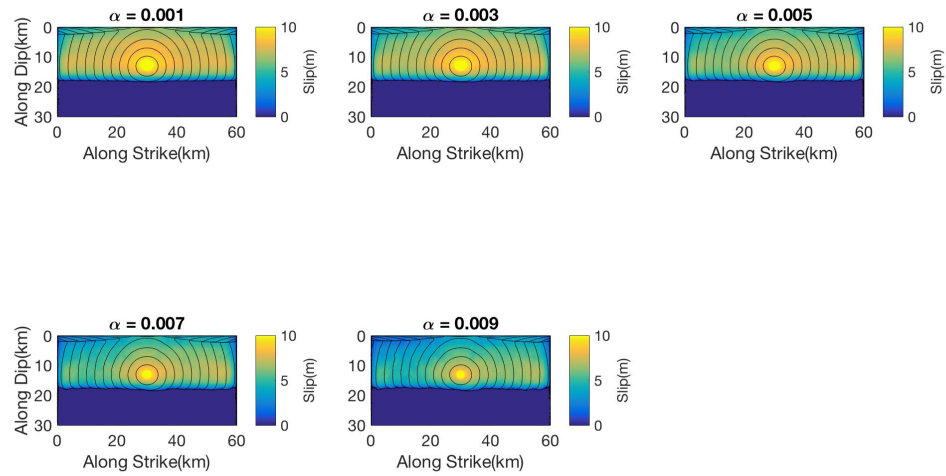


Figure 4.3: Final slip distribution on fault plane from dynamic rupture at 5 different α level (increasing from top to bottom) in plastic cases. Black lines are contours of rupture fronts at 1s intervals mapped onto the mean fault plane.

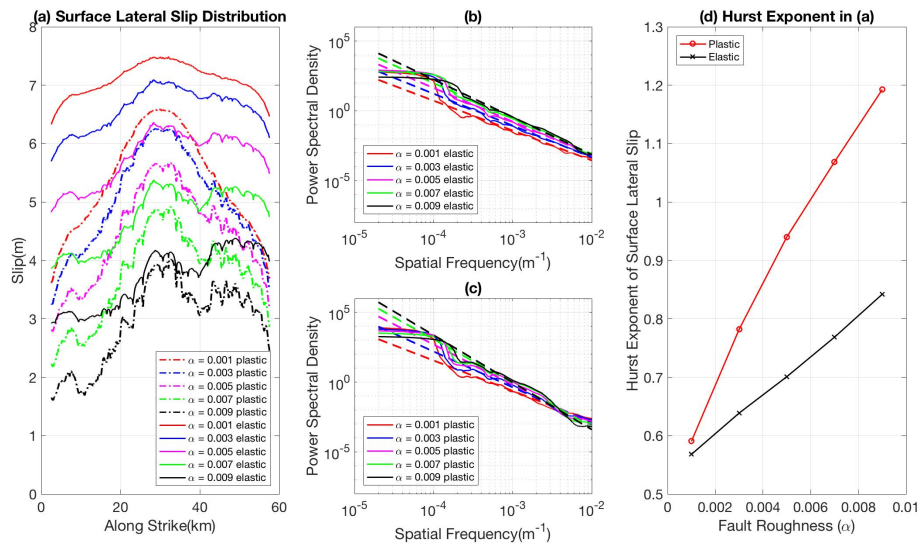


Figure 4.4: (a) Surface lateral slip distributions and power spectral density of surface lateral slip in (a) elastic cases and (b) plastic cases at 5 different fault roughness levels. Solid lines are calculated psd, and dashed lines are fitted psd. (d) Hurst exponents of surface lateral slip distributions.

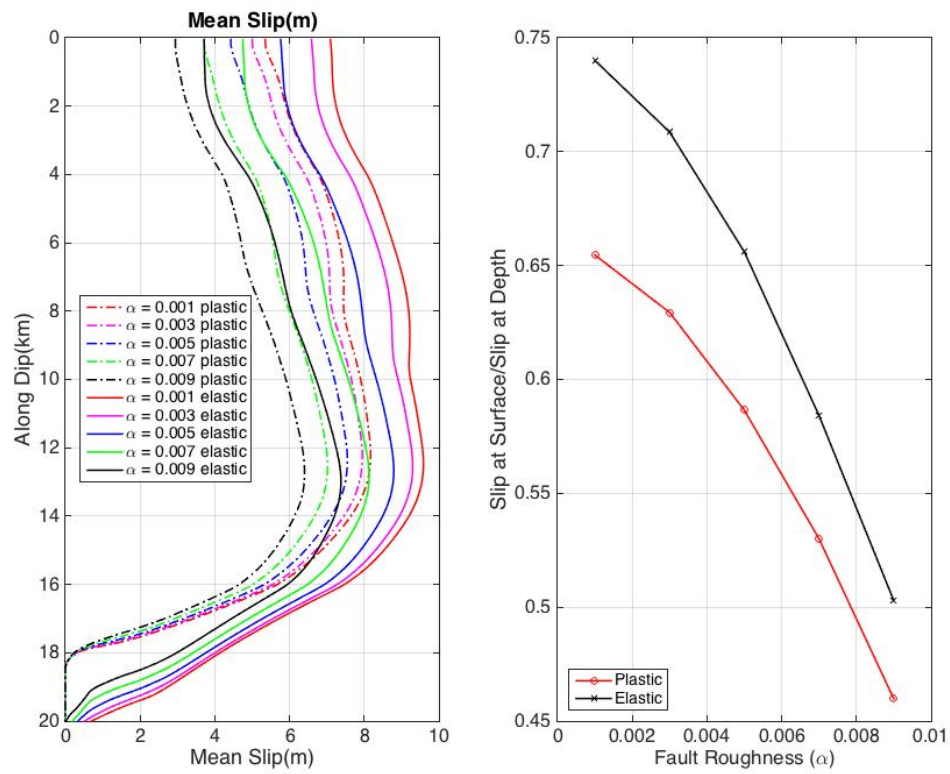


Figure 4.5: (left) shows mean surface slips (averaged along strike) obtained at 5 fault roughness levels. (right) shows the ratio of slip near Earth surface and at depth, are dependent on the fault roughness level.

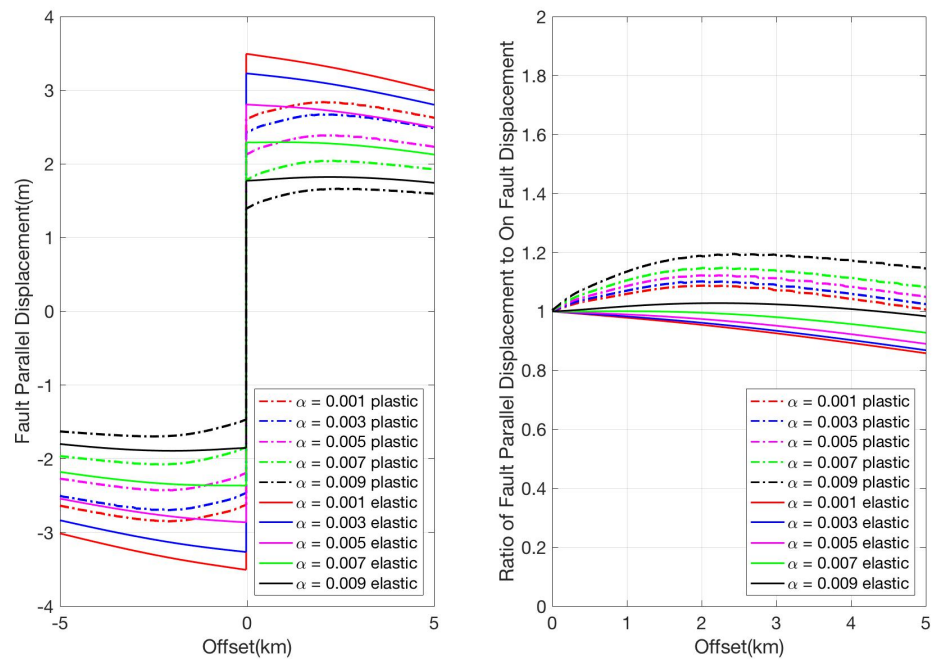


Figure 4.6: (left) Mean fault parallel displacement (averaged along strike) obtained for both elastic and plastic cases at 5 fault roughness levels. (right) Ratio of fault parallel displacement to on fault displacement for both elastic and plastic cases at 5 fault roughness levels.

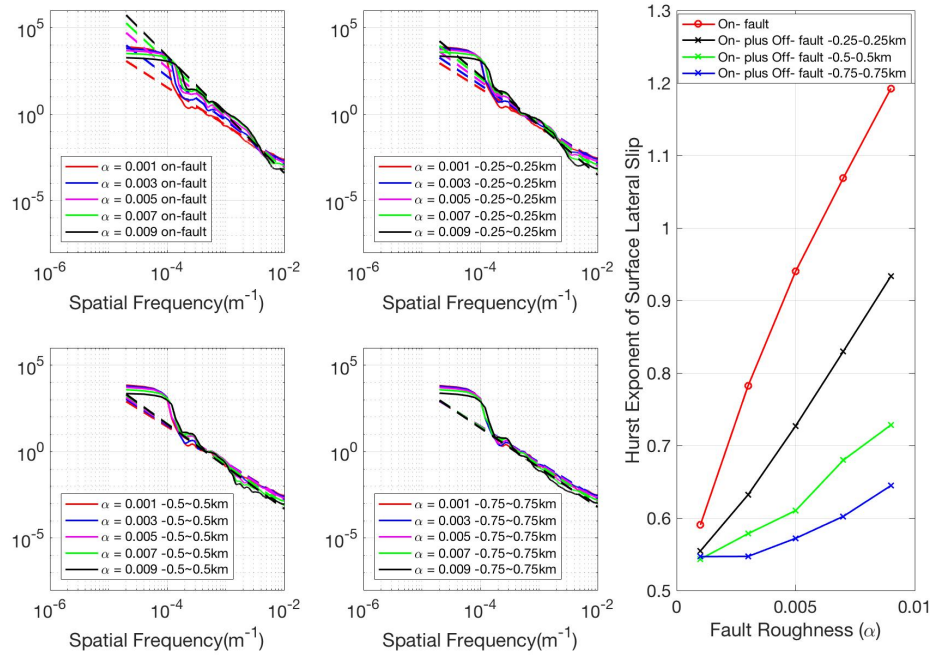


Figure 4.7: Power spectral density of surface lateral slips on-fault and on-plus off-fault within different damage zone $-0.25\text{km}\sim 0.25\text{km}$, $-0.5\text{km}\sim 0.5\text{km}$, $-0.75\text{km}\sim 0.75\text{km}$ at 5 different fault roughness levels in plastic cases. Solid lines are calculated psd, and dashed lines are fitted psd. (right) Hurst exponent of different surface lateral slips.

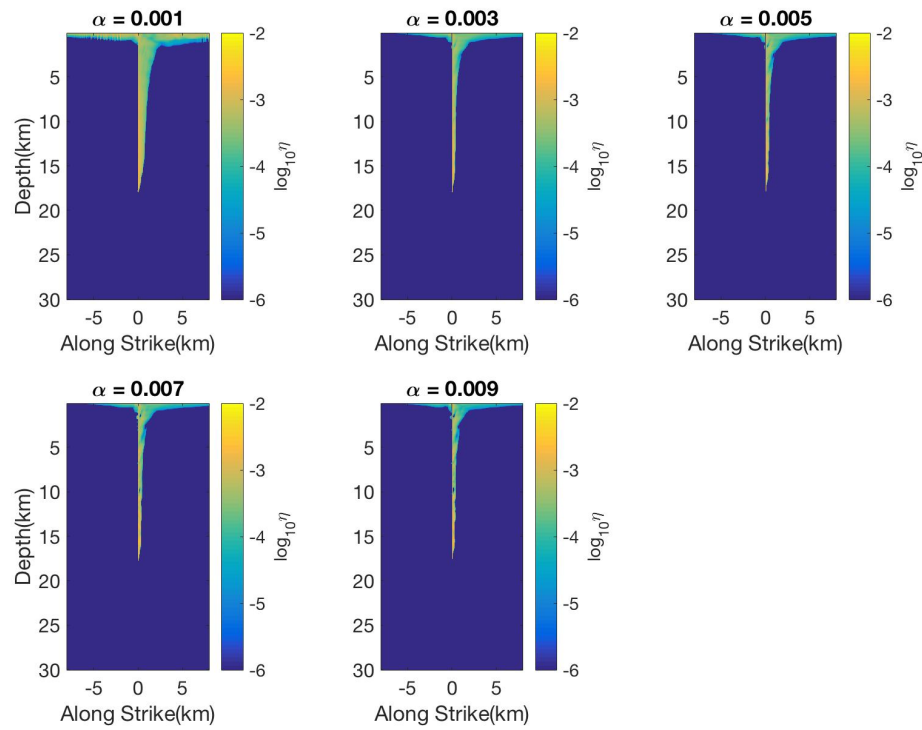


Figure 4.8: Distributions of accumulated plastic strain along cross-sections perpendicular to fault at $x = 10\text{km}$ for plastic cases.

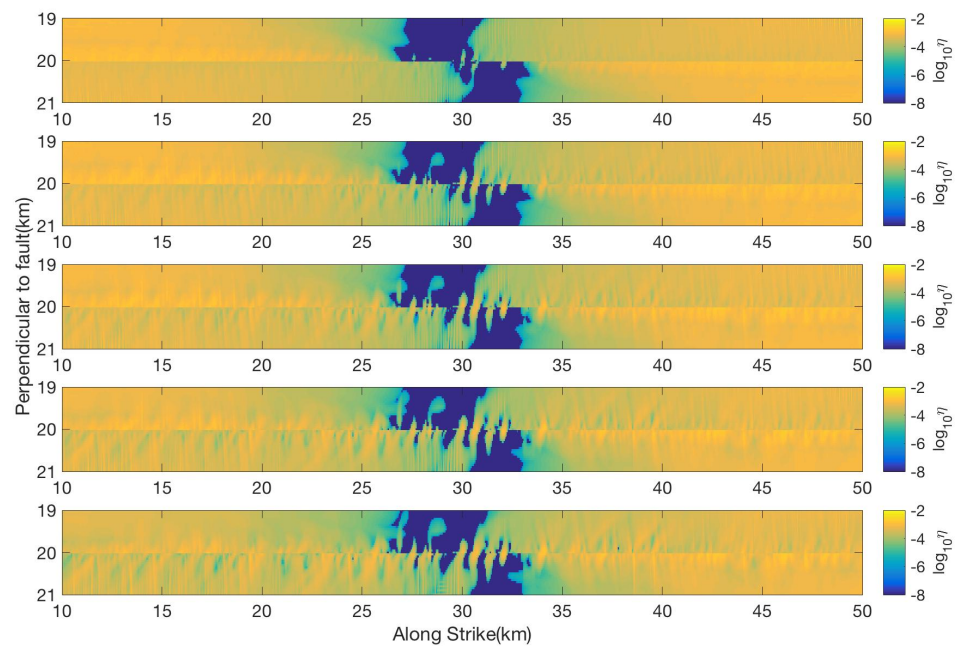


Figure 4.9: Distributions of accumulated plastic strain at 25m for plastic cases for different fault roughness levels. α ranges from 0.001 to 0.009 from top to bottom.